TRIBOLOGICAL BEHAVIOURS OF MAGNESIUM ALLOY SECTOR SHAPE PAD WITH SURFACE MODIFICATION

A Thesis submitted to the Delhi Technological University, Delhi in fulfillment of the requirements for the award of the degree of

DOCTOR OF PHILOSOPHY

in

Mechanical Engineering

by

SUMIT JOSHI
(2K16/PHDME/07)

Under the guidance of

Dr. R. C. SINGH
(Professor)
Department of Mechanical Engineering,
Delhi Technological University,
New Delhi-110042, India.

Dr. RAJIV CHAUDHARY
(Professor)
Department of Mechanical Engineering,
Delhi Technological University,
New Delhi-110042, India.

DEPARTMENT OF MECHANICAL ENGINEERING
DELHI TECHNOLOGICAL UNIVERSITY
NEW DELHI-110042, INDIA

DECLARATION

I hereby declare that the thesis entitled "**TRIBOLOGICAL BEHAVIOURS OF MAGNESIUM ALLOY SECTOR SHAPE PAD WITH SURFACE MODIFICATION**" is an original work carried out by me under the supervision of **Dr. R.C. Singh, Professor**, Department of Mechanical Engineering, Delhi Technological University, Delhi, and **Dr. Rajiv Chaudhary, Professor**, Department of Mechanical Engineering, Delhi Technological University, Delhi. This thesis has been prepared in conformity with the rules and regulations of the Delhi Technological University, Delhi. The research work presented and reported in the thesis has not been submitted either in part or full to any other university or institute for the award of any other degree or diploma.

SUMIT JOSHI

(2K16/PHDME/07)

Department of Mechanical Engineering

Delhi Technological University, Delhi

Date: 09/12/2021

Place: New Delhi

CERTIFICATE

This is to certify that the thesis entitled, **"TRIBOLOGICAL BEHAVIOURS OF MAGNESIUM ALLOY SECTOR SHAPE PAD WITH SURFACE MODIFICATION"** submitted by **Mr. Sumit Joshi** to the Delhi Technological University, Delhi for the award of the degree of Doctor of Philosophy in Mechanical Engineering is a bonafide record of original research work carried out by him under our supervision in accordance with the rules and regulations of the institute. The results presented in this thesis have not been submitted, in part or full, to any University or Institute for the award of any degree or diploma.

Dr. Ramesh Chandra Singh
Professor,
Department of Mechanical Engineering,
Delhi Technological University,
Delhi, India

Dr. Rajiv Chaudhary
Professor,
Department of Mechanical Engineering,
Delhi Technological University,
Delhi, India

ACKNOWLEDGMENTS

I would like to express my deep gratitude, sincere thanks and appreciation to my supervisors Prof. Ramesh Chandra Singh and Prof. Rajiv Chaudhary for their valuable guidance during this Ph.D. work. I am thankful from my heart for all the help, encouragement, and support you generously extended to me.

I would like to express, a sincere gratitude to Prof. R.S. Mishra, Chairman, DRC, Mechanical Engineering Department and Prof. S K Garg, Head of the Department, Mechanical Engineering, Delhi Technological University, for their valuable help, motivation and extending all the necessary processing and experimental facilities during my research work.

Thanks are also due to Prof. R.K. Pandey, Prof. Abid Haleem, Prof. D.S. Nagesh, Prof. Reeta Wattal, Prof. Atul Kumar Agarwal and Prof. S.G. Warkar for serving my SRC committee members and many critical help without which I would not be able to complete my thesis in time.

I am also grateful to Prof. Ranganathan M. S. (DTU), Dr. M. Saravanan (NPL, Delhi) and Dr. N. Yuvaraj (DTU) for all the motivation and their teachings, without that I would not be able to finish my thesis work.

I gratefully acknowledge Institute Instrumentation Centre, IIT Roorkee and National Physical Laboratory, Delhi for the characterization facility.

My sincere thank to all the faculty and staff members of Department of Mechanical Engineering (DTU), who supported me during my entire course work and research work. I am grateful to Mr. Rajesh Bohra, Mr. Manjeet and Mr. Tekchand for their technical and experimental support.

I am grateful to the management of at Maharaja Agrasen Institute of Technology, Delhi, particularly Dr. Nand Kishor Garg, Founder Chairman, Sh. Prem Sagar Goel, Chairman, Prof. M. L. Goyal, Vice Chairman (Academics), Prof. Neelam Sharma, Director and Prof. Vednath Mathur, Head, Department of Mechanical and Automation Engineering for the timely help and support in every possible way to finish this thesis work.

I would like to express my sincere thanks to Dr. Vipin Kumar Sharma, Assistant Professor, MAIT, Mr. Ramakant Rana, Assistant Professor, MAIT, Mr. Madhukar Chhimwal, Assistant Professor, MAIT, Mr. Prashant (Research Scholar, DTU) and friends for their support and encouragement throughout this period.

I am also grateful to the expert examiners for improving the overall quality of the thesis.

I am short of words to express my sincere gratitude to my parents. Whatever I have achieved in my professional life; it is because of them. I cannot express in words their efforts to nurture me. I am also grateful to my wife Mrs. Neha for her support and encouragement during thesis writing.

Last but not the least; I thank the Almighty for giving me strength to complete this work in all respects.

(SUMIT JOSHI)

New Delhi, 2021

ABSTRACT

In the ongoing demand for light weight materials, magnesium alloys are equally comparable to aluminium alloys because of attributes such as high specific strength, low density, high damping capacity and better machinability. Magnesium-Aluminium-Silicon (Mg-Al-Si) is one of the Mg alloy series which is well recognised for elevated temperature applications as they contain the thermally stable Mg_2Si intermetallic compound. However, the coarse and brittle nature of Mg_2Si deteriorates the mechanical and tribological properties; therefore researchers are working on its modification and refinement to enhance the widespread use of heat resistant Mg-Al-Si alloys.

The rapid emerging surface modification phenomena like Friction Stir Processing (FSP) have proved its potential in achieving significant grain refinement and morphological modification in the materials thus enhancing their mechanical and wear behaviour.

In the present research, Magnesium-Aluminium-Silicon (Mg-Al-Si) based AS21A magnesium alloy was examined for microstructural, mechanical and tribological characterization in respect of the cast and Friction Stir Processed (FSPed) conditions. The Taguchi − Grey Relational Analysis (GRA) − Principal Component Analysis (PCA) hybrid methodology was applied to achieve the optimized values of FSP parameters.

Microstructural features exhibit the fragmentation of coarse Mg_2Si to fine particles thus creating their homogeneous dispersion and eliminate the casting defects present in the parent material. The morphological structure modification achieved through FSP resulted in the significant enhancement of mechanical properties like strength, ductility etc. Further, fractography images proved the brittle failure in cast AS21A sample while ductile failure in FSPed AS21A sample.

In tribological study, FSPed AS21A samples exhibited noteworthy improvement in the wear characteristics at all assessment conditions. It was established that the morphology

of Mg_2Si precipitates had an active contribution in the wear behaviour of cast and FSPed AS21A samples. The notable mechanisms found responsible for the wear of samples were adhesion, abrasion, oxidation, delamination and plastic deformation.

An attempt has also been made to replace the Babbitt coating with the investigated alloy in thrust bearing applications in the form of sector shape pad.

CONTENTS

LIST OF FIGURES

LIST OF TABLES

LIST OF ABBREVIATIONS

BM	Base Material
COF	Coefficient of Friction
EDS	Energy Dispersive Spectroscopy
FSP	Friction Stir Processing
FSPed	Friction Stir Processed
GRA	Grey Relational Analysis
GRC	Grey Relational Coefficient
GRG	Grey Relational Grade
HV	Hardness Value
NZ	Nugget Zone
OM	Optical Microscope
PCA	Principal Component Analysis
PM	Parent Material
RS	Rotational Speed
SEM	Scanning Electron Microscope
SD	Shoulder Diameter
SZ	Stirred Zone
TS	Travel Speed
UTS	Ultimate Tensile Strength
UTM	Universal Testing Machine
XRD	X-ray Diffraction

CHAPTER 1

INTRODUCTION

In the last few decades, with the enhancing need for reasonable utilization of limited energy resources, sky touching crude oil value [1], and strict emission norms, industries is continuously seeking novel and advanced materials as substitutes to the "conventional" materials. Owing to this significant need for sustainable development, the option of light-weight materials is an important and inevitable resolution for the upcoming generation. Magnesium is one such capable candidate in light-weight material category, which is presently lagging for application in manufacturing industries.

1.1 Magnesium Background

Magnesium is the sixth abundant element found in the Earth, constituting 2.7% of Earth's crust [2]. However, magnesium is unavailable in its elemental form; instead magnesium based compounds are extracted universally. The widespread form of magnesium compounds available are magnesite (MgCO), dolomite ($CaMg(CO_3)_2$), carnalite ($KCl{\cdot}MgCl_2{\cdot}6H_2O$), and also found 2.8 % in seawater [3]. Magnesium is one of the lightest structural materials having mass density of 1.7 g/cm^3 that is nearly 35% lighter than aluminium, and 78% lighter than steel [4–6]. Because of their high specific mechanical characteristics and low density, magnesium alloys are actively practised by the industries for weight-critical applications. Magnesium is an energy-efficient candidate which makes them suitable for aerospace, automotive, sports, biomedical and electronic industries [7, 8].

Magnesium with 99.8% purity is readily available commercially but it is initially alloyed with other materials before being employed in engineering industries. The promising features of magnesium and its based alloys are as follows [6]:

- least density of all structural metals;
- higher thermal and electrical conductivity;
- functional damping capacity;
- high specific strength;
- excellent machinability;
- better castability;
- suitable for high-temperature applications using heat resistant alloys;
- can be machined at high speed;

- superior weldability in controlled atmospheric conditions;
- less corrosion rate with high purity magnesium.

Nevertheless, it is extremely crucial to boost the industrial use of magnesium and its alloys since magnesium alloys offer resistance when plastically deformed at room temperature conditions which is attributed to their distinctive hexagonal closed pack crystal structure. At ambient temperature, the HCP structure of Mg alloys provides merely three active slip planes, all parallel to the basal plane. However, at high temperatures, both prismatic and pyramidal slip planes comes in action, thus resulting in a considerable amount of plastic deformation [9]. Therefore, magnesium alloys are alloyed with the metallic elements primarily Al, Zn, Mn and Rare Earth (RE) to synthesize the alloys possessing excellent characteristics. In addition to this, another major challenge with the magnesium is their flammability with oxygen, which makes their casting very difficult. Hence, it is recommended to have perfect vacuum conditions during the melting of magnesium [10]. In brief, the limitations with magnesium based alloys are as follows [11]:

- low modulus of elasticity
- limited amount of formability and toughness
- a considerable amount of shrinkage during casting
- high affinity to oxygen
- poor mechanical behaviour at elevated temperature

1.2 Classification of Magnesium alloys

1.2.1 Designation of magnesium alloys

The designation of Mg alloys is based on the American Society for Testing and Materials (ASTM) standard B275, magnesium alloys are represented by two letters in uppercase followed by the two numbers [12]. The two uppercase letters correspond to major alloying elements:

- The first letter being the highest amount of the respective element;
- The second letter being the next highest amount.

Table 1.1 shows the uppercase letters corresponding to each alloying element of magnesium, generally used to represent the magnesium based alloys. The numbers represent the amount of the two major alloying elements:

- The first number corresponds to the weight % of the first uppercase letter;
- The second number corresponds to the weight % of the second letter.

For instance, AZ91D represents the magnesium alloy containing 9% Al and 1% Zn with D modification. Apart from this, fabrication conditions can also be included in the designation such as ‘O’ for annealed, ‘T’ for temper etc.

Table 1.1 ASTM designation of magnesium alloys [3, 12]

Uppercase letter	Alloyed element	Uppercase letter	Alloyed element
A	Aluminium	H	Thorium
Z	Zinc	C	Copper
M	Manganese	R	Chromium
E	Rare earth	F	Iron
S	Silicon	T	Tin
P	Lead	Q	Silver
K	Zirconium	D	Cadmium

1.2.2 Development of magnesium alloys

The alloy development was necessary to meet the demand of specific property desired in the magnesium alloys by the aerospace and automobile industries. Mordike and Ebert [5] mapped the hierarchy of magnesium alloy development by the layout shown in Figure 1.1.

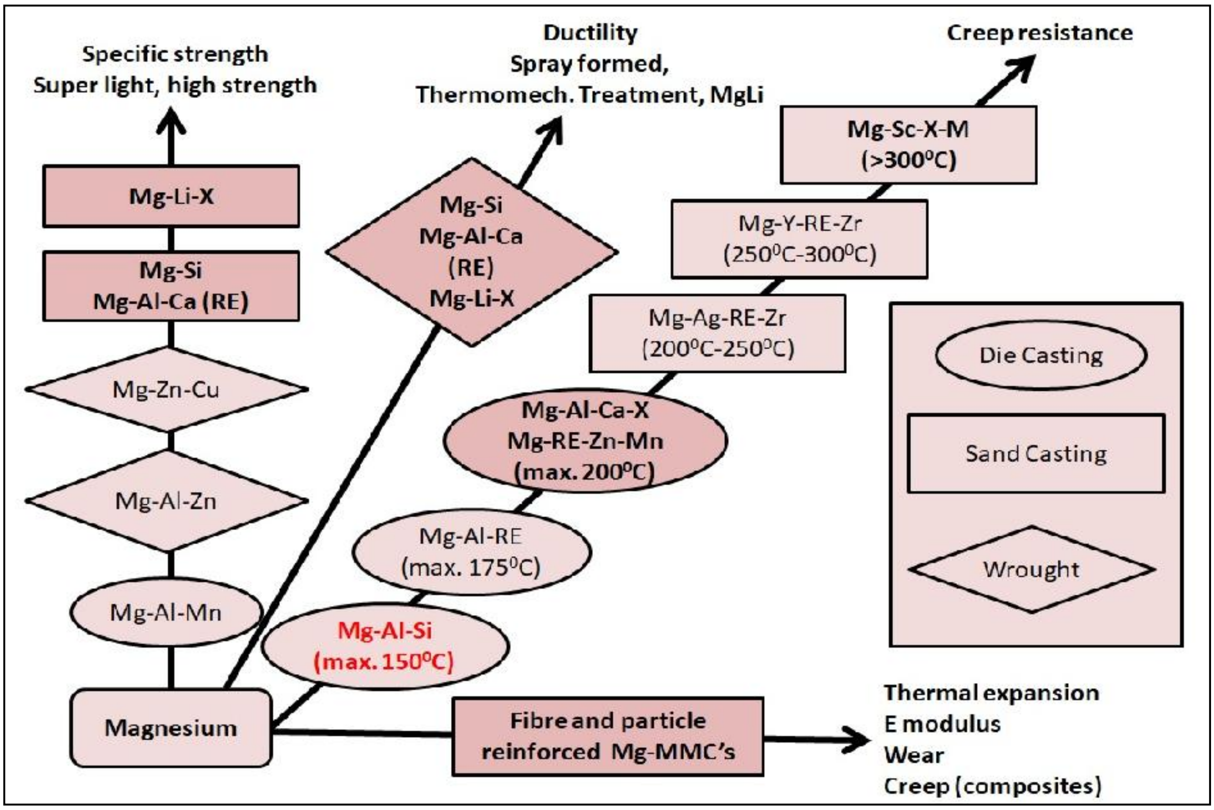

Figure 1.1 Layout depicting the direction of alloy development in magnesium [5]

It can be inferred from the flowchart that Magnesium alloy possess varieties of properties, thus making their widespread use in industries. Among all commercial magnesium alloy products, cast magnesium alloys have a maximum contribution of 85-90% [13]. Some of the commonly employed commercial magnesium alloy systems are:

- Mg-Al-Zn (AZ series)
- Mg-Zn-Zr (ZK series)
- Mg-Al-Mn (AM series)
- High-temperature magnesium casting alloys such as Rare Earth (RE) series, Mg-Al-Si (AS series), Mg-Al-Ca series etc.
- Wrought magnesium alloys

Mg-Al-Zn (AZ series) alloy system is the most universal commercially employed alloy in automotive and aerospace sectors due to its remarkable features like superior ductility, excellent castability and good mechanical properties [3-5]. The solid solubility limit of aluminium in the melt of magnesium is 12.7% at 473^0C, due to which a coarse network of β-$Mg_{17}Al_{12}$ is formed across the grain boundaries in the cast condition. The network of β phase increases the strength of Mg alloys through precipitates hardening and solid solution strengthening mechanisms [14].

The recent growing application of magnesium alloys in power train components encouraged the development of heat resistant or creep resistant magnesium alloys. Power train components like automatic transmission system and engine block are subjected to repeated mechanical and thermal stresses, hence require materials that can resist plastic deformation due to creep [15]. Mg-Al-Zn alloy system is not suitable for the elevated temperature applications since they exhibit poor mechanical behaviour at high temperature (above 120 °C) due to the existence of low melting point β-$Mg_{17}Al_{12}$ phase (about 460 °C) in α-Mg matrix [14]. The newly developed creep resistant alloys [15-18] are classified as:

- RE elements based alloys:
- Calcium based alloys; and
- Silicon based alloys

The RE elements containing magnesium called AE series alloys such as AE42, AE41 and AE21 are the groups of creep resistant magnesium alloys containing 2-4 wt% Al. Since REs are costly, therefore a mixture of RE elements called Misch metal is also employed commercially. RE elements is Neodymium (Nd), Yttrium (Y), Strontium (Sr) etc. Mg-Al-RE series alloy system exhibit remarkable creep behaviour due to the formation of Al-RE intermetallics ($Al_{11}RE_3$ and Al_2RE) in the Mg matrix along with the inhibition of the β-

$Mg_{17}Al_{12}$ compound [17, 18]. Similarly, the formation of Al_2Ca and Mg_2Ca phases in the Mg-Al-Ca series system enhances the creep property [19]. As the current research is focused only on silicon containing alloys; therefore the upcoming section is confined to the study of the Mg-Al-Si alloy.

1.3 Magnesium-Aluminum-Silicon (AS series) alloy

Mg-Al-Si (AS series) alloys were developed for high temperature applications (up to 150 ^{0}C) since they contain hard and brittle thermally stable eutectic Mg_2Si intermetallic phase in the matrix [20]. Morphology of Mg_2Si phase appears as polygon shape or Chinese language [21] as shown by the microstructure in Figure 1.2.

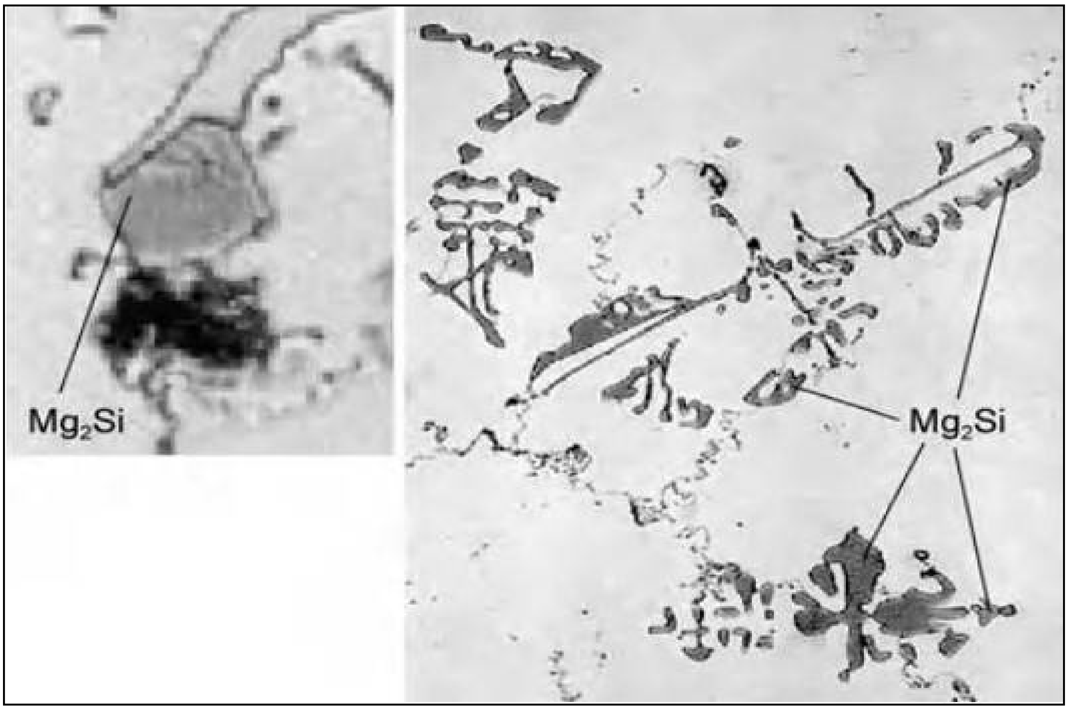

Figure 1.2 Morphology of Mg_2Si intermetallics [21]

The formation of Mg_2Si is due to very less maximum solid solubility (0.003 at %) of Si in Mg at room temperature thus encouraging the precipitation formation during solidification of casting [22]. The solubility data can be inferred from the Mg-Si phase diagram as shown in Figure 1.3.

Mg_2Si exhibit attributes such as low density (2×10^3 kg/m^3), high melting point (1358.15 K), larger elastic modulus (120 GPa), high hardness (460 HV) and low thermal expansion coefficient (7.5×10^{-6} K^{-1}). Further, Mg_2Si exhibit the pinning effect during grain boundary sliding at elevated temperature thus making the Mg-Al-Si based alloys heat resistant alloys [23-26]. Volkswagen firm firstly utilised these alloys in the 1970s for the engine block and powertrain components [27,28].

However, the major drawback in Mg-Al-Si alloys was their tendency to form insignificant coarse Chinese script Mg_2Si phase, which was attributed to the slow cooling conditions during casting. The coarse and brittle nature of Mg_2Si had a detrimental influence on the mechanical properties and became a major hindrance in the widespread application of Mg-Al-Si series alloys [29,30]. Therefore researchers have been involved in the modification and refinement of the Mg_2Si compound to enhance the mechanical properties of Mg-Al-Si based alloys.

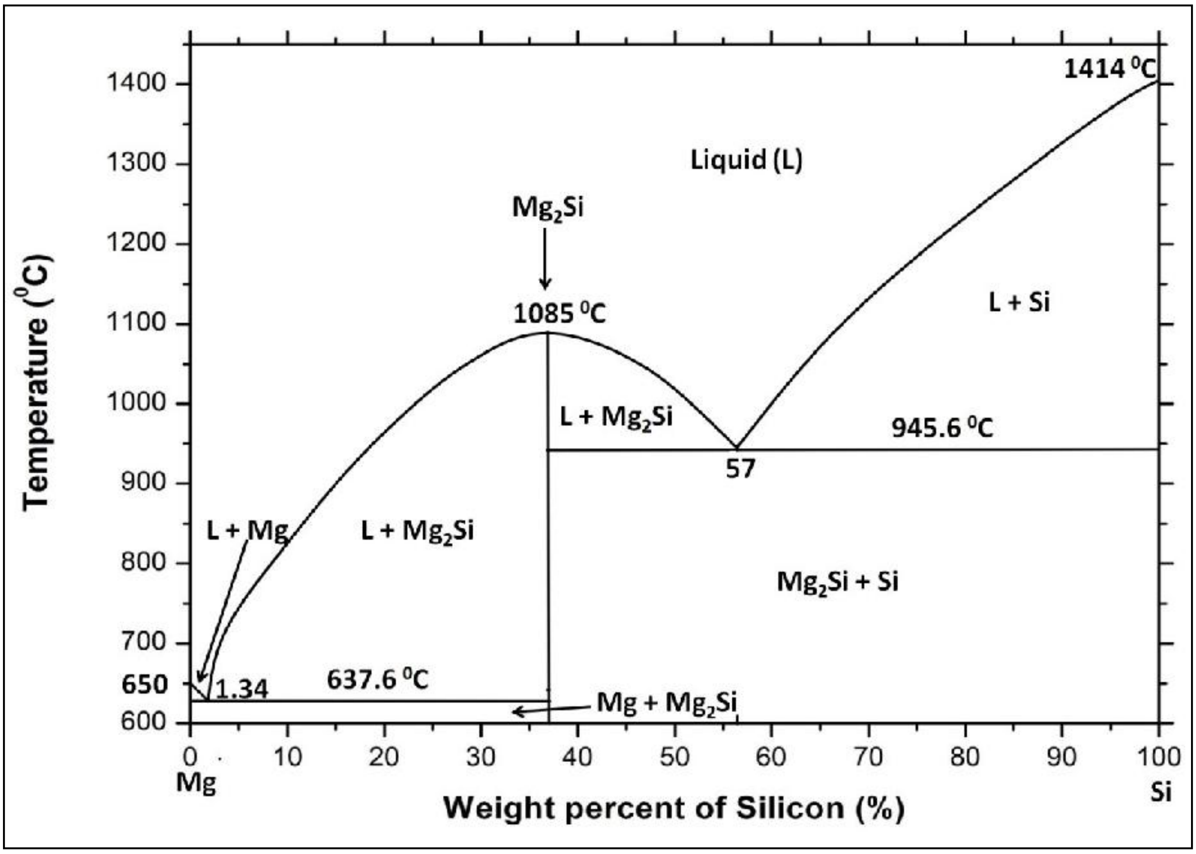

Figure 1.3 Phase diagram of Mg-Si binary alloy [22]

Various conventional techniques such as grain refiners [31, 32], rapid solidification [33], hot extrusion [34], solution treatment [35] and mechanical alloying [36] were developed for modification/refinement of the coarse morphology of Mg_2Si. All these techniques were successful in obtaining the fine Mg_2Si particles and thus enhancing the mechanical strength and ductility of the alloy. However, these techniques display limited grain refinement and also it is hard to obtain a uniform dispersion of Mg_2Si particles. Therefore, researchers have proposed the severe plastic deformation techniques like Equal Channel Angular Pressing (ECAP) [37, 38], Cyclic Extrusion Compression (CEC) [40], High Pressure Torsion (HPT)

[39], Repetitive Upsetting (RU) [41] and Cyclic Closed-Die Forging (CCDF) [42, 43] to overcome the shortcomings of conventional methods through morphological modification of Mg_2Si. SPD techniques impose large strains in the material during deformation which is sufficient in achieving the breakage of Mg_2Si into fine particles and thus attaining their uniform dispersion in the matrix.

1.4 Severe Plastic Deformation (SPD) techniques

The most acceptable approach for achieving Ultra Fined Grained (UFG) structure from a coarser one is the application of severe plastic deformation phenomena. UFG resulted in refined microstructure and enhanced mechanical properties. As there is not much variation in the overall dimensions of the component when subjected to SPD, therefore it can be applied multiple times to achieve a very high strain rate. SPD yields components with high density, thus suitable for aerospace, automobile and defence applications [44, 45]. Some of the important SPD techniques which are in practice currently for the production of UFG materials are ECAP, HPT, RU, CEC and CCDF. The principle of different SPD techniques is discussed in the upcoming section.

1.4.1 Equal Channel Angular Pressing (ECAP)

In this technique, a fine lubricated sample is pushed through an angular die having channel angle θ with the help of a plunger. The sample experiences high shear strain rate at the curvature of the die. Since the dimension remains unaffected, the plunging can be done multiple times to achieve exceptionally high strains with an equiaxed grain structure. The basic principle of ECAP is shown in Figure 1.4

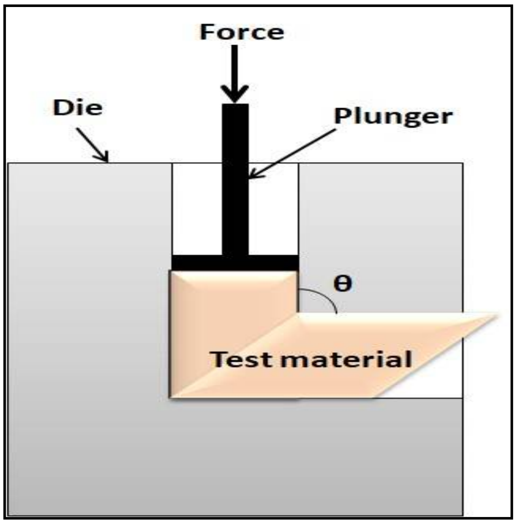

Figure 1.4 Schematic illustration of ECAP technique [37,38]

1.4.2 High Pressure Torsion (HPT)

In this technique, a specimen in the shape of a disc is located inside the cavities of the upper and lower anvil. In HPT method, sample is subjected to shear deformation through the normal force on the top anvil and twisting force on the bottom anvil. Figure 1.5 depicts the basic principle of HPT.

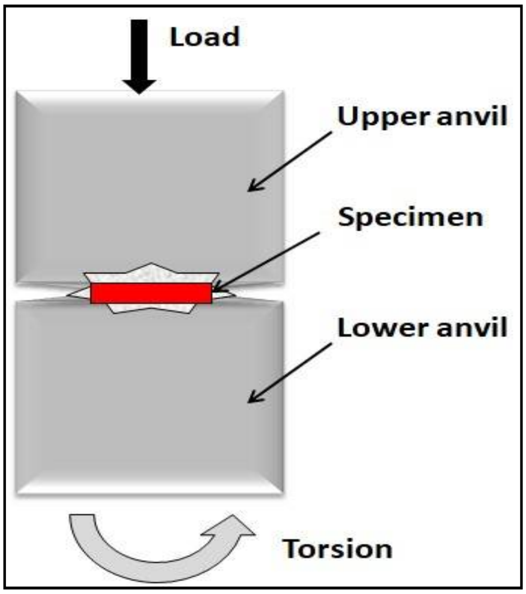

Figure 1.5 Schematic representation of HPT technique [39]

1.4.3 Cyclic Extrusion and Compression (CEC)

In this method, component is made to pass from one cylindrical chamber to another having the same diameter of 'd_o' through a die of diameter d_m (d_m<d_o) as depicted in Figure 1.6. The grain size reduction from nano to micro-level is achieved in this technique. The whole process is completed in two stages: extrusion followed by compression [40].

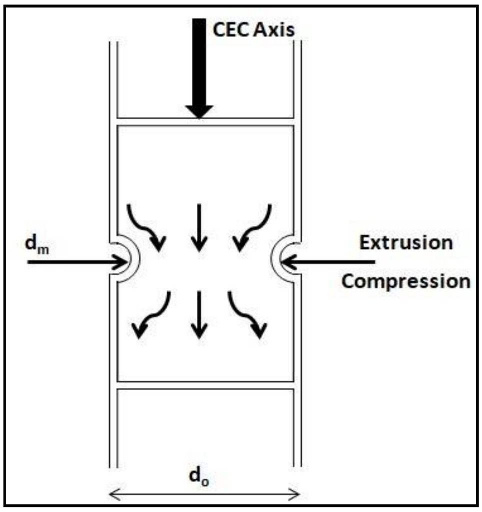

Figure 1.6 Schematic representation of CEC technique [40]

1.4.4 Cyclic Closed Die Forging (CCDF)

CCDF comprises of an upper and lower die; and a punch of the same cross-sectional dimensions. Firstly, the lubricated sample is kept into the upper die and heated to a particular temperature and maintaining for some duration. Now, the sample is pushed into the lower die through a punch at a specified speed. After pressing, the sample is taken out and rotated 90° about Z-axis, and relocated into upper die for subsequent pressing. In this way, specimens are treated with one, three, and five passes, respectively. The basic principle of CCDF is depicted in Figure 1.7. RU technique is also based on the same working principle.

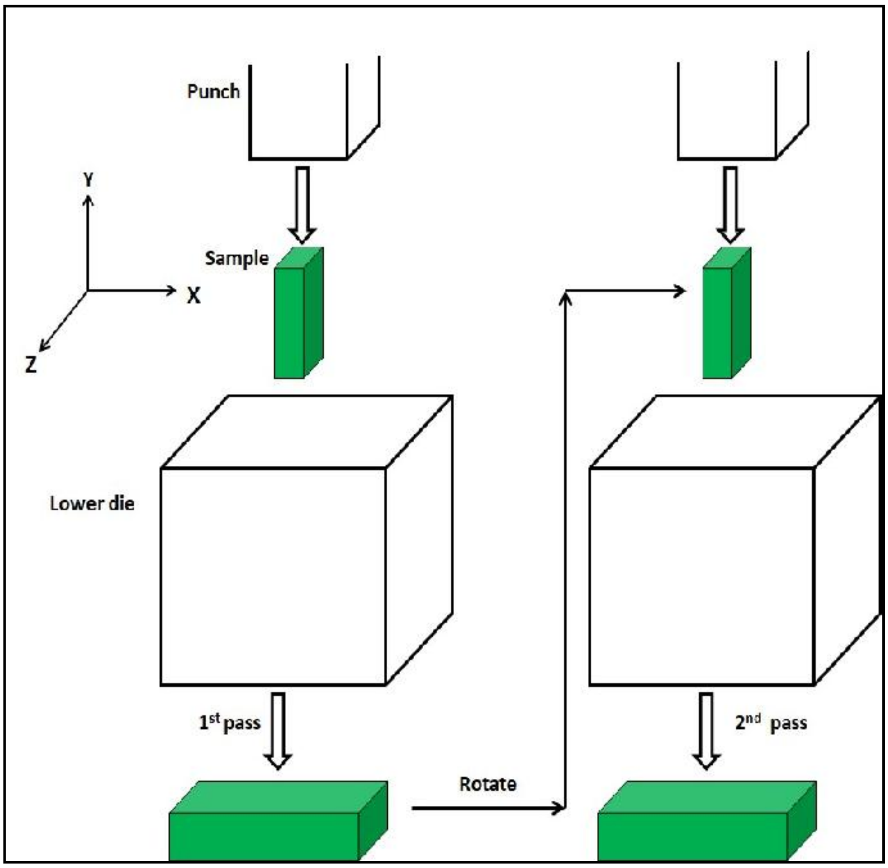

Figure 1.7 Schematic representation of CCDF technique [43]

In addition to the above SPD techniques, the research is going on a newly emerging technique termed Friction Stir Processing (FSP). FSP is a very fast and economical SPD approach since the desired microstructure and properties can be attained in a single pass. FSP having its roots related to Friction Stir Welding (FSW) is the solid-state method which involves microstructural modification through intense plastic deformation of the material resulting in grain refinement and enhanced mechanical properties [46]. Therefore, the present study was performed on the FSP of cast AS21A magnesium alloy. In the upcoming section, the concept and parameters of FSP are discussed in detail.

1.5 Friction Stir Processing (FSP)

Friction stir processing is the novel solid-state technique that utilizes frictional heat and stirring action of tool for microstructural modification. It was developed by Mishra and Z.Y. Ma [47] as a specific method for microstructural modification which follows the basic principles of FSW. The rigorous plastic deformation of the material surface is obtained in FSP by employing a non-consumable cylindrical tool having protruding probe in the cross-section. The rotational and linear movement of the FSP tool produces stirring thus generating heat in the material. FSP build the dynamic recrystallisation phenomena in the material thus achieving a very fine-grained microstructure [48]. Fine microstructure obtained by FSP enhanced the mechanical properties like hardness, ductility, UTS and Yield strength. For instance, FSP resulted in high strain rate super plasticity achieved in commercial 7075 aluminum alloy [49]. FSP technique has also been utilized to fabricate surface composite [50], homogenization of powder metallurgy product and specific property improvement in cast light-weight alloys.

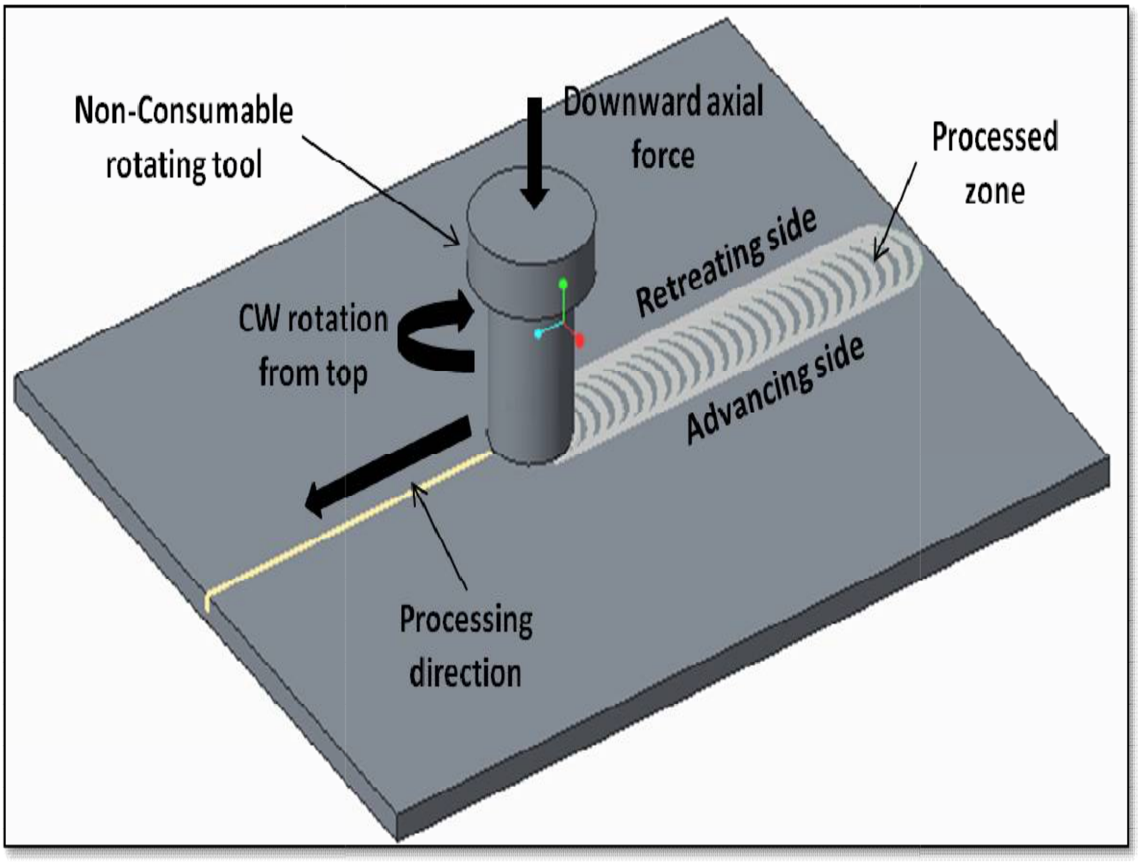

Figure 1.8 Schematic illustration of FSP technique.

1.5.1 Working Principle of FSP

The schematic illustration of the FSP technique is depicted in Figure 1.8. Firstly, the hardened cylindrical tool is rotated at predetermined revolutions. Later, the tip of the rotating tool is inserted into the workpiece for serving the following purpose:

i. Heating and
ii. Plastic deformation of the base material.

The tool's feature consists of a small diameter pin that is intended to cause a vigorous stirring in the workpiece, and a large diameter shoulder whose function is to keep the deformed material beneath it. As the tool penetrates the workpiece surface, the protruding pin of the rotating tool builds frictional heat. This confined heat beneath the tool softens the material, thus permitting further penetration of the tool into the workpiece surface. With the tool rotation, stirring action is induced and material flows in the vicinity of the pin. The penetration depth is managed by the tool's shoulder and pin length. Now, heat is expanded to the enlarged region due to the axial force aided penetration of the tool shoulder. The shoulder avoids the ascent of the flow of material, which is due to the stirring action thus resulting in forging action on the plasticized material. When the tool is fully plunged into the workpiece surface, it then traverses longitudinally across the metal at a specific speed [50].

During FSP, the rotating tool offers repeatedly hot working phenomena, deforming the metal within the narrow area adjacent to the pin and finally directing the material from the advancing region (leading side) of the probe to its retreating region (trailing side). It is noteworthy that the metal never melts since the highest temperature acquired in this particular process is typically 85-90 per cent of the melting temperature. After FSP, material is allowed to reach atmospheric conditions and the processed region shows a refined and homogeneous microstructure. FSP is a thermomechanical metal working phenomenon that modifies only the local characteristics of a material with minimal effect on the overall properties of the material [51].

1.5.2 Processed Region Terminology

Generally, three distinct zones are observed in the processed region of the material when subjected to FSP namely Stirred or Nugget Zone (NZ), Thermo Mechanically Affected Zone (TMAZ) and Heat Affected Zone (HAZ). For instance, the processed zone of aluminium alloy shown in Figure 1.9 exhibits three different zones. The three zones are distinguished based on different microstructural features attained after FSP. These microstructural features in various zones have a significant influence on post-processing mechanical and tribological characteristics. Intense plastic deformation and frictional heating throughout FSP cause initiation of Dynamic Recrystallization (DRX) phenomena resulting in fine-grained microstructural features within the stirred zone. This region is called as nugget or stirred or dynamically recrystallized zone (DXZ). Unique to the FSP process is the formation of a transition zone between the stirred zone and the base metal known as thermo-mechanically affected zone (TMAZ), depicted in Figure 1.9. The TMAZ is subjected to both deformation and temperature during FSP which is insufficient to exhibit DRX phenomena, unlike SZ. Therefore, TMAZ is characterized by deformed and elongated grains. Beyond TMAZ, a heat-affected zone (HAZ) is present whose microstructure is affected by thermal phenomena only exclusive of any plastic deformation. Therefore, sometimes HAZ and base material exhibit similar microstructural features [51, 52].

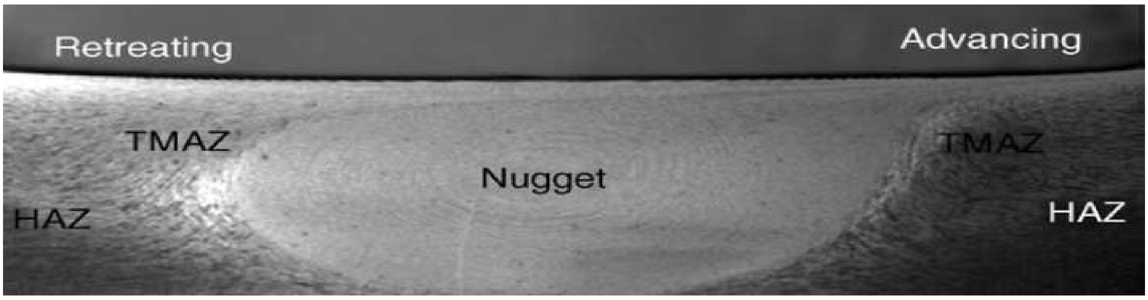

Figure 1.9 Different zones in the cross-section of FSPed 7075Al-T651 [49].

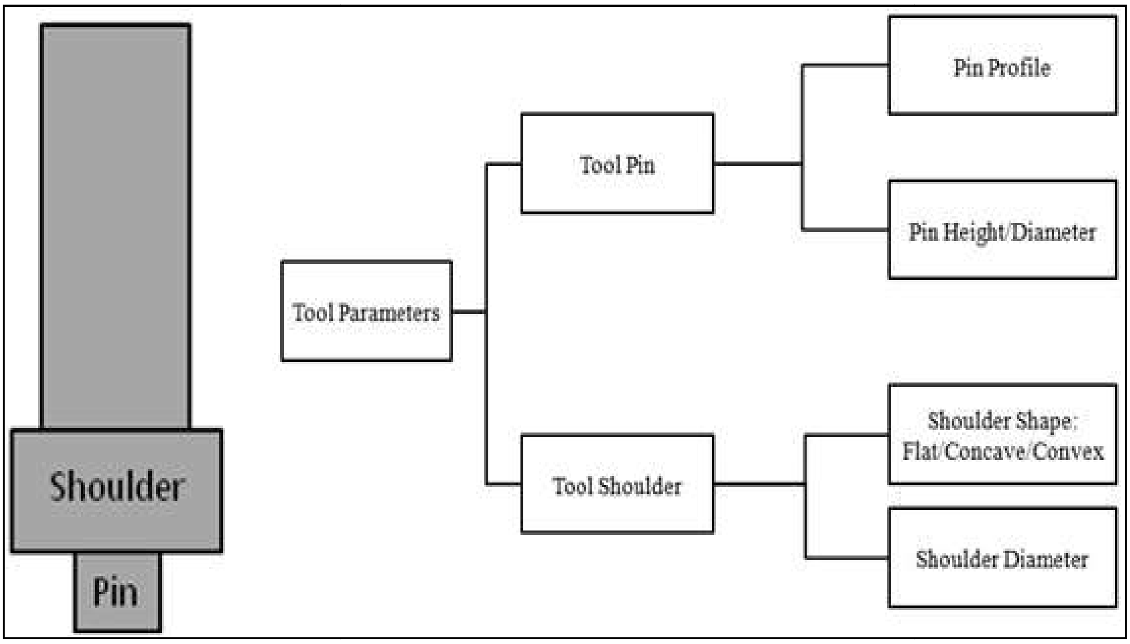

Figure 1.10 Classification based on tool attributes

1.5.3 Process Parameters in FSP

One of the most important aspects of FSP is a selection of process parameters that can yield good results. While fabrication, these parameters are selected optimally and carefully since they have a strong influence on microstructural characteristics, mechanical and tribological properties. These can be classified as: Tool Parameters, Machine Parameters, and Reinforcement/Particle Parameters.

- *Tool Parameters:* FSP tool consists of two important attributes: shoulder and pin, which have a considerable effect on the behaviour of the FSPed surface composite. During fabrication, both are responsible for localized heating and plasticized material flow. Figure 1.10 represents the simple FSP tool with its influencing parameters. Among these parameters majority pin profile, and somewhere shoulder and pin diameter was observed to be varied in almost all surface composite investigations. Tool pin profile can be cylindrical, square, triangular, threaded, fluted, conical, etc. Threaded profile tool is the best suitable choice for surface composite fabrication since it develops defect-free products unlike tunnelling and tool jamming exhibited by fluted profile. Further, a threaded profile effectively mixes the particles from top to bottom resulting in better distribution [53-55]. On the other hand, the square probe can be used instead of the cylindrical probe since it amplifies the mixing of particles due to the pulsating stirring action and high welding torque characteristics [55-57]. Also, tool wear in the case of the square and triangular probe (flat faces) was more compared to circular probe since particles of iron aluminide were observed in the aluminium matrix [56-58]. The shoulder of the FSP tool is responsible for heat generation in the workpiece. Optimum Shoulder Diameter (SD) should be selected while fabricating composite since low strength is shown by too high SD and too low SD due to the annealing effect and insufficient heat generation phenomena respectively [59]. FSP tool pin is responsible for stirring particles in the substrate. A large diameter pin exhibits a defective nugget zone due to insufficient shoulder area for heat generation in the nugget zone while small pin results in clustering of particles [57].
- *Machine Parameters*: Figure 1.11 depicts the various machine parameters involved in composite fabrication. Among these, tool Rotational Speed (RS), Traverse Speed (TS) and FSP passes are the major influencing parameters while fabricating the composite. The tool rotation leads to stirring of softened material around the pin while the linear movement of the tool throws the plasticized material from advancing side to retreating side of the pin

and ultimately ceases the processing. During surface composite fabrication, RS and TS of the FSP tool exhibit an inverse effect on the grain size and hardness of composite. An increase in RS of tool results in more heat generation thus leading to grain growth and reduction in surface hardness while the increase in tool TS results in less heat generation thus restricting grain growth and increase in hardness [60-64]. In addition to this, high tool RS also exhibits a homogeneous distribution of nano particles without any particle agglomeration thus accelerating the pinning effect of particles while high TS exhibit defect in the composite [53, 56, 65]. Another important parameter, FSP passes, depicts similar behaviour like RS, i.e., more no. of FSP passes avoid particles clustering resulting in significant grain refinement and increase in strength [53-56, 58, 61, 64-69]. There is not sufficient literature available in the case of an FSPed surface composite having axial force as a variable. However, Langari et al. [70] reported that axial force (F) is minimum at low TS, i.e. $F \propto TS$ and best quality weld was achieved at high RS and low TS, unlike previous results. Further, the effect of Penetration Depth (PD) and tilt angle on AZ91/SiC composite was studied by Asadi et al. [62] and their optimum values were determined. FSP integrated with cooling arrangement restricted the excessive grain growth during processing as shown by [66, 69].

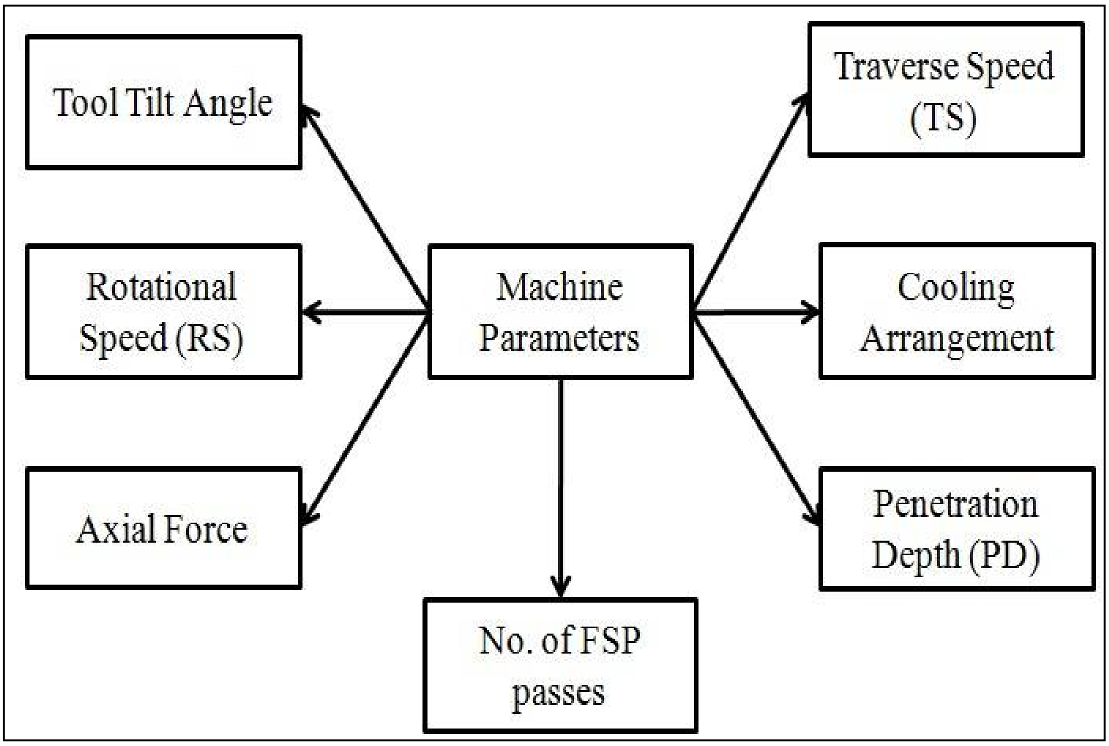

Figure 1.11 Classification based on machine attributes

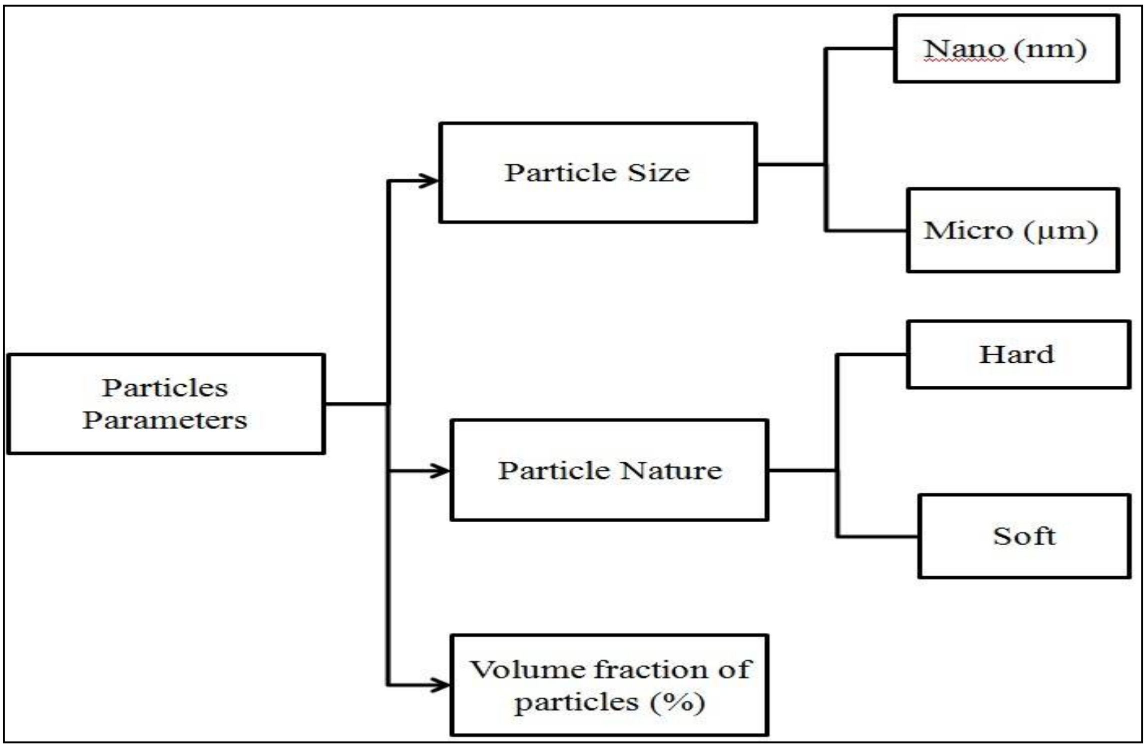

Figure 1.12 Classification based on particle attributes

- Particle/Reinforcement: Figure 1.12 depicts the parameters based on particle nature, size and quantity. Nano-size particles are usually employed while fabricating surface composite. Nanoparticles based composites display improved mechanical properties when compared to micro ones, only if the uniform dispersion of nano particles in the matrix is achieved since uniform distribution impedes the grain growth resulting in high strength and hardness. Therefore the use of nano particles along with high RS and large no. of FSP passes is very necessary for achieving the defect-free and high hardness surface composite [71-73]. However, nano particles are costly and exhibit clustering, unlike micro particles. Increasing the fraction of reinforcement particles (usually expressed in volume %) in the substrate results in enhancement of hardness and UTS while the reduction in wear rate and ductility. This is due to the brittle behaviour exhibited by the composite having high vol. % particles [66, 67]. Further advancement in FSPed surface composite technology is the hybrid composite having a combination of hard/hard, hard/soft or soft/soft particles.

CHAPTER 2

LITERATURE REVIEW

Chapter 2 is organized into two sections. In the first section, literature relevant to Mg_2Si morphological features achieved through various conventional and SPD techniques are discussed while the later section pertains to the previous investigations on FSP of light-weight alloys. In addition to this, literature concerning wear analysis in magnesium alloys is also incorporated. The chapter concludes with the Literature gap and research objectives of the current thesis.

2.1 Modification or refinement of Mg_2Si morphology

Literature survey advocates that the size, quantity and morphology of the Mg_2Si compound play an exceptionally vital role in the mechanical and wear behaviour of Aluminium and Magnesium-based cast alloys. Wang et al [37] reported the breakage of coarse Chinese script Mg_2Si into small particles with uniform dispersion during ECAP of an AZ31-0.5Si alloy which resulted in the significant improvement of ductility. Guo et al [41] performed CCDF on AZ31-Si composite and attained the fragmentation of Mg_2Si into fine particles that resulted in enhanced yield strength and elongation. Kumar et al. [74] reported that the hard and coarse brittle primary Mg_2Si particles present in hyper eutectic Mg–Si alloys make them a superior wear resistance candidate as compared with hypo eutectic alloys. Kondoh et al. [75] synthesized Mg_2Si particles reinforced Mg composites followed by its wear characterization under oil lubrication conditions. The composite sample exhibited the abrasive wear mode since deep plough marks were observed on the sample worn surface, which might be credited to the hard feature of Mg_2Si particles. Pourfallah et al. [76] found less wear in Al–Mg_2Si–3% Ni in-situ synthesized composite when treated with the SIMA process. The Mg_2Si globular shape and its uniform distribution achieved post-SIMA process significantly enhanced the wear resistance of in-situ composites. Soltani et al. [77] studied the wear behaviour in Al–Mg_2Si in situ synthesized composite when subjected to hot extrusion. The extrusion process reduced the size of Mg_2Si particles, thus resulting in their uniform dispersion. The extrusion produced small size Mg_2Si particles that were attributed to the reduced wear rate in extruded samples. Wu et al. [78] investigated wear characteristics in Nd modified Al– Mg_2Si in-situ composite. The Mg_2Si morphology alteration and size refinement obtained after Nd addition contributed to the improved wear behaviour of the in-situ composite. The literature relevant to Mg_2Si morphology is also summarized in Table 2.1.

Akyuz et al. [79] investigated the features of AS series magnesium alloys and reported that the Mg_2Si presence in the alloy had a strong influence on the wear and machining properties.

Table 2.1 Summary of the investigations pertaining to Mg_2Si morphology

Reference	Processing method	Material	Results
Wang et al [37]	ECAP	AZ31-0.5 Si	Breakage of coarse Chinese script Mg_2Si into small particles with uniform dispersion resulted in the significant improvement of ductility.
Gan et al [38]	ECAP	Mg-3.2Si	Grain structure and eutectic morphology of Mg_2Si particles were refined, thus enhancing the strength of the material
Zhang et al [40]	CEC	Mg-9Al-6Si	Most of the Mg_2Si particles were refined and have an average size less than 20µm after 12 CEC passes
Guo et al [43]	CCDF	AZ31-1.7%Si	Fragmentation of Mg_2Si into fine particles that resulted in enhanced yield strength and elongation.
Metayer et al [42]	CCDF	Mg-Si	Wear resistance improved with more CCDF passes which were attributed to the refined morphology of Mg_2Si.
Kumar et al [74]	Casting	Mg-Mg_2Si composite	Hard and coarse brittle primary Mg_2Si particles present in hyper eutectic Mg–Si alloys make them a superior wear resistance candidate as compared with hypo eutectic alloys.
Kondoh et al [75]	Casting	Mg-Mg_2Si composite	The composite sample exhibited the abrasive wear mode since deep plough marks were observed on the sample worn out surface, which can be credited 8 to the hard feature of Mg_2Si particles.

Pourfallah et al [76]	Casting followed by SIMA	Al–Mg_2Si–3% Ni in-situ synthesized composite	The Mg_2Si globular shape and its uniform distribution achieved post-SIMA process significantly enhanced the wear resistance of in-situ composites.
Soltani et al [77]	Casting followed by hot extrusion	Al–Mg_2Si in-situ synthesized composite	The extrusion process reduced the size of Mg_2Si particles, thus resulting in their uniform dispersion. The extrusion produced small size Mg_2Si particles that were attributed to the reduced wear rate in extruded samples.
Wu et al [78]	Grain refiner	Nd modified Al– Mg_2Si in-situ composite	The Mg_2Si morphology alteration and size refinement obtained after Nd addition contributed to the enhanced wear behaviour of the in-situ composite.
Shou-qiu et al [80]	Grain refiner	Al-10%Sr modified Mg-4%Si alloy	The addition of a grain refiner alters the Chinese morphology of Mg_2Si to a polyhedral shape. Also, the average size of the Mg_2Si phase was found to be decreased from 46μm to 16μm.

2.2 FSP of light-weight alloys

FSP can be employed for improving the characteristics of lightweight materials by altering their surface in two ways. Firstly, normal FSP of material exhibited improved mechanical properties compared to the parent material, which can be further extended to enhanced tribological properties [51]. Secondly, the newly revamped FSP method is synthesizing a material with hard reinforcements forming surface composites [50]. The present review is divided into two sections, where each section is concerned with the mechanical and wear investigations done on light-weight materials subjected to normal FSP and surface composite approaches respectively.

2.2.1 Characterization of light-weight alloys subjected to normal FSP approach

Normal FSP or simple FSP involves the intense plastic deformation of specimen resulting in high strain rate leading to recrystallization of grain structure and improvement in mechanical properties. Further, it can be extended to improvement in tribological properties. In recent times, various studies have been conducted to predict the mechanical and wear behaviour of lightweight metals when subjected to FSP. It has been reported that FSP was effective in achieving significant grain refinement along with enhanced mechanical properties like tensile strength and ductility. Further, FSP approach was effectively utilised in modifying the morphology of intermetallic compounds present in the alloy matrix either through their breakup and dissolution ($Mg_{17}Al_{12}$ [81, 82], $Mg_{12}Nd$ [83], Mg_3Zn_2 [84]) or their fragmentation into fine particles (Al_2Ca [85], Al-RE [86]). Mahmoud and Mohamed [87] studied the consequence of FSP on the dry sliding wear behaviour of the as-cast A413 aluminium alloy. It was found that FSP significantly enhanced the wear resistance of A413 alloy. However, the wear resistance was found to have an inverse relationship with the rotational speed while direct relation with the traverse speed of the tool. Zahmatkesh et al. [88] investigated the tribological behaviour of FSPed Al2024 alloy. FSP was found to be more advantageous in enhancing the wear behaviour. Less wear rate was found due to lower COF and high microhardness value of 110 Hv. Abdi Behnagh et al. [89] studied the wear behaviour of the FSPed Al5083 alloy. FSPed specimen exhibited less wear rate and COF (0.35) compared to base metal (0.62). Reddy and Rao [90] examined the wear behaviour of as-cast Al356 alloy. The important findings were that the wear rate of as-cast alloy exhibited a higher wear rate of 0.216 µm/s and COF of 0.63 compared to an FSPed alloy having a rate of 0.0.14 µm/s and COF of 0.15. Alidokht et al. [91] investigated the wear behaviour of FSPed A356 cast aluminium alloy. FSP of A356 alloy results in enhancement of wear resistance to a great extent. Further, samples processed at higher rpm exhibited a low wear rate compared to lower 9 rpm processed samples. Hybridization of abrasion and delamination wear mechanism was observed for both FSPed (shallow grooves) and as-cast (deep grooves) A356 samples. Arora et al. [92] studied the wear behaviour of FSPed AE42 alloy at three unlike sliding speed of 0.33, 1 and 3 m/s while three different loads of 5, 10 and 20 N. Highest wear rate was observed at the lowest velocity and maximum load, i.e., wear resistance increases with increase in sliding velocity and reduction in normal load. Conversely, the highest COF was observed at the lowest load and lowest sliding velocity for both conditions of the AE42 alloy. The wear rate and COF of FSPed AE42 alloy were found to be lower compared to that of base alloy for all wear test conditions. Further, a similar wear mechanism was exhibited by both conditions of the AE42 alloy. Abrasion, oxidation, and delamination along with plastic deformation (PD) were the major wear mechanisms involved during the investigation. It was revealed that oxidation and abrasion were the dominant wear mechanism at low sliding velocity, while delamination along with PD at higher sliding velocity. The literature relevant to the FSP of lightweight alloys is briefed in Table 2.2.

Table 2.2 Summary of the investigations pertaining to light weight alloys subjected to normal FSP approach

Reference	Material	Results
Wen et al [81]	AZ31 Mg alloy	• FSP resulted in the significant grain refinement, homogenization; and dissolution and breakup of coarse eutectic morphology of β-$Mg_{17}Al_{12}$ intermetallic in the magnesium matrix. • The mechanical behavior of AZ31 Mg alloy is improved by increasing the number of FSP pass. The strength achieved in single-pass and the two-pass specimens were found to be increased by 43 and 82 MPa while ductility increased by 4.3% and 11.9%, respectively. The fractured tensile specimen of FSPed AZ31 alloy exhibited ductile characteristics.
Feng and Ma [82]	Mg-Al-Zn	• FSP causes fragmentation and dissolution of coarse eutectic β-phases precipitates dispersed at grain boundaries, thus achieving significant grain refinement and homogenization in the magnesium matrix. • FSPed Mg–Al–Zn specimen exhibited improved mechanical properties like tensile strength of 337 N/mm^2 and % elongation of 10.
Xing-hao and Bao-lin [93]	AZ61 Mg alloy	FSP followed by rapid cooling facilitated in attaining the UFG microstructure in AZ61 Mg alloy, thus exhibiting remarkable enhancement of about 3 times in the microhardness (120-130 Hv).
Zheng et al [83]	Mg-2.0Nd-0.3Zn-1.0Zr	FSP causes absolute dissolution of the $Mg_{12}Nd$ phase in the base substrate and grain refinement of the extruded alloy which leads to enhanced tensile properties. The Vickers hardness of processed zone in all studied FSPed

		specimens is higher than that of the parent material. Elongation was remarkably improved from 13.0% to 24.5%
Ma et al [84]	Cast Mg and Al alloy	FSP resulted in the fragmentation of coarse eutectic network and secondary phases, dissolution of coarse precipitate, refinement of matrix grains, and elimination of casting defects, thereby enhancing the mechanical behaviour of the cast Mg and Al alloy.
Zhang et al [85]	Mg–6Al–3Ca–0.5RE–0.2Mn	Due to FSP, the base material coarse microstructure was replaced with the fine dispersion of Al_2Ca particles and the refinement of grain structure. The Microhardness of the FSPed zone was found to be higher than that of the thixomoulded Mg alloy.
Ramesh et. al [94]	Al-5086-O	• The hardness is increased in the FSP specimen due to the reduction of grain size 48μm base metal to 4-6μm in the FSPed specimen. • Ductility values are better in all FSP processing conditions in comparison with base metal in both longitudinal and transverse ways.
Kwon et al [18]	AA 1050	The tensile strength and hardness of the FSPed zone increased 37% and 46% respectively in comparison to the unprocessed zone at the lower rotational speed at 560rpm.
Rayes et al [96]	AA6082-T651	• Increase in the number of passes in the stir zone the grain size increases and the tensile strength of material was decreased at a given traverse speed. • With the increase in traverse speed, the strength of the specimen was increased. While with the increase in rotational speed, mechanical property of the stir zone was insignificant due to grain coarsening.
Kumar et al [97]	ZK60 Mg alloy	FSPed specimen exhibited minimum wear rate at all tested conditions, which was attributed to the FSP microstructural refinement phenomena. Abrasion,

		delamination, oxidation was the major wear mechanisms found responsible.
Cao et al [98]	Mg-Nd-Y	FSPed Mg alloy microstructure was characterized by the average grain size of 2.7 μm while very fine grains were obtained in the case of FSP followed by cooling, having an average size of 1.9 μm. The respective values of YS (MPa), UTS (MPa), and % elongation were observed to be 281 (or 270), 297 (or 291), and 20.2 (or 7.4) for FSPed sample (with/without cooling) as compared to 180, 182 and 2.6 respectively.
Cavaliere et al [99]	AM60B Mg alloy	FSP causes an increase in mechanical properties due to strong grain refinement and disappearance of casting defects. Ductile characteristics are shown in FSPed samples due to the presence of fine dimples in fractography.
Wang et al [100]	Mg-Zn-Y-Zr	FSP leads to significant grain refinement, dissolution and distribution of eutectic network of Mg_3Zn_6Y, thus resulting in enhanced strength and ductility. The mechanically activated effect of FSP promotes the transformation of the Mg_3Zn_6Y phase to $Mg_3Zn_3Y_2$.
Li et al [101]	WE43 Mg alloy	Mg-Y-Nd coarse second phases in the as-cast alloy were transformed into fine particles due to the intense stirring action of FSP; thus exhibiting improved mechanical properties at a higher rotational speed.
Xiao et al [102]	Mg-Gd-Y-Zr	FSP improved the mechanical behaviour of cast Mg alloy; particularly ductility via fundamental dissolution of coarse $Mg_5(Gd,Y)$ networks and the remarkable grain refinement.

2.2.2 Characterization of light-weight alloys subjected to surface composite approach of FSP

Surface composite fabricated by FSP is the newly developed approach for surface modification. In this approach, hard and brittle ceramic particles such as Al_2O_3, SiC, CNTs, Gr, MoS_2 etc. are reinforced, individually or in combination, with the light-weight alloy matrix to form mono or hybrid surface composite.

The wear being a surface characteristic is entitled to surface treatment such as laser remelting, gas tungsten arc hard facing, High-Velocity Oxy-Fuel (HVOF) coating, plasma spraying, etc. to develop a durable wear resistance layer. However, in elevated temperature conditions, liquidation and the formation of harmful phases are some of the common issues encountered with these processes. Moreover, it is vital to manage the influencing parameters to obtain a perfect microstructure. These issues could have been evaded if the processes had been carried out below the melting point range. Hence Friction Stir Processing (FSP) is an appropriate solution for altering surface qualities of as-cast alloys.

FSP is a rapidly growing surface modification technique that utilises a non-consumable hard tool inducing intense plastic deformation material to enhance the strength and wear properties of materials [47, 50]. The current scenario in FSP technology is strengthening the hard/soft particles in the soft matrix to obtain the Surface Composite layer. The surface composite layer obtained through the FSP technique significantly enhanced the wear resistance of light-weight materials like Aluminium, Magnesium and Copper. The literature survey pertaining to enhanced wear properties due to the formation of surface composite layer comprises AA7075/B_4C [103], A4047/$ZrSiO_4$ [104], AZ91/Al_2O_3 [105], AZ31/Fly Ash [106], Cu/TiB_2 [107] etc. All such investigations lead to the formation of ex-situ composites having micron/nano-sized reinforced matrix through the FSP phenomenon. The intense stirring phenomena of FSP helped in uniform dispersion of externally added reinforcements owing to the severe plastic deformation and intense strain rate induced in the material. However, ex-situ composites experience specific issues like interfacial reaction and poor wettability between reinforcement and base matrix, which may be attributed to the surface contamination of reinforcement. The in-situ composites, synthesized within the matrix, overcome the inbuilt problems allied with the ex-situ composites. FSP plays a vital role in the synthesis of in-situ composites such as refinement of in-situ precipitates formed during the transformation cooling of as-cast alloys [86].

Literature survey deals with the investigations done on the mechanical and tribological studies of ductile materials based surface composites developed by Friction Stir Processing (FSP). Ductile materials such as Aluminum, Magnesium and Copper are utilized as a base material in these investigations with a special focus on Magnesium alloys. Process parameters are represented in the upcoming literature Table 2.3 as per the following format:

- Shoulder Diameter/Tool Profile/Tool pin size (diameter, altitude, diagonal)/Tool pin height/Tool Tilt Angle

• TS: Traverse Speed (mm/min), RS: Rotational Speed (RS), PD: Penetration Depth

Table 2.3 Summary of the investigations pertaining to light weight alloys subjected to surface composite approach of FSP

Reference	Material/Particles/ Parameters	Characteristics studied	Results
Jiang et al [71]	• **AZ31** • **SiO_2**: 20 nm • 20/Circular/5 /3.5 • RS: 1200, TS: 50	Influence of SiO_2 particles on grain structure and hardness.	• The distribution of SiO_2 reinforcement resulted in grain refinement and an equiaxed ultrafine grain structure was obtained having less than 1 µm grain size. • The hardness of the AZ31/SiO_2 composite was measured as 90 HV which is nearly two times that of the Mg matrix.
Nia and Nourbakhsh et al [69]	• **AZ31** • **SiC:** 50 nm & **MWCNTs:** diameter: 20-50 nm and length: 10-20 mm • 18/threaded (3 mm pitch)/7/4/3° • RS: 1000, TS: 28 • FSP passes: 4	Study of microstructure, hardness and tensile strength of AZ31 alloy reinforced with 4, 8 and 16 % (v/v) SiC or CNTs using FSP technique having cooling arrangement.	• SiC nanoparticles exhibited better reinforcement characteristics than CNT's for AZ31 due to their more uniformly dispersion in the AZ31 matrix. • Increased micro-hardness value from 67Hv (Base Material) to 108 Hv and 112 Hv for the composite having 16 % CNT and 16 % SiC respectively. • Increasing the fraction of particles increased the yield strength while decreased the ultimate stress and ductility.
Asadi et al [60]	• **AZ91** • **SiC & Al_2O_3**: 30	Effect of FSP passes on the	• The average grain size in the SiC (800 nm) reinforced specimen is

	nm • 15/Square/5/2.5/3° • RS: 900, TS: 63 • FSP passes: 1, 2, 4, and 8	behaviour of SiC and Al_2O_3 particles, microstructure, tensile properties, and hardness and wears properties of FSPed AZ91/SiC and AZ91/Al_2O_3surface composite.	much smaller than the specimen having Al_2O_3 (1.3 μm) after 8 FSP passes. • Non uniform hardness profile in case of 1 pass AZ91/SiC ranging from 90 Hv to 115 Hv while AZ91/Al_2O_3 exhibited average uniform hardness value of 95 Hv in the stirred zone. After 8 FSP passes AZ91/SiC sample exhibited a uniform hardness value of 135 Hv compared to 130 Hv of AZ91/Al_2O_3. • UTS (MPa) and elongation (%) exhibited by 8 passes FSPed AZ91/SiC was 251 and 13.4 while AZ91/Al_2O_3 exhibited 244 and 12 compared to 128 and 6.6 of the base metal. • The inclusion of SiC and Al_2O_3 particles in the AZ91 matrix decreased the wear rate from 17 to 5 ($10^{-5}mm^3/Nm$). • Eight passes FSPedAZ91/SiC and AZ91/Al_2O_3 composite exhibited average friction coefficient of 0.48 and 0.45 respectively.
Asadi et al [62]	• **AZ91** • **SiC**: 5 μm • 15/Square/5/2.5/2.5°-4° • RS: 710-1400,	Effect of RS and TS, PD and tilt angle on the formation of defects,	• High PD leads to the sticking of base material to the FSP tool due to the transformation of the sliding mode of friction to the sticking mode of friction. While

	TS: 12.5-80 • PD: 0.15-0.45	mechanical properties and microstructures.	a longitudinal crack develops along the processing area at a small PD value thereby exhibiting tunnelling type of abnormalities in the stirred region. • Optimum PD were 0.40, 0.30 and 0.22 mm for 3.5°, 3° and 2.5° tilt angle, respectively, when RS and TS conditions were 1120 rpm and 63 mm/min, respectively. • TS and RS had an inverse effect on grain growth. An increase in TS leads to reduction in grain size and vice-versa for rotational speed. • Grain structure was refined and had an average size of 7.17 µm thus improving the microhardness value from 63 to 96 HV.
Azizieh et al [53]	• **AZ31** • **Al_2O_3**: 35, 350 and 1000 nm • 18/Circular/6/5.7/2°, 18/Threaded/6/5.7/2° (thread of 1 mm pitch) and 18/Fluted/6/5	Effect of pin profile, rotational speed, no. of FSP passes and particle size on the AZ31/Al_2O_3 nano-composite fabricated by FSP.	• Among non-threaded and three flute profile tool, the threaded tool profile was found to be the best. • The average grain size of the composite was found to be increased on increasing the RS from 800 to 1200 while the opposite effect was observed on increasing the FSP passes from 2 to 4. • The grain size was effectively

	.7/2° (3 flutes of 1.5 mm depth) • RS: 800, 1000 and 1200; TS: 45 • FSP passes: 2-4		refined in the case of nanocomposite compared to composite with micro-particles, simple FSP and base matrix. • AZ31 sample fabricated with nano particles was found to have the highest hardness value of 90 Hv compared to rest of investigated particles.
Balakrishnan et al [108]	• **AZ31** • **TiC**: 4 μm • 18/Square/6/5 • RS: 1200, TS: 40 • Axial force: 10 kN	Effect of TiC particles (0, 6, 12 and 8 vol. %) on microstructure.	Uniform distribution of TiC particles without agglomeration. Further, no interfacial reaction was observed between the Mg substrate and the TiC particles.
Dadashpour et al [67]	• **AZ91C** • **SiO_2**: 10-15 nm • 18/Square/6/6/3° • RS: 1250, TS: 40 • FSP passes: 1-3	Investigation of mechanical properties and fracture mechanism of the FSPed AZ91C/SiO_2 composite.	• AZ91C/SiO_2 synthesized with 3 FSP passes exhibited the least grain size of 4 μm while highest UTS of 240 MPa and 130 Hv hardness. • More passes result in the elimination of particles clustering and homogeneous distribution of particles. • The presence of nano particles in base material reduced the fracture toughness while it was improved by increasing the no. of FSP passes.
Lu et al [72]	• **AZ31** • **Al_2O_3:** 50 nm	Hybrid and individual effect	• All individual and hybrid fabricated composites were found

	and **CNTs:** dia: 30 nm and length: 30 µm • 20/Conical Frustum/5.5-3.5/5/0.5° • RS: 1050, TS: 33.4 • FSP passes: 4	of reinforcement on tribological behaviour of AZ31 Mg alloy.	more wear resistance than the base matrix. • Individual n-Al_2O_3 particles wear was lower than that of independent CNTs; however, the former friction coefficient was higher. • The wear and friction coefficient of the composite having 0.1% $A1_2O_3$ and 0.2% CNTs was lower than those of other studied composites when load was higher than 1.94 N/mm^2 while of the composite having 0.2% $A1_2O_3$ and 0.1% CNTs was less than others when the load was less than 1.32 N/mm^2.
Faraji and Asadi et al [56]	• **AZ91** • **Al_2O_3**: 30 nm • 15/Circular/5/3/3°, 15/Square/5/3/3° • RS: 900-1200, TS: 40-80 • FSP passes: 1-2	• Effect of tool pin profile, RS/TS ratio, and FSP passes on the microstructure and hardness of the fabricated nano composite. • Influence of nano Al_2O_3 particles on hardness and wear resistance.	• FSP performed at 900 rpm, 40 mm/min and employing square pin feature tool was found to be an optimum condition for fabricating the sound surface composite layer. • Due to the nonexistence of pulsating stirring action in the square profile FSP tool; it was intricate to achieve a homogeneous distribution of particles even at lower TS. • Higher RS/TS ratio results in improved distribution of Al_2O_3 nanoparticles and accordingly smaller grain size of the surface

			composite layer. • An increase in the number of passes increases microhardness. • Alumina particles decreased the volumetric wear rate (in mm^3/Nm) from 0.0175 to 0.0025, which is almost 7 times.
Khayyamin et al [61]	• **AZ91** • **SiO_2**: 10 nm • Square/6/4/3° • RS: 1250, TS: 20,40, and 63 • FSP passes: 1-3	Effect of different TS and FSP passes on microstructure, hardness and tensile properties of the AZ91/SiO_2 nanocomposite.	• An increase in TS leads to decrease in grain size from 140 µm of base metal to 8.27 µm of the composite produced while the increase in microhardness from 65 to 108 HV. • An increase in FSP passes from 1 to 3 results in uniform distribution of particles and an increase of hardness from 65 to 124 HV. • At TS of 63 mm/min, UTS of 192 MPa and elongation of 12.4% was achieved in AZ91/SiO_2 composite compared to 139 MPa and 6.74% of base metal. Maximum UTS of 192 MPa and elongation of 12.5% was achieved in 3 passes FSPed AZ91/SiO_2 composite.
Navazani and Dehghani et al [73]	• **AZ31** • **TiC**: 5 µm • 14/Square/6/2.7/2.5° • RS: 1250, TS: 50	Effect of TiC particles on grain structure and hardness.	• Grain morphology was refined due to dynamic recrystallization and the presence of TiC particles. • The pinning effect of TiC restricted grain boundary movement and therefore grain

			growth was reduced. The average grain size was found to be decreased from 40μm to 12μm. • Average hardness was found to be enhanced from 50Hv to 79Hv on the addition of reinforcement.
Morisada et al [109]	• **AZ31** • **MWCNTs:** diameter: 20-50nm and length: 250 nm • 12/Circular/4/1.8 /3° • RS: 1500, TS: 25-100	• Behaviour of reinforcement particles. • Effect of TS on the distribution of MWCNTs.	• Grain refinement by FSP, pinning effect and high strength of particles increased hardness. The maximum hardness obtained was 78 Hv compared to 55Hv of the base alloy. • Lower TS exhibited fine distribution of MWCNT particles. A good dispersion was obtained at 25 TS and 1500 RS.
Morisada et al [65]	• **AZ31** • **SiC**: 1 μm • 12/Circular/4/1.8 /3° • RS: 1500, TS: 25-200	• Effect of FSP with the SiC particles on microstructure and hardness. • Effect of heat treatment on grain structure.	• SiC particles aided in the grain refinement through FSP. The maximum hardness obtained was 80 Hv compared to 48 Hv of the base alloy. • The fine-grain structure of FSPed AZ31 becomes unstable above 300°C while that of AZ31 reinforced with SiC was not influenced by the heat treatment.
Navazani and Dehghani et al [110]	• **AZ31** • **ZrO_2**: 40 nm • 14/Circular/6/2/2.5° • RS: 1250, TS: 20 • FSP passes: 4	Effect of ZrO_2 nanoparticles on microstructure evaluations and mechanical properties.	• The introduction of ZrO_2 particles in the AZ31 matrix resulted in grain refinement from 40 μm to 3 μm. • Hardness improved from 54 Hv of base metal to 87 Hv of FSPed AZ31/ZrO_2 surface composite.

Sun et al [111]	• **AZ63** • **SiC**: 40 nm • 20/Circular/6/4.2 /2.5° • RS: 1500, TS: 20	Influence of FSP reinforced SiC particles on the microstructural and mechanical features of AZ63 alloy.	• AZ63/SiC surface composite was successfully fabricated through FSP devoid of any sign of particles interfacial reaction and agglomeration. • The FSPed composite exhibited a hardness of 109 HV and tensile strength of 312 N/mm^2 which was significantly higher than that of base metal.
Reddy et al [112]	• **ZM21** • **SiC** and **B_4C** • 20/Circular/6/3/3 ° • RS: 1200, TS: 50	Effect of SiC or B_4C particles introduced by hole filling and closing technique on the wear behaviour of ZM21 Mg alloy.	• ZM21/B_4C surface composite exhibited relatively higher hardness compared to ZM21/SiC. • Less wear rate (friction coefficient of 0.025) was revealed by ZM21/B_4C compared to parent metal (friction coefficient of 0.2).
Abbasi et al [68]	• **AZ91** • **SiC** & **Al_2O_3**: 30 nm • 15/Circular/4/2.5 /2° • RS: 950, TS: 42 • FSP passes: 1, 2 and 4	Effect of FSP pass on mechanical and wear properties of FSPed AZ91/SiC and AZ91/Al_2O_3 composite.	• FSPed AZ91/SiC exhibited greater strength and ductility compared to AZ91/Al_2O_3 due to a more uniform dispersion of SiC particles. • Increasing the FSP passes to 4, both types of composites exhibited better distribution, less agglomeration of particles and higher hardness compared to base AZ91 alloy. • Both particle reinforced AZ91 alloy almost exhibited the same wear rate at all FSP passes. Moreover, the wear rate was

			found to reduced with an increase in no. of FSP passes from 1 -3. • Fewer fluctuations in friction coefficient (about 0.45) were observed in the case of 4 passes FSPed surface composite.
Haghani et al [113]	• **AZ31** • **SiC**: 50 nm • 18/Circular/7/4/2 ° • RS: 1000, TS: 28 • FSP passes: 4 • Cooling: Yes	Effect of SiC particles (4, 8 and 16 %) in 100 % overlap and 4 % particles in 50 % overlap on microstructure, hardness and tensile strength of AZ31 alloy.	• In 100 % overlap, grain structure was refined from 18 µm of base metal to 6.4 µm of FSP without SiC and further to 2.04 µm (4 %), 1.65 µm (8 %), 1.15 µm (16 %) of AZ31/SiC surface composite while 50 % overlap FSP with 4 % SiC exhibited grain size of 2.04 µm. • Hardness was increased from 67 Hv to 112 Hv for a composite having 16 % SiC particles. • With the addition of particles, yield stress increased from 110 MPa to 123 Mpa for 16 % SiC reinforced composite while the reduction in % elongation and UTS.
Naser and Darras [63]	• **AZ31B** • **SiC**: 250 µm • 15/Circular/5/4/2 ° • RS: 800-2000, TS: 25-200	Effect of combinations of tool RS and TS on grain size and hardness of the AZ31/SiC composite produced by FSP.	• The average grain size was found to be decreased from 3.5 to 1.3 µm on increasing the TS from 25 to 200 mm/min at a fixed RS of 800. Also, GS increased from 4 µm to 20 µm on increasing the rpm from 800 to 2000 at a fixed TS of 25 mm/min. • Microhardness measured within

			the SZ of FSPed AZ31/SiC was 81-103 Hv which was 37.7 % and 52.3 % higher than the simple FSPed AZ31 and the base metal respectively.
Sharifitabar et al [114]	• **Cast Mg alloy** • **Al_2O_3**: 40 nm and **$ZrSiO_4$:** 1-5 µm • 13.6/Circular/5/3.7/2.5° • RS: 800, TS: 50 • FSP passes: 1-4	Effects of FSP passes and pass sequence on the hardness and wear behaviour of the Mg-$ZrSiO_4$-Al_2O_3 micro/nano-composite.	• A uniform distribution of Al_2O_3 and $ZrSiO_4$ particles were obtained in the SZ after 4 FSP passes. • Maximum hardness of 103 Hv was exhibited by the 2 pass FSPed sample (C4) having intermediate cooling • No considerable effect of FSP pass sequence on the tribological behaviour of the samples (C1, C2 and C3) produced by four FSP passes. Minimum wear rate along with minimum temperature was exhibited by the C4 sample. • The wear mechanism of the SZ varied with no. of FSP passes. Three-body abrasion mechanism was exhibited by sample C4 while two-body abrasion mechanism by samples (C1-C4).
Faraji et al [58]	• **AZ91** • **Al_2O_3:** 3000, 300 and 30 nm • 15/Square & Triangular/5/1.8/3° • RS: 900, TS: 63	Effect of particle size, FSP tool geometry and FSP passes on grain size, microstructure and hardness of	• With the increase in the size of Al_2O_3 from micro to nano, there was a decrease in grain size from 150 to 5.94 µm (square) and 5.63 µm (triangular) while increase in hardness from 70 HV to 103 HV. • Both square and triangular tool

	• FSP passes: 1-3	the Al_2O_3 reinforced AZ91 surface composite.	geometry exhibited a reduction in average grain size and cluster size when more passes were employed. • The triangular profile was better than the square profile since it exhibited better grain refinement (2.16 µm compared to 2.8 µm of the square) and good particle dispersion (1.7 µm avg cluster size compared to 2.5 µm of the square profile).
Lee et al [66]	• **AZ61A** • **SiO_2**: 20 nm • 18/Circular/6/6/2 ° • RS: 800, TS: 45 • FSP passes: 1-4 • Cooling: Yes	Effect of SiO_2 particles (vol. % 5 and 10) and FSP passes on microstructure and mechanical features of AZ61 magnesium alloy.	• Agglomeration of SiO_2 particles was observed with size ranging from 0.1 to 3µm. Also, composites fabricated with more FSP passes exhibited less agglomeration along with the homogeneous dispersion of nano particles. • Sample processed with 4 FSP passes and 10 % SiO_2 particles showed maximum hardness, YS and UTS of 105 Hv, 225 N/mm^2 and 251 N/mm^2 respectively, while ductility achieved was least.
Hashemi and Hussain [55]	• **Al7075-T651** • **TiN**: 30 nm • 16/Tapered Threaded/5-3/3/2.5° (1 mm pitch),	Effect of employing three different FSP tool geometries and FSP passes on the microstructure,	• 4 pass FSP exhibited uniform dispersion of particles and produced defect-free composite compared to 2 pass FSP for all 3 tool geometries. • Al7075/TiN surface composite

	16/Square/5/ 3/2.5° and 16/Triangular /5/3/2.5° • RS: 1250, TS: 40 • FSP passes: 2 and 4	hardness wear characteristic of Al7075/TiN surface composite.	fabricated with 4 pass FSP threaded tool exhibited least grain size of 1.2 µm (78 µm of parent metal) and highest hardness of 173 Hv (160 Hv of base metal). • Further, the threaded tool was found to be the best choice for fabricating Al/TiN as it exhibited the least friction coefficient (45% less than parent metal) and mass loss (60% less than parent metal). • Al/TiN composite experienced abrasion and adhesion wear mechanism while parent metal suffered from severe adhesion mechanism.
Thankachan and Prakash [115]	• **Cu** Alloy • **AlN:** 10 µm • 20/Circular/6/5 • RS: 1000, TS: 30	Effect of different volume fractions (5, 10, 15) of AlN particles on microstructure, mechanical and wear characteristics of FSPed Cu/AlN surface composite	• With the increase in particles %, grain size reduced and microhardness increased to 80-90 Hv value in SZ. UTS and YS also increased from 111 to 173 MPa while ductility reduced from 12 to 8 %. However copper as a base material possessed higher UTS, YS and ductility compared to composite. • The wear rate exhibited a decreasing trend with an increase in AlN %. Also, fluctuations in friction coefficient were large in the case of pure copper compared to surface composite. • With the introduction of

			particles, adhesion wear diminished while abrasion wear dominated.
Alidokht et al [116]	• **Al A356** • **SiC:** 30 µm and **MoS_2:** 5 µm • 20/Threaded /6/3.7/3° (thread of 1 mm pitch) • RS: 1600, TS: 50	Microstructural, hardness and tribological study of FSPed Al-based hybrid composite.	• One FSP pass was sufficient in achieving the homogeneous dispersion of SiC and MoS_2 particles in the stir zone. • FSPed Al-SiC-MoS_2 hybrid composite exhibited hardness between FSPed Al-SiC composite and FSPed Al alloy without particle. • Hybrid surface composite offered maximum resistance to wear which can be attributed to the formation of a mechanically mixed layer.
Narimani et al [117]	• **Al AA6063** • **B_4C:** 7 µm and **TiB_2-**10 wt% Al in situ synth. • 18/Threaded/6/4. 5/2° • RS: 1000 (first 3 passes), 710 (last pass) and TS: 40 • FSP passes: 4	Effect of different ratios of TiB_2 and B_4C on the microstructure and wear resistance of FSPed AA6063 based hybrid and mono surface layers.	• Microstructure analysis revealed that on increasing the fraction of TiB_2 agglomeration of particles occurred. • AA6063-100% TiB_2 mono surface composite layer exhibited the maximum hardness and wear resistance compared to AA6063-100% B_4C mono composite, AA6063-25% B_4C+75% TiB_2 hybrid composite and base Al alloy (with and without FSP). • Presence of Mechanically Mixed Layer (MML) decreased the wear rate of mono/hybrid surface composite layers.

Kumar et al [118]	• **Al5083-O** • **W:** 10 µm • 15/Threaded/4/3.5 • RS: 1200 and TS: 24 • Axial Force: 8 kN	Study of wear behaviour of Al5083 alloy reinforced with metallic Tungsten (W) particles.	• Formation of Al-W intermetallic was avoided. The average hardness of the Al-W composite was found to be 127 Hv in contrast to 91 Hv and 81 Hv for FSPed and base alloy respectively. • Al-W surface composite exhibited mild wear behaviour from lower (Adhesion) to higher load (Oxidation) while the base and FSPed sample showed the transition from mild (Adhesion) to severe wear (Abrasion + Delamination).
Devaraju et al [119]	• **Al6061- T6** • **SiC, Gr and Al_2O_3:** 20 µm • 24/Tapered Threaded/8/3.5/2.5° • RS: 900 and TS: 40 • Axial Force: 5 kN	Effect of reinforcement mixtures (SiC+Gr) and (SiC+Al_2O_3) at vol. the ratio of 8 % and 4 % respectively on microstructure, hardness and wear behaviour.	• The hybrid composite was successfully fabricated with uniform distribution of particle mixtures in SZ by FSP and no defects were observed. • Al-SiC/Gr hybrid composite displayed less hardness of 108 HV compared to 120 HV of Al-SiC/Al_2O_3 while base matrix was having hardness value of 104 HV. • Further Al-SiC/Gr exhibited superior wear resistance and low friction coefficient (0.30) in contrast to Al-SiC/Al_2O_3 having a friction coefficient of 0.36.
Dinaharan et al [120]	• **Cu** • **Rice Hush Ash (RHA):** 5 µm	Study of RHA particles (0, 6, 12, 18% vol.) on	• RHA particles were finely dispersed in the Cu matrix without any formation of particle

	• 24/circular/6/4.5 • RS: 1000 and TS: 40	microstructure and wear behaviour of Cu/RHA CMCs.	agglomeration. • Cu/18% RHA CMCs exhibited finer grain structure unlike the coarse grain structure of pure Cu. • An increase in hardness was observed with an increased quantity of particles and Cu/18% RHA CMC exhibited the highest hardness value of 116 Hv from 64 Hv of base metal. • Wear resistance enhanced with increase in the volume fraction of particles, unlike hardness behaviour. Cu/18% RHA exhibited the least wear rate (in mm^3/m) of 0.000053 from 0.000083 of base metal.
Devaraju et al [64]	• **Al 6061-T6** • **SiC:** 20 µm and **Al_2O_3:** 20 µm • 24/Tapered threaded/8/3.5/2.5º • RS: 900, 1120, 1400 and TS: 40 • Axial Force: 5 kN • FSP passes: 1	Study on the influence of reinforcement and RS on wear and mechanical properties of FSPed Al alloy 6061-T6/(SiC+Al_2O_3) surface hybrid composite and to obtain optimum parameters using Taguchi analysis.	• Optimum conditions obtained were 1120 RS, 8 % and 4 % vol. fraction of SiC and Al_2O_3 respectively. • Microhardness increased owing to high volume fraction of particles while decreased due to high rotational speed. • Tensile properties decreased owing to the high rotational speed and volume fraction of particles. • Presence of MML converts the mechanism from 2 to 3 body thus increasing the wear resistance and minimizing the COF.

Palanivel et al [121]	• **AA6082** • **TiB_2:** 20 µm and **BN:** 200 nm • 18/Threaded/6/5.5 • RS: 1600 and TS: 60 • FSP passes: 2 • Axial Force: 10 kN	Effect of reinforcement combinations of 100 % TiB_2, 50 % TiB_2 + 50 % BN and 100 % BN on microstructure & wear behaviour of hybrid/mono composite.	• FSPed AA6082/(TiB_2+BN) hybrid composite exhibited extensive grain refinement from 39.4 to 6.6 µm and a decrease in wear rate from 23.75 to 13.00 (×10^{-5} mm^3/Nm). Moreover, it also exhibited less wear rate compared to a mono composite of AA6082/TiB_2 (15.50×10^{-5} mm^3/Nm) and AA6082/BN (14.25×10^{-5} mm^3/Nm). • On addition of TiB_2 and BN in AA6082, transition of wear mode was observed from adhesion to abrasion. In other words, the characteristics of wear debris were altered from large platelet structure to a much fine flake. • AA6082/BN mono composite exhibited the least wear of counterface disc compared to mono composite AA6082/TiB_2 and AA6082/ (TiB_2+BN) hybrid composite.
Saravanakumar et al [122]	• **Cu** • **AlN:** 1 µm • 24/circular/6/4.5 • RS: 1000 and TS: 40	Effect of different volume fraction (0, 6, 12, and 18) of AlN particles on microstructural and wear behaviour of Cu/AlN surface composite.	• Uniform distribution of AlN particles in the matrix was observed along with the absence of particle agglomeration. • Cu/18% AlN exhibited the finest grain size compared to the coarse grain size of the Cu matrix. • An increase in microhardness was observed with increased quantity

			of particles and Cu/18% AlN exhibited the highest hardness value of 109 Hv from 64 Hv of base metal. • Wear behaviour enhanced with an increase in the fraction of particles, unlike hardness behaviour. Cu/18% AlN exhibited least wear rate (mm^3/m) of 0.00174.
Selvakumar et al [123]	• **Al6082** • **Mo:** 25 µm • 18/threaded/6/5.8 • RS: 1600 and TS: 60 • FSP pass: 1	Investigation of different volume fraction (0, 6, 12, and 18) of Molybdenum (Mo) metallic particles on microstructure and tensile properties of the FSP aided Al6082/Mo composite.	• Homogeneous distribution of Mo particles in the Al matrix was observed without clustering and segregation. Also, strong bonding between the particle and the Al matrix was there without any pores and intermetallic phases. After FSP, Mo retains its elemental form, unlike hard ceramic particles. • Al/18% Mo exhibited the finest grain size of about 5 µm compared to 32 µm grain size of Al/0% Mo. • Mo particles enhanced the UTS of the composite without any abrupt reduction in ductility. Al/0% Mo exhibited UTS and ductility of 222 Mpa and 24% while Al/0% Mo exhibited 305 MPa and 14% respectively.

2.3 Wear studies in Magnesium alloys

Magnesium alloys, one of the light-weight candidates, own features like remarkable specific strength, excellent thermal and electrical conductivity, functional damping capacity, etc [3-8]. Nevertheless, magnesium alloys lack surface characteristics, particularly wear resistance, which undermines their widespread application. Wear is a common problem encountered in the machinery components when subjected to relative motion. The soft attribute of magnesium alloy makes wear when they make contact with the hard counterpart. The Mg-Al–Zn [124], Rare Earth (RE) [125–127] and Mg-Al–Mn [128] series is the most broadly used and investigated magnesium alloy in the current scenario. Various studies have been performed to examine the wear performance of magnesium alloys in different parametric conditions. Chen et al. [124] identified two wear regimes as mild and severe in AZ91D magnesium alloy by constructing the sliding wear map. The phenomena of critical contact surface temperature controlled the wear transition from Mild to Severe. Selvan et al. [125] observed some of the leading wear mechanisms such as oxidation, abrasion, plastic deformation, delamination, and melting while examining the dry sliding characteristics of cast ZE41A Mg alloy. Lopez et al. [126] observed diverse wear mechanisms in ZE41 magnesium alloy when tested at different sliding velocities. First, the dominant wear mechanism found at low sliding velocities was oxidation with a minimum contribution of delamination and abrasion. At moderate speed, Abrasion became more prevailed along with the oxidation. Finally, at a higher velocity, the primary wear mechanism shifted to delamination and plastic deformation during intermediate and high load values, respectively. An et al. [127] reported that microstructure and mechanical modifications attained due to surface temperature rise during dry sliding significantly influenced the wear behaviour of Mg97Zn1Y2. Taltavull et al. [128] inspected the dry sliding wear characterization in AM50B alloys and constructed a wear mechanism map under different ranges of Normal load and Sliding velocity. Hu et al [129] examined the dry sliding wear behaviour of Mg-10Y-4Gd-1.5 Zn-0.4 Zr on a Ball-on-Flat Tribometer. It was found that the $Mg_{12}Y_1Zn_1$ precipitate had a notable effect on the wear characteristics of Mg alloy. Asl et al [130] studied the addition of RE elements on the wear characteristics of AZ81 alloy. The presence of needle-shaped $Al_{11}RE_3$ particles enhanced the wear behaviour of AZ81; particularly at higher loads due to the high resistance offered by $Al_{11}RE_3$.

2.4 Literature Gap

After an exhaustive literature study, following gaps were identified:

- Literature study reveals that limited studies are available on the FSP of magnesium alloys in comparison to aluminum alloys. Further, the FSP approach employed on Mg alloys is mostly confined to commercially or wrought alloy system such as Mg-Al-Zn (AZ series), Mg-Zn-Zr (ZK series), Mg-Al-Mn (AM series) & Rare Earth (RE). Inadequate amount of work has been carried out on cast magnesium alloys.
- Majority of the investigations related to FSP of Mg alloys are based on grain refinement, surface composite fabrication, and superplasticity. Limited studies are available on the enhancement of properties due to FSP aided precipitates refinement/modification.
- Investigation regarding optimization of process parameters to yield better mechanical and wear properties is not enough in the case of magnesium alloys.
- Products obtained after FSP are not explored in past for the bearing applications.

2.5 Research Objectives

The presented work is based on the following research objectives:

1. Microstructural and mechanical characterization of as-cast and FSPed Magnesium alloy.
2. Tribological studies of as-cast and FSPed Magnesium alloy
3. Optimization of FSP parameters to yield enhanced mechanical and tribological properties.
4. Fabrication of sector shape pad as per the best result.

CHAPTER 3

METHODOLOGY AND EXPERIMENTATION

Chapter 3 discusses the methodology and experimentation details for attaining the objectives of the thesis. This chapter is organized into three parts as per the execution of experimental and optimisation work. In the first part, surface modification of AS21A magnesium alloy was performed using Friction Stir Welding (FSW) setup. The hybrid approach of Taguchi − Grey Relational Analysis (GRA) − Principal Component Analysis (PCA) was utilized for achieving the optimum set of FSP parameters. A detailed explanation of the optimization strategy is also included in this part. In the second part, cast and FSPed samples of AS21A alloy were characterized mechanically and tribologically through various types of equipment, primarily Optical Microscope, Scanning Electron Microscope, Energy Dispersive Spectroscopy (EDS), X-ray Diffractometer, Universal Testing Machine, Microhardness and Pin on-Disc Tribometer. In the third part, a sector shape pad of thrust bearing was prepared from the investigated material through the multi-pass (50 % overlap) strategy of FSP.

3.1 Work material

The present investigation utilized AS21A commercial alloy of Magnesium–Aluminium–Silicon (Mg–Al-Si) group in the form of a plate having a 200×80×10 mm dimension. The Gravity Die Casting route prepared AS21A alloy was procured from Venuka Engg, Hyderabad, India. The AS21A chemical composition characterized as per ASTM B94- 2013 standards is shown in Table 3.1. The Inductively Coupled Plasma−Optical Emission Spectroscopy (ICP−OES) spectrometer, Model: Spectro Max, Made in Germany facility at NTL, Delhi was used for spectroscopy.

Table 3.1 Chemical composition of cast AS21A alloy

Alloy	Al	Si	Mn	Zn	Cu	Fe	Ni	Mg
Percentage	2.12	1.04	0.221	0.058	0.002	0.003	<0.001	Rest

After procurement, as-received casting plates were firstly machined on conventional machines, importantly Lathe and milling, to make them suitable for research work. Figure 3.1 depicts the as-cast and machined surface of the procured alloy.

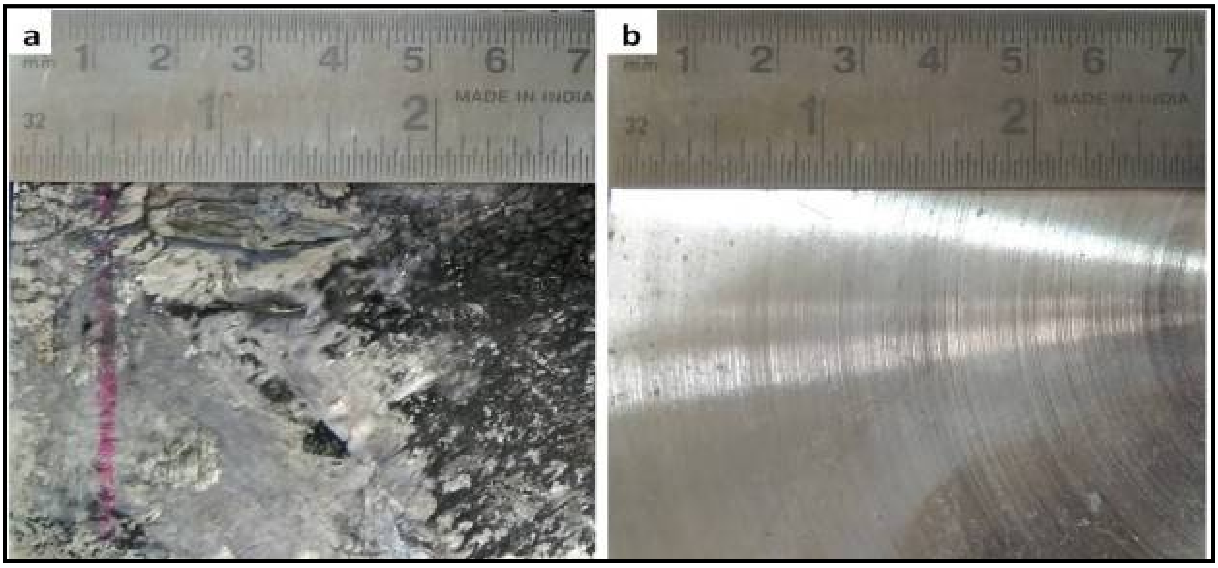

Figure 3.1 Surface of AS21A alloy casting plate (a) as received; (b) machined

3.2 Experimental Technique

The Friction Stir Processing (FSP) technique was utilised in achieving the surface modification of the parent material. In this technique, a non−consumable spinning tool is introduced into the material surface which creates rigorous plastic deformation due to the mixed influence of tool stirring and frictional heat. Tool pin is responsible for mechanical stirring while the frictional heat is generated by the axial load aided penetration of the tool shoulder. After the attainment of sufficient amount of heat and deformation, the tool pin is in a capacity to direct the material from advancing to retreating side of the plate. Finally, tool is traversed longitudinally to get the desired modified surface. The schematic sketch of the FSP principle is shown in Figure 3.2.

3.2.1 FSW equipment

An indigenously developed friction stir welding set up (R V machine tools, FSW-4T-HYD) shown in Figure 3.3(a) was the main research equipment for undertaking the FSP technique. Figure 3.3(b) depicts the surface appearance of a random sample when treated with FSP. Machine specifications are as follows:

- Power – 11 KW
- Spindle RPM – Variable up to 3000
- Load capacity – 25 KN
- Clamps – hydraulically actuated
- Backing plate groove – 200 mm × 80 mm

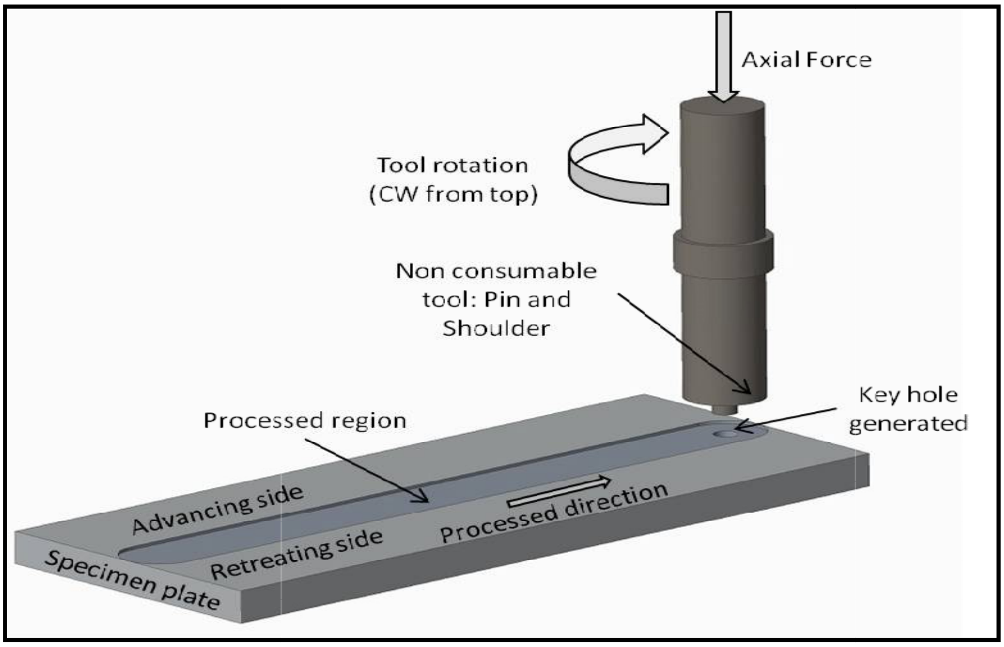

Figure 3.2 Schematic of Friction Stir Processing (FSP) principle

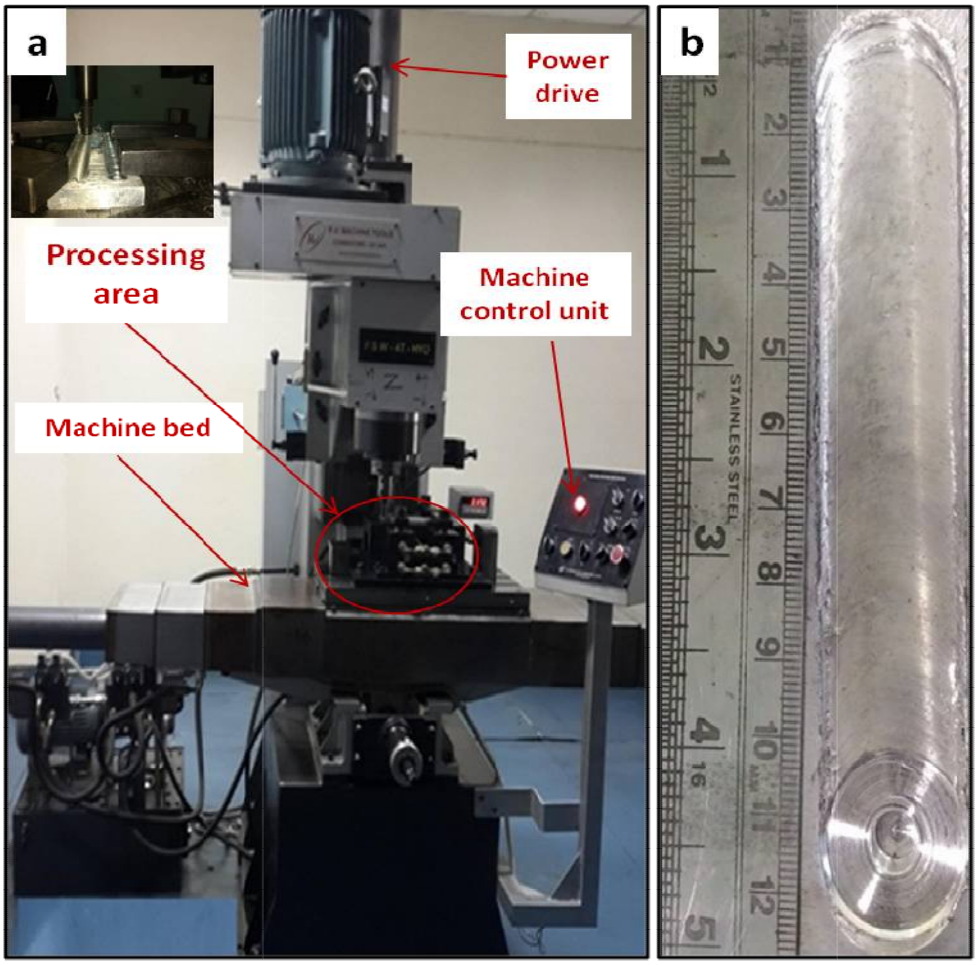

Figure 3.3 (a) FSW set up (R V machine tools, FSW-4T-HYD), (b) Surface appearance of the FSPed specimen

3.2.2 FSP Tool

The tool is the heart of FSW equipment since it generates the required frictional heat which is utilized in the formation of SZ. The tool constitutes shoulder and pin. FSP tool employed along with its dimensional features is shown in Figure 3.4. Following are the characteristics of the tool employed during FSP operation:

- Shoulder diameter of 16, 20 and 24 mm.
- H-13 tool steel material heat treated to 55 HRC
- Threaded cylindrical probe of 1 mm pitch.
- Probe length of 5 mm.
- Probe diameter of 6 mm.

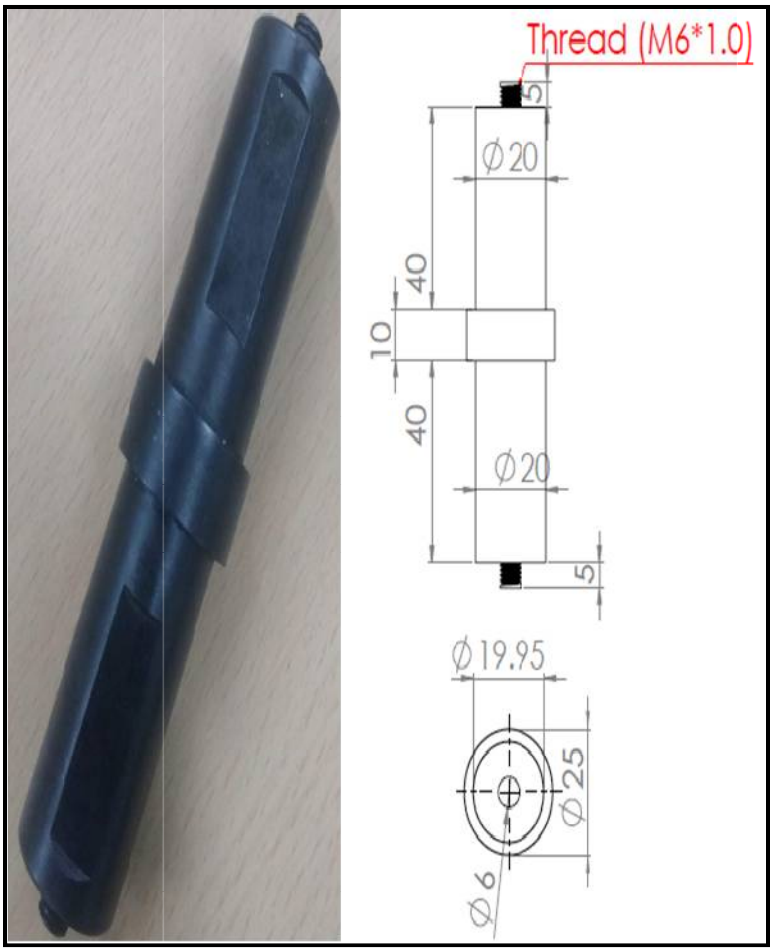

Figure 3.4 FSP tool with dimensional attributes

3.2.3 Process parameters

FSP technique involves a variety of parameters that can affect the product characteristics in different ways. Therefore, optimisation of parameters is an essential task in FSP. The significant variables which extensively affect the characteristics of the material are tool geometry, tool rpm and tool travel or traverse speed. Rotational and linear speeds of the FSP tool corresponds to the amount of heat generation in the SZ thus controlling the material flow and microstructure features which directly affects the mechanical and wear behaviour of the material [53]. The formation of SZ is also affected by the parameters like tool tilt angle and penetration depth but not much of significance therefore usually kept fixed. Further, FSP tool geometry consisting of shoulder diameter, pin shape, pin size and pin features promotes the heat generation, material flow and microstructural advancement in the material. The smaller shoulder diameter corresponds to the formation of defects whereas the larger shoulder diameter corresponds to enhanced material flow and high heat generation [131]. Optimum shoulder diameter should be selected during FSP since excessive high and low diameter exhibits lower strength due to the annealing and the inadequate heat generation phenomena respectively [58].

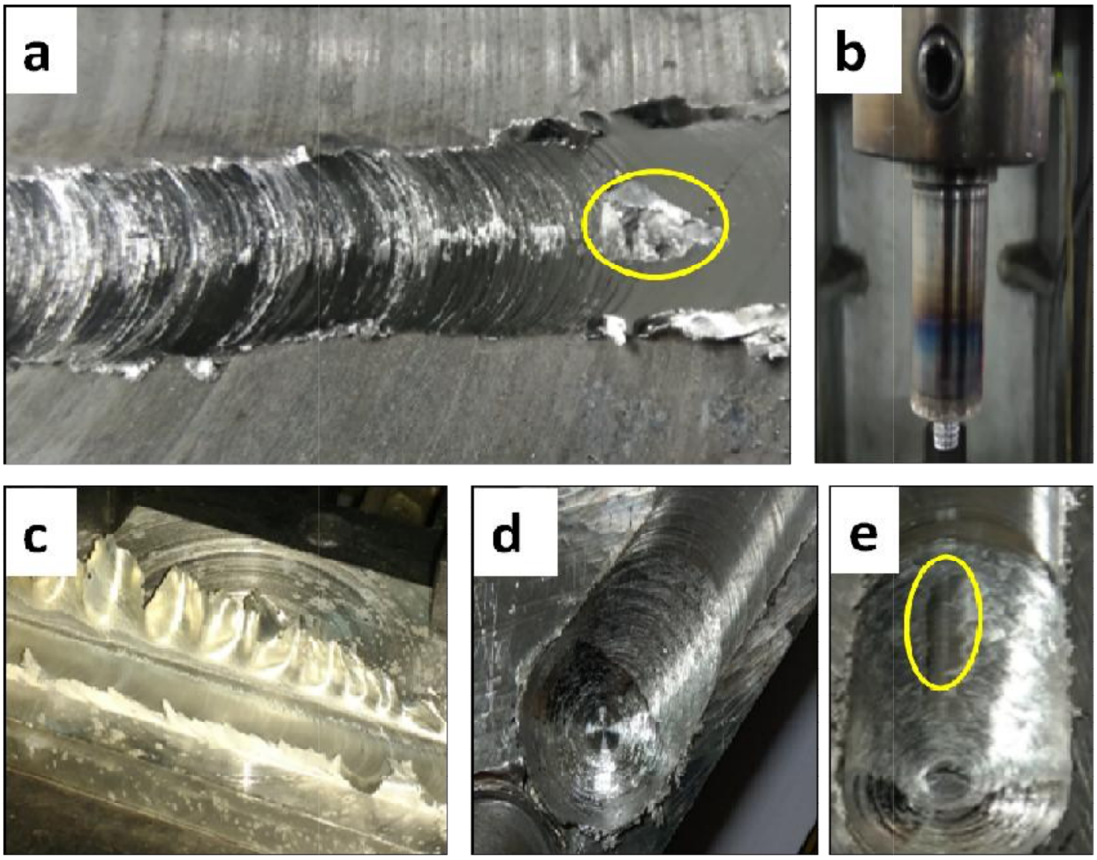

Figure 3.5 Defects encountered during preliminary experiments

Pilot experiments were carried out on AS21A magnesium alloy to identify the working range of FSP process parameters. Some of the major snags were encountered during the preliminary experiments as shown in Figure 3.5. Defects such as longitudinal cracks and tunnelling cavities (Figure 3.5a,e) were formed in the processing zone due to the insufficient tool plunge depth. Excessive flash (Figure 3.5d) was also observed due to high shoulder diameter and high heat input. In addition to this, galling and tearing of the metal (Figure 3.5c) on the top surface were also observed which can be attributed to the sticking of metal to the pin tool (Figure 3.5b) and excessive heat generation during processing.

Therefore, based on literature and pilot tests, following input parameters were selected which can influence the properties of AS21A material to a greater extent:

1. Rotational speed (RS)
2. Travel speed (TS)
3. Shoulder Diameter (D)

In addition to this, two pass FSP with 100% overlap and the same forward direction was employed to accelerate the material mixing and breakage of the hard and brittle eutectic networks present in the AS21A matrix. Also, the threaded pin profile of the FSP tool was selected to enhance the material flow and mixing from top to bottom. The values and levels corresponding to FSP input parameters are listed in Table 3.2. Figure 3.6 exhibits the processing zone and the tools employed in the present investigation.

Table 3.2 FSP input parameters and their levels

Designation	Variable Parameters	Level 1	Level 2	Level 3
RS	Rotational Speed (rpm)	400	800	1200
TS	Travel Speed (mm/min)	20	50	80
D	Shoulder Diameter (mm)	16	20	24
	Fixed parameters			
	Pin Diameter (d)		6 mm	
	Pin Length		5 mm	
	Pin Profile		Threaded Cylindrical	
	Plunge Depth		0.1-0.2 mm	
	FSP passes		2 with 100 % overlap	

3.2.4 Selection of orthogonal array

The 1st stage in identification of optimal FSP conditions is the selection of an orthogonal array also called a design matrix. The rotational speed, travel speed and shoulder diameter of FSP tool are the selected input parameters and 3 levels are corresponding to them, thus yielding 3 Degrees of Freedom (DOF). The DOF corresponds to the number of comparisons required among process parameters in order to optimise them. It is required that the total

DOF of the input parameters should be less than the DOF for a whole system. In this step, the effects of the main factor are taken into account not their interactions. DOF corresponding to each factor is determined as 3−1= 2 where 3 are number of levels, and consequently, the total DOF will be 6 (3 × 2). Generally, the total DOF of the factors should be less than the DOF of the OA. Since the DOF corresponding to L9 OA is 8, thus it is found to be appropriate for the present work. Therefore, in the present study, experiments were performed as per the L9 design matrix presented in Table 3.3, which is in accordance with the Taguchi design.

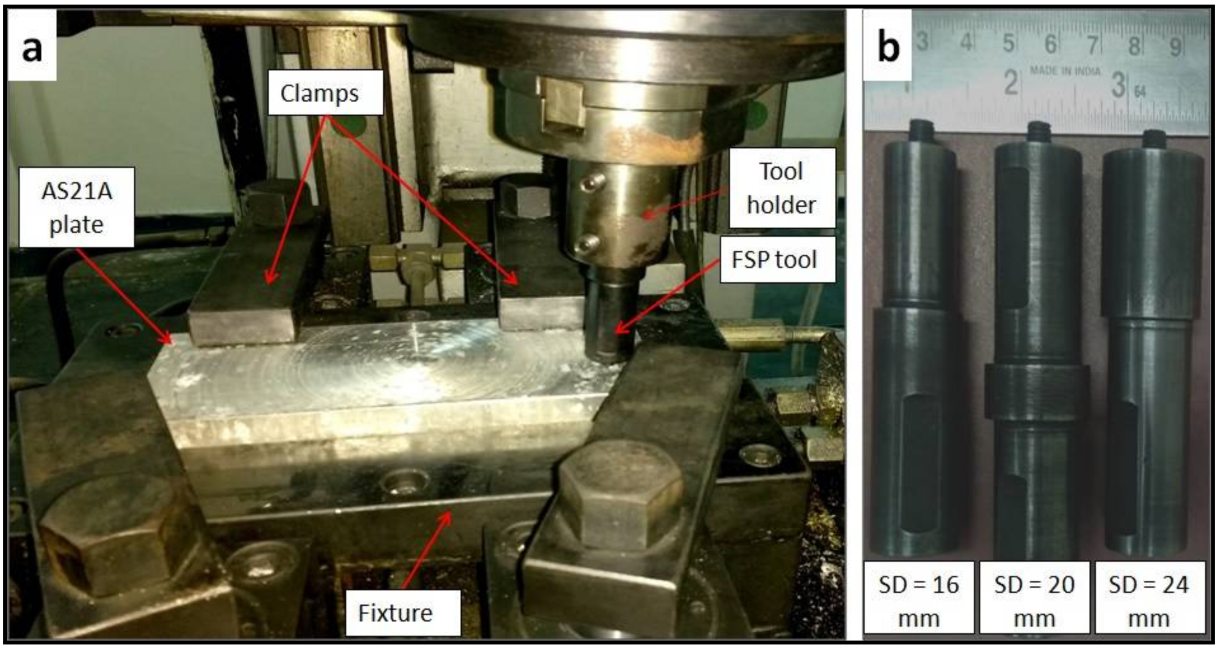

Figure 3.6 (a) Processing zone in FSW machine; (b) FSP tools

Table 3.3 Experimental design as per L9 orthogonal array and their results

Exp. No.	Input factors			Performance attributes		
	RS	TS	D	UTS (MPa)	ε (%)	HV
1	400	20	16	88.4	5.32	62.2
2	400	50	20	91.8	6.72	64.1
3	400	80	24	89.9	5.43	65.5
4	800	20	20	89.4	10.1	64.7
5	800	50	24	90.2	9.31	66.2
6	800	80	16	89.2	9.75	65.5
7	1200	20	24	90.3	7.95	64.3
8	1200	50	16	91.5	5.58	63.6
9	1200	80	20	91.1	7.12	64.9

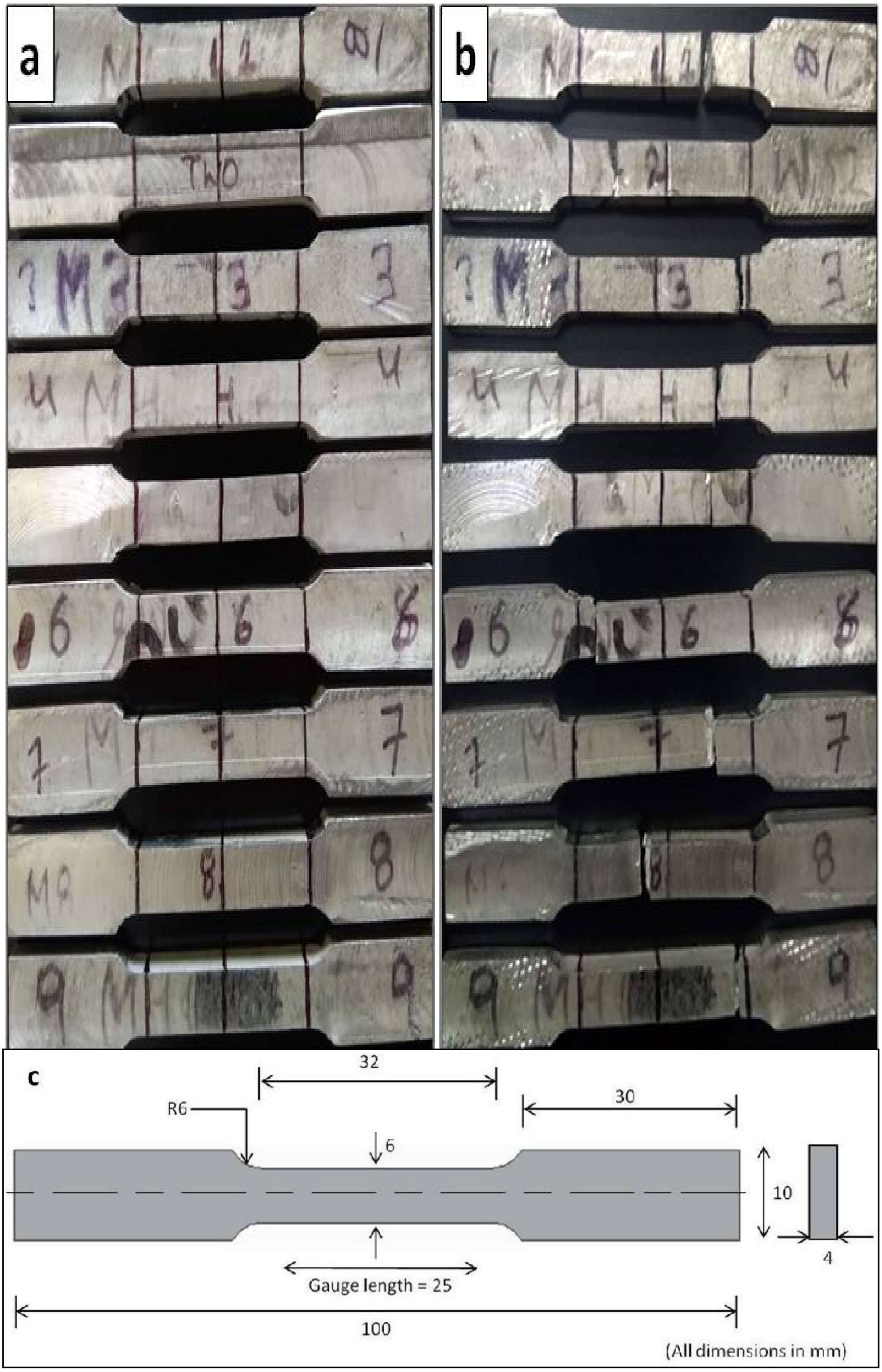

Figure 3.7 Tensile specimens (a) before fracture; (b) after fracture and (c) prepared as per ASTM B557M-06

3.2.5 Experimental results

The Ultimate Tensile Strength (UTS) in MPa, Ductility (ε) in % elongation and Microhardness in HV were measured as performance attributes of the present study. Longitudinal tensile test specimens were prepared according to ASTM B557M-06 specification as shown in Figure 3.7c, and testing was carried out on a universal testing machine set up at a crosshead mean speed of 2.5 mm/min. Figures 3.7 depict the fracture location of tensile test specimens. The microhardness analysis was carried out using a microhardness setup attached with Vickers diamond pyramidal indenter (136°) at a load of 100 gram with a dwell time of 10 seconds. The experimental results are presented in Table 3.3.

3.3 Research methodologies

The Taguchi-GRA-PCA hybrid approach was effectively utilized in the current investigation for achieving the optimal combination of FSP parameters. The following section discusses the optimisation strategy in detail.

3.3.1 Taguchi method

Genichi Taguchi remembered as the "father" of quality engineering [132] analyzed the engineering problems with the statistical approach. Taguchi technique attempts to optimize a product or process design and is accomplished in three steps of design i.e. system, parameter and tolerance. In recent years, the Taguchi approach is established as a valuable tool in research and development activities. Taguchi approach utilises Orthogonal Arrays (OAs) from the design of experiment theory to analyse a more no. of variables with a less no. of experiments. Taguchi technique was formulated for the process optimisation and determining optimal levels of input parameters for obtaining the desired process responses [133]. It is one of the time-efficient and economical optimisation techniques. In this method, the experimental readings of the process responses are converted to a ratio; called a signal to noise (S/N) ratio. S/N ratio represents the ratio of signal i.e. mean to noise i.e. standard deviation. S/N ratio signifies the degree of robustness used to recognize control factors that decrease variability in a process or product by diminishing the influence of uncontrollable factors. The process attribute that is to be minimized and minimized is referred to as 'Lower the better' and 'Higher the better' respectively. In Taguchi, deviation of process attribute from the mean value is measured using the S/N ratio [134, 135].

S/N ratio with the larger-the-better attribute can be evaluated from the following expression:

$$\text{S/N ratio } (\eta) = -10\log_{10}\frac{1}{n}\sum_{i=1}^{n}\frac{1}{y_i^2} \quad (3.1)$$

S/N ratio with the lower-the-better attribute can be evaluated from the following expression:

$$\text{S/N ratio } (\eta) = -10\log_{10}\frac{1}{n}\sum_{i=1}^{n}y_i^2 \quad (3.2)$$

where n is the total no. of experiments and y_i represents the experimental values of the i^{th} experiment.

The S/N ratio for each attribute can be calculated separately despite the type of performance characteristics. Generally, a higher S/N ratio value denotes the better performance characteristics.

3.3.2 Grey Relational Analysis (GRA)

The Grey theory, formulated by Deng in 1982, is mainly used to analyze a process that involves both known and unknown factors. GRA is similar to the black-box concept that contains both known and unknown factors. to solve the problems having multiple responses [136]. Unlike Taguchi, GRA optimises a problem having multiple responses by converting all responses to a single output, known as Grey Relational Grade (GRG). GRA involves data pre-processing (data normalization), GRC calculation using deviation sequence and GRG calculation [137-140]. Following steps are involved in GRA:

1. The first step in GRA analysis is the normalization or pre-processing of experimental data, referred to as a grey relational generation. In this step, the experimental data (S/N ratio in the present study) is converted to a value in the range from 0 to 1. The experimental data is called a reference sequence while normalized data is called a comparable sequence. The objective should be well defined in advance for this step. Three different quality characteristics namely the larger the better, smaller the better and nominal the better are used. If maximization of the original sequence is the objective, the "larger the better" notion is applied to normalize reference sequence and normalization is calculated according to Eqn 3.3 [137-140].

$$x_i^c(k) = \frac{x_i^r(k) - min\, x_i^r(k)}{max\, x_i^r(k) - min\, x_i^r(k)} \quad (3.3)$$

If the minimization of original sequence is the objective, the “smaller the better” notion is applied to normalize reference sequence and normalization is calculated according to Eqn 3.4 [137-140].

$$x_i^c(k) = \frac{max\, x_i^r(k) - x_i^r(k)}{max\, x_i^r(k) - min\, x_i^r(k)} \tag{3.4}$$

where, $x_i^r(k)$ denotes reference sequence while $x_i^c(k)$ denotes the sequence obtained after normalization i.e., comparability sequence, $max\, x_i^r(k)$ and $min\, x_i^r(k)$ are the highest and least value in reference sequence respectively, $i = 1,2,3, \ldots\ldots, m \; and \; k = 1,2,3, \ldots\ldots, n$; m is the no. of experimental runs and n is the no. of responses. In the present case, $m = 9$ and $n = 3$.

2. GRC calculation: the GRC is calculated to ascertain the correlation between comparability$[x_i^c(k)]$ and reference $[x_i^r(k)]$ sequence. GRC is calculated from the following expression:

$$\Gamma[x_i^c(k), x_i^r(k)] = \frac{\triangle_{min}(k) + \xi\, \triangle_{max}(k)}{\triangle_{rc}(k) + \xi\, \triangle_{max}(k)} \tag{3.5}$$

where, $\triangle_{rc}(k)$ known as deviation sequence is the absolute value of the difference between $x_i^c(k)$ and $x_i^r(k)$ given by:

$$\triangle_{rc}(k) = ||x_i^c(k) - x_i^r(k)|| \tag{3.6}$$

$\xi \in [0,1]$ known as distinguishing coefficient. In the present study, ξ is set at 0.5.

$\triangle_{max} = max_{\forall j \in i} max_{\forall j \in k} ||x_i^c(k) - x_i^r(k)||$ is the largest value of $\triangle_{rc}(k)$ (3.7)

$\triangle_{min} = min_{\forall j \in i} min_{\forall j \in k} ||x_i^c(k) - x_i^r(k)||$ is the smallest value of $\triangle_{rc}(k)$ (3.8)

3. GRG calculation: The last step in GRA is to determine the grey relational grade. GRG is weighted sum of GRC calculated values which is determined using the following expression:

$$\Psi[x_i^c, x_i^r] = \sum_{k=1}^{n} \delta_k\, \Gamma[x_i^c(k), x_i^r(k)] \tag{3.9}$$

where δ_k represents the fraction values of k^{th} response, and $\sum_{k=1}^{n} \delta_k = 1$. In this paper, the respective fraction (δ_k) values of responses were obtained from PCA.

GRG $\Psi[x_i^c, x_i^r]$ signifies the intensity of the correlation between the comparability series and the reference series. Value of GRG is 1 for the ideal condition i.e. when the two sequences are alike. The GRG also represents the degree of influence the reference series could be affected by the comparability series. Thus, if a particular comparability sequence is more significant than rest of the comparability sequences, then that particular comparability sequence will have a higher value of GRG compared to all other GRGs. Grey analysis is the determination of absolute value which is obtained by the difference between sequence values, and it could be utilized to assess the approximate relationship between sequences [141].

3.3.3 Principal Component Analysis (PCA)

PCA tool was introduced by Pearson and Hotelling to describe the construction of variance and covariance of multiple quality attributes by integrating them linearly [140, 142]. The step by step procedure of PCA is explained as follows:

1. The multiple quality characteristics are initially expressed in the form of a matrix given by:

$$M_{ij} \ where \ i = 1,2,3, \ldots\ldots, n \ and \ j = 1,2,3, \ldots\ldots, q$$

$$M_{ij} = \begin{bmatrix} m_1(1) & m_1(2) & \ldots\ldots & m_1(q) \\ m_2(1) & m_2(2) & \ldots\ldots & m_2(q) \\ . & . & \ldots\ldots & . \\ . & . & \ldots\ldots & . \\ . & . & \ldots\ldots & . \\ m_n(1) & m_n(2) & \ldots\ldots & m_n(q) \end{bmatrix} \quad (3.10)$$

   where n is no. of experimental runs and q is no. of performance characteristics. In the present study, n = 9, q = 3 and m denote the GRC value corresponding to each quality characteristic.

2. Calculation of correlation coefficient matrix by the following equation:

$$C_{jl} = \left(\frac{covar(M_i(j), M_i(l))}{\sigma_{Mi}(j) \times \sigma_{Mi}(l)} \right); j \ and \ l = 1,2,3, \ldots\ldots, n \quad (3.11)$$

   where $covar(M_i(j), M_i(l)$ are the covariance of sequences $M_i(j)$ and $M_i(l)$ while $\sigma_{Mi}(j)$ and $\sigma_{Mi}(l)$ represents their standard deviation.

3. Determination of Eigen values and eigenvectors using the following expression:

$$(C - \mu_k I_m)E_{ik} = 0 \quad (3.12)$$

   where μ_k represents the Eigen values, $\sum_{k=1}^{n} \mu_k = n, k = 1,2,3, \ldots\ldots, n$; $E_{ik} = [a_{k1} a_{k2} a_{k3} \ldots\ldots a_{km}]^T$ represents Eigen vectors corresponding to the Eigen value μ_k.

4. Computation of uncorrelated principal components using the following expression:

$$Y_{mk} = \sum_{i=1}^{n} x_m(i) \times E_{ik} \quad (3.13)$$

   The above equation will provide Y_{m1} and Y_{m2} as the first and second principal component values respectively and so on. The components are ordered in descending order of variance, and consequently Y_{m1} reports for largest variance in the data.

3.4 Specimens preparation

Conventional methods are not appropriate for cutting the specimens from FSP treated regions as it is difficult to achieve accuracy in these techniques. Therefore, CNC wire cut is the most suitable technique for obtaining the specimens from FSPed regions. In this, specimens of requisite dimensions were sliced in the traverse direction from the processed region for examining the key characteristics. The flowchart shown in Figure 3.8 exhibits the step by step procedure of specimen preparation.

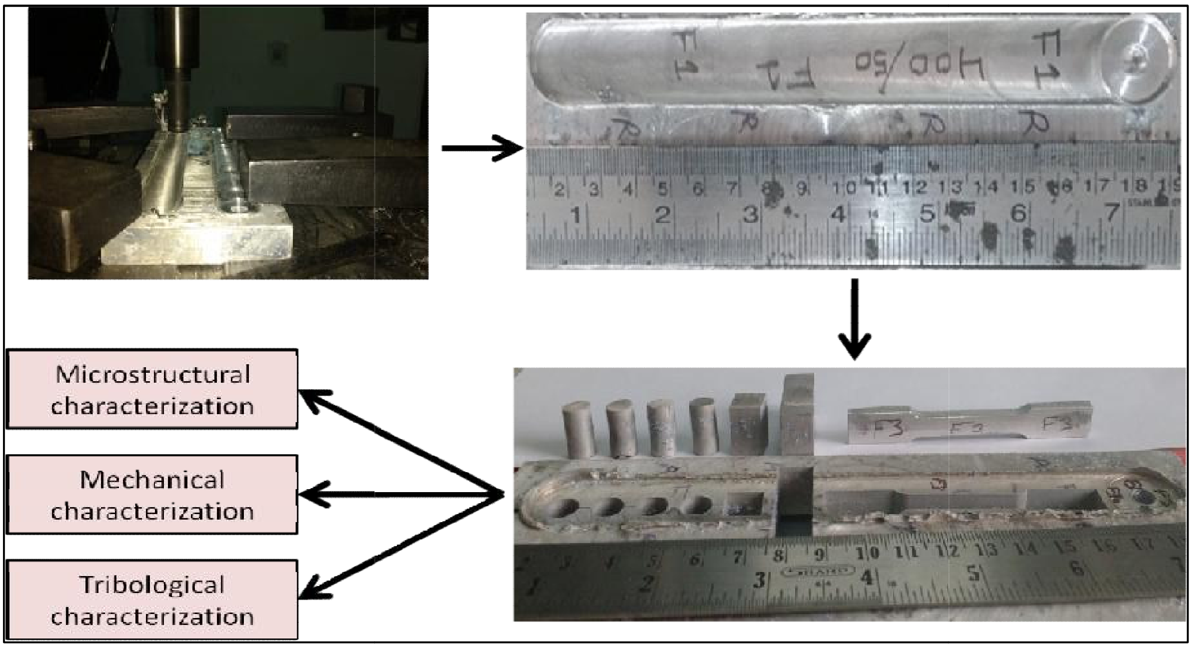

Figure 3.8 Flowchart showing the steps for specimen preparation

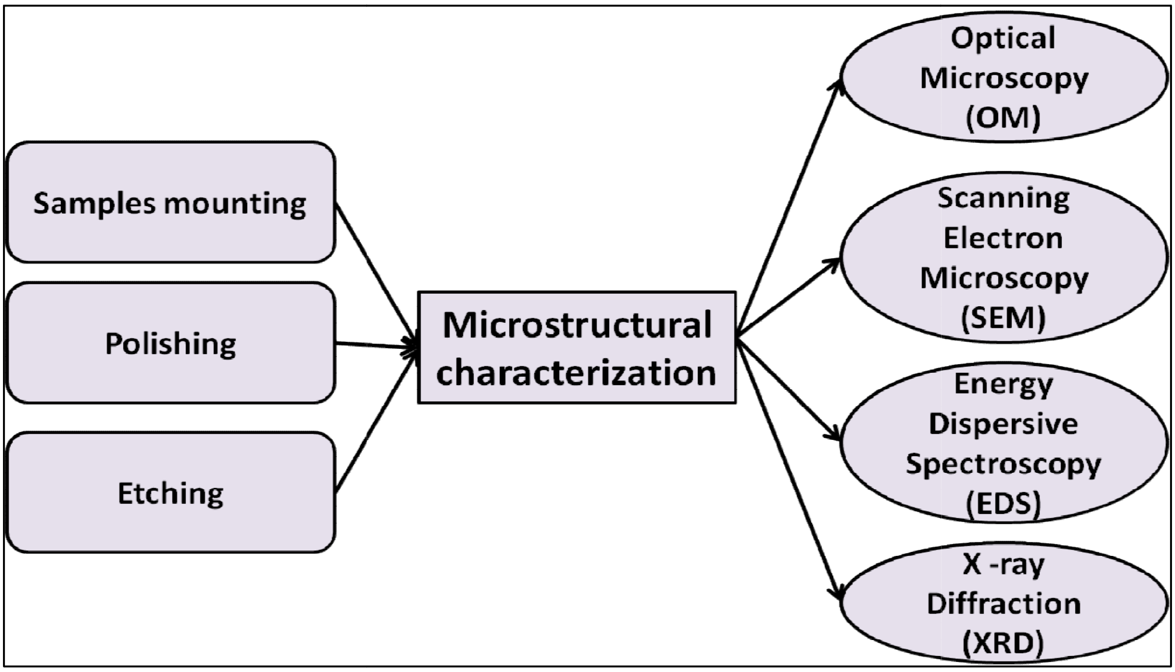

Figure 3.9: Steps followed for microstructural characterization

3.5 Microstructural Observation

The microstructure of the material is an important part of the characterization since the behaviour of the material will be decided by its attribute. The flowchart shown in Figure 3.9 depicts the whole procedure of microstructure characterization from prerequisites of the specimen to the characterization using conventional and advanced machinery. In the present research work, typical machinery used for characterization includes Optical Microscopy (OM), Scanning Electron Microscopy (SEM), Energy Dispersive Spectroscopy (EDS) and X-ray Diffraction (XRD).

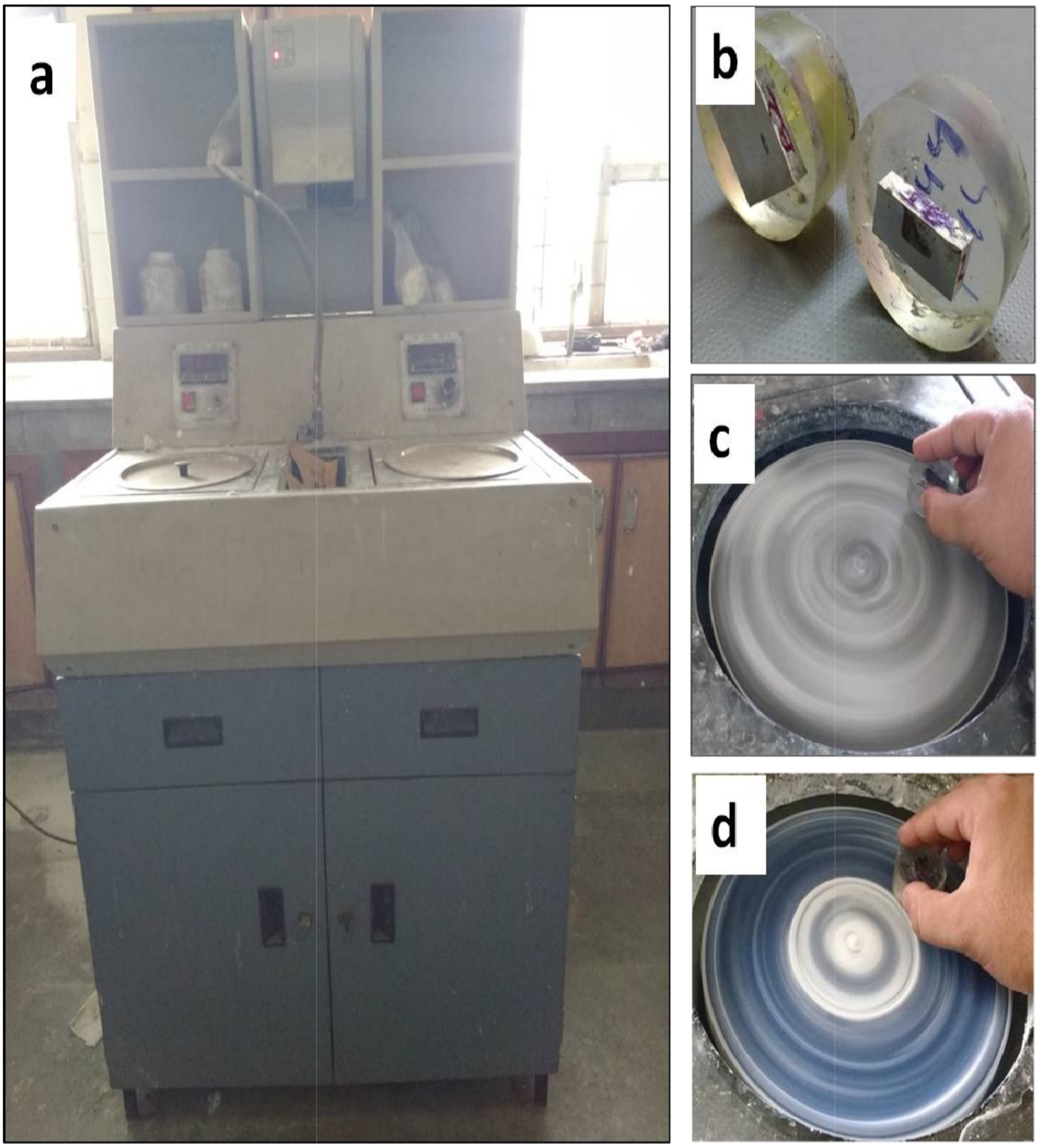

Figure 3.10 (a) Polishing machine, (b) Cold mounted samples, (c,d) Dry and wet polishing method

3.5.1 Samples mounting

Smooth and appropriate polishing of specimens is desired for superior characterisation studies. Since samples are small in size and can cause poor polishing; therefore samples are mounted for proper gripping. Magnesium alloys are very soft materials and have a low melting point compared to other non-ferrous alloys; therefore hot mounting of magnesium specimens is not appropriate since it will result in an appreciable amount of microstructural changes. In the present work, AS21A specimens were mounted using a combination of resin (90%) and hardener (10 %), commonly known as the cold mounting technique, as shown in Figure 3.10 (b).

3.5.2 Polishing

Polishing starts with the dry polishing of mounted samples through various grades of an emery paper. Samples were progressively rubbed against the emery from coarser one (100 grade) to finer one (2000 grade) grit. Further polishing of samples was performed on a polishing machine having two rotating discs as shown in Figure 3.10 (a). In this machine, initially wet polishing was performed by rubbing the specimens against the fine grade emery which is fastened to the rotating disc as shown in Figure 3.10 (c). Afterwards, wet polishing was performed against the velvet type cloth along with the alumina powder (I, II and III grade) as depicted in Figure 3.10 (d). During polishing, samples were dried intermittently using the dryer available on the machine. Since the present study is based on magnesium alloy having soft attributes; therefore precaution was taken during polishing to avoid scratch marks and unnecessary surface contamination. In the end, samples were rinsed in ethanol as the water was not enough to eliminate surface contaminants.

3.5.3 Etching

Finally, samples were etched in the chemical solution for 5-10 s to reveal the grain structure. The acetic picral etchant solution comprising of ethanol (100 ml), acetic acid (5 ml), picric acid (6 gms) and water (10 ml) was used. After chemical etching, a residual layer retained on the sample surface was removed by ethanol.

3.5.4 Optical Microscopy (OM)

The microstructural features of the specimens such as grain structure, Mg_2Si morphology etc. were analyzed using an Olympus Compact Inverted Metallurgical Optical Microscope (OM), model GX 41 having attachment of 10 x, 20 x, 50 x and 100 x objective lenses and a dedicated computer installed with image analysis software. The basic principle of the microscope is that it utilises an objective lens for creating the magnified image of the specimen and further magnification is achieved using an eyepiece so that the user can easily observe it with the naked eye. The OM equipment and its working principle are depicted in Figure 3.11. The average grain size of microstructure was estimated using the linear intercept concept of ImageJ software. Also, the scale bar on the microstructure was incorporated using ImageJ software.

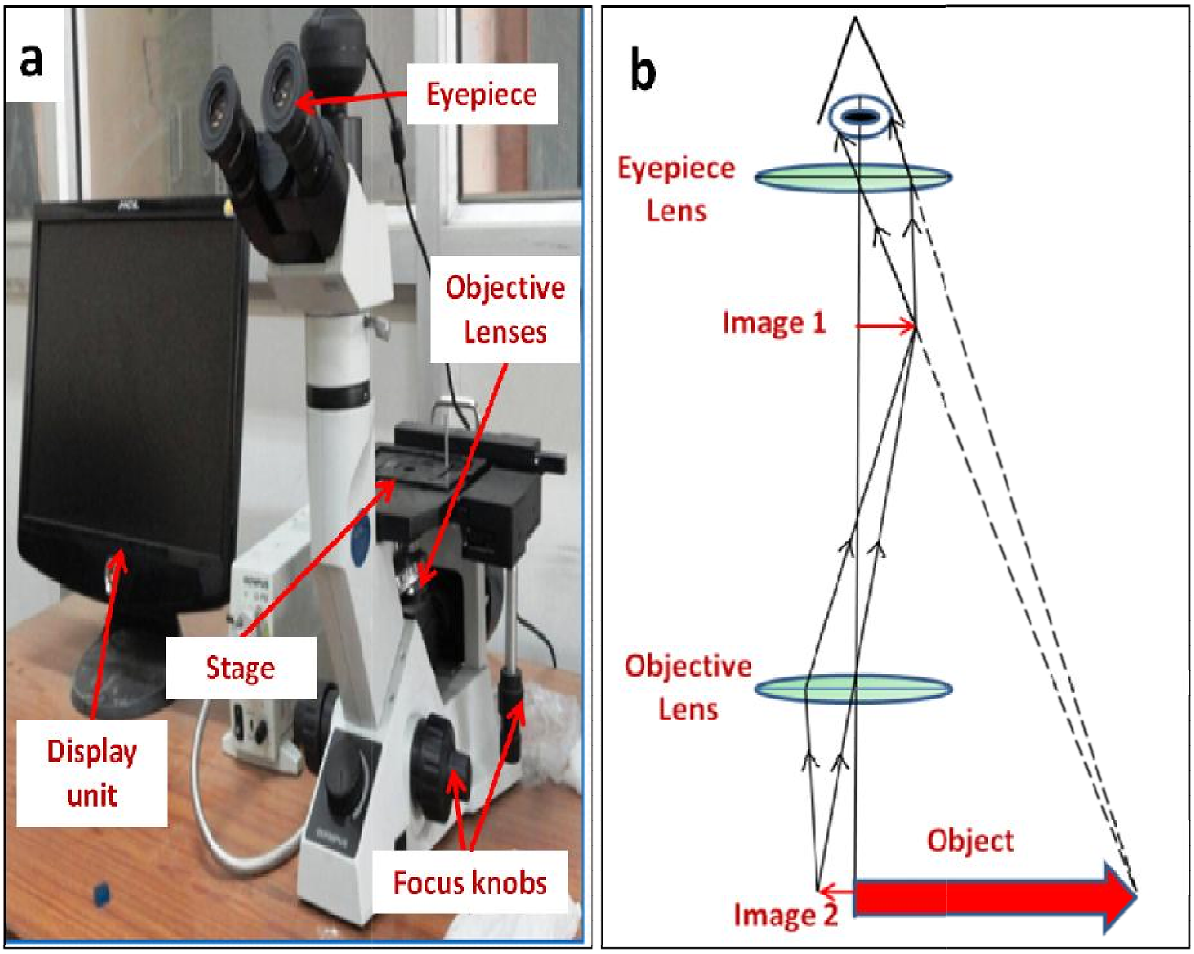

Figure 3.11 Optical Microscope (a) setup (Olympus, Model: GX 41); (b) principle

3.5.5 Digital microscope

The Celestron Handheld Digital Microscope, model 45308-DS 5 MP, shown in Figure 3.12 (a) was utilised for taking the macrographs of the FSP treated specimens. These images were useful for locating the FSP impression in the transverse section i.e. section vertical to the processing direction. One can ensure the formation of the defect-free stirred zone in the specimen through macrographs. The sample image of the FSP impression is depicted in

Figure 3.12 (b). A digital microscope is equipped with a digital camera permitting examination of a sample through a computer.

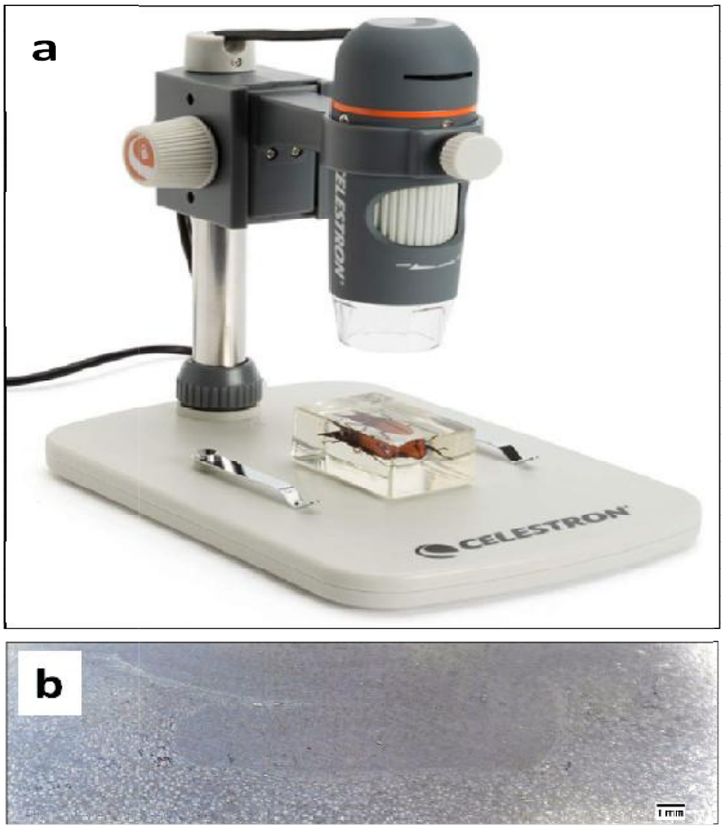

Figure 3.12 Handheld Digital microscope (Celestron, Model: 45308-DS 5 MP), (b) FSP impression captured

3.5.6 Scanning Electron Microscope (SEM)

The scanning electron microscope analysis provides the microstructural features, grain and grain boundary information and second phase compounds in the solid-state materials. In SEM, images of the specimens are generated by scanning the specimen surface with the highly focussed electron beam. The electrons are discharged from the electron gun. The process involves the interaction of electrons with atoms in the specimen, thus generating signals containing reports of the specimen composition and topography. The electron beam scans the sample in a raster pattern, and beam location is merged with the intensity of the perceived signal to generate the desired picture. The basic components of SEM include the source of electrons i.e. electron gun, lenses, scanning coil, detectors to store signals, sample stage and display devices. The electron column must be under vacuum to protect it from contamination, noise and vibrations. The vacuum will also help in acquiring the high-resolution image since foreign atoms and molecules can interfere with the electron beam in the absence of the vacuum. The schematic illustration of the SEM principle is depicted in Figure 3.13(a).

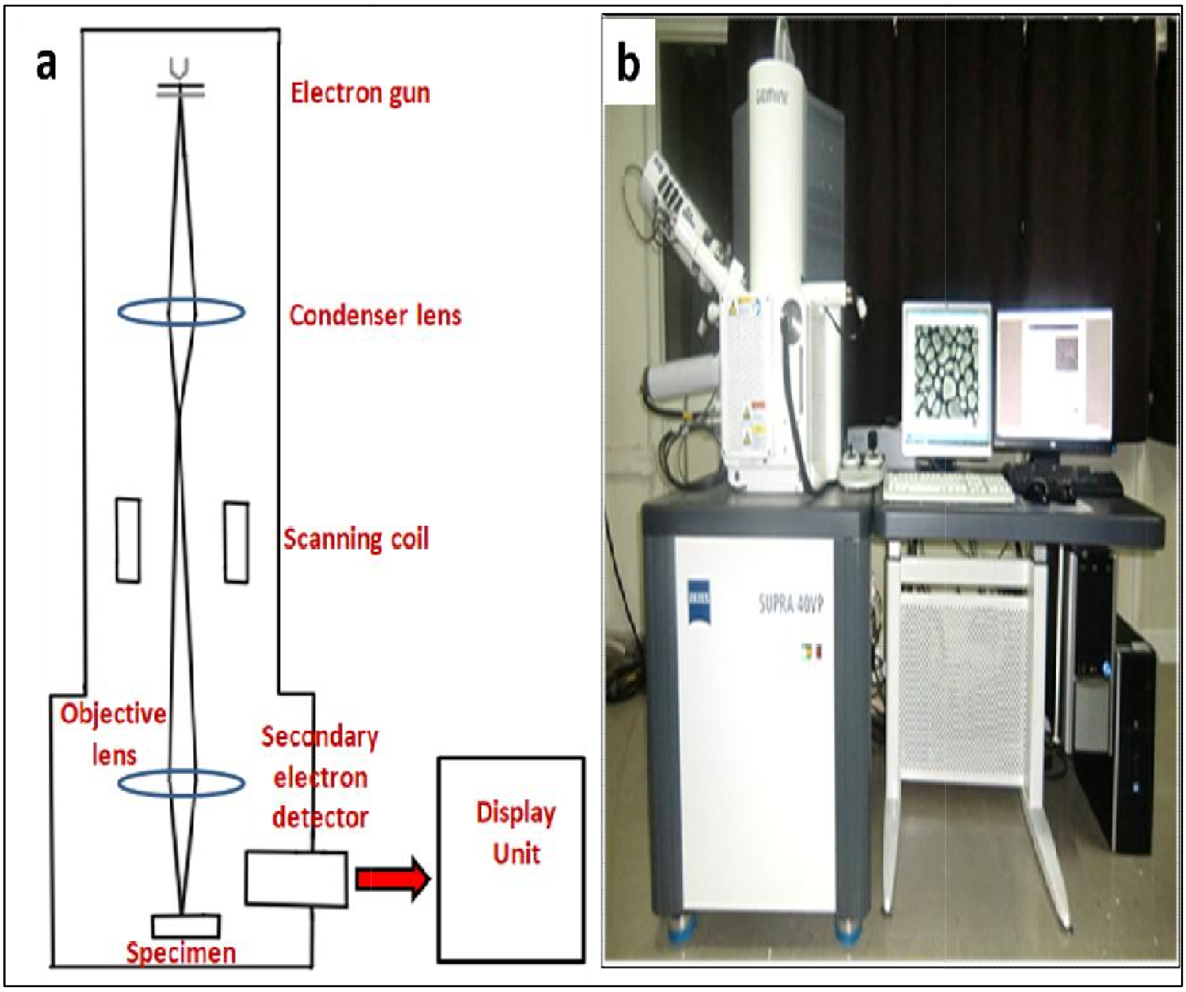

Figure 3.13 (a) Principle of SEM; (b) FESEM set up (Zeiss, Germany; Model: SUPRA 40VP) for microstructural analysis

In the present study, Field Emission Scanning Electron Microscope (FESEM), Zeiss, Germany; Model: SUPRA 40VP shown in Figure 3.13 (b), was employed for the analysis of microstructure and elemental analysis of Mg_2Si intermetallic in AS21A alloy. Moreover, fractured surfaces obtained from the tensile test and worn out surfaces obtained from the wear test were studied using FESEM for better analysis. In FESEM, a Field Emission gun is used for producing fine electron beam thus producing high resolution images.

3.5.7 Energy Dispersive Spectroscopy (EDS)

Energy-dispersive X-ray spectroscopy also referred to as Energy Dispersive X-ray Analysis (EDXA or EDAX) is an analytical method used for identifying the elemental composition of specimen. EDS analysis is an integral part of SEM and cannot work on its own. During EDS analysis, a solid sample is bombarded with a focussed beam of electron which results in the emission of X-rays with a unique amount of energy. By computing the amount of energy in X-rays, the identity of the particular atom can be established. The output of EDS is obtained in the form of a spectrum exhibiting peaks of various elements constituting the sample. In the present work, elemental characterization of microstructural and wear samples was achieved through it.

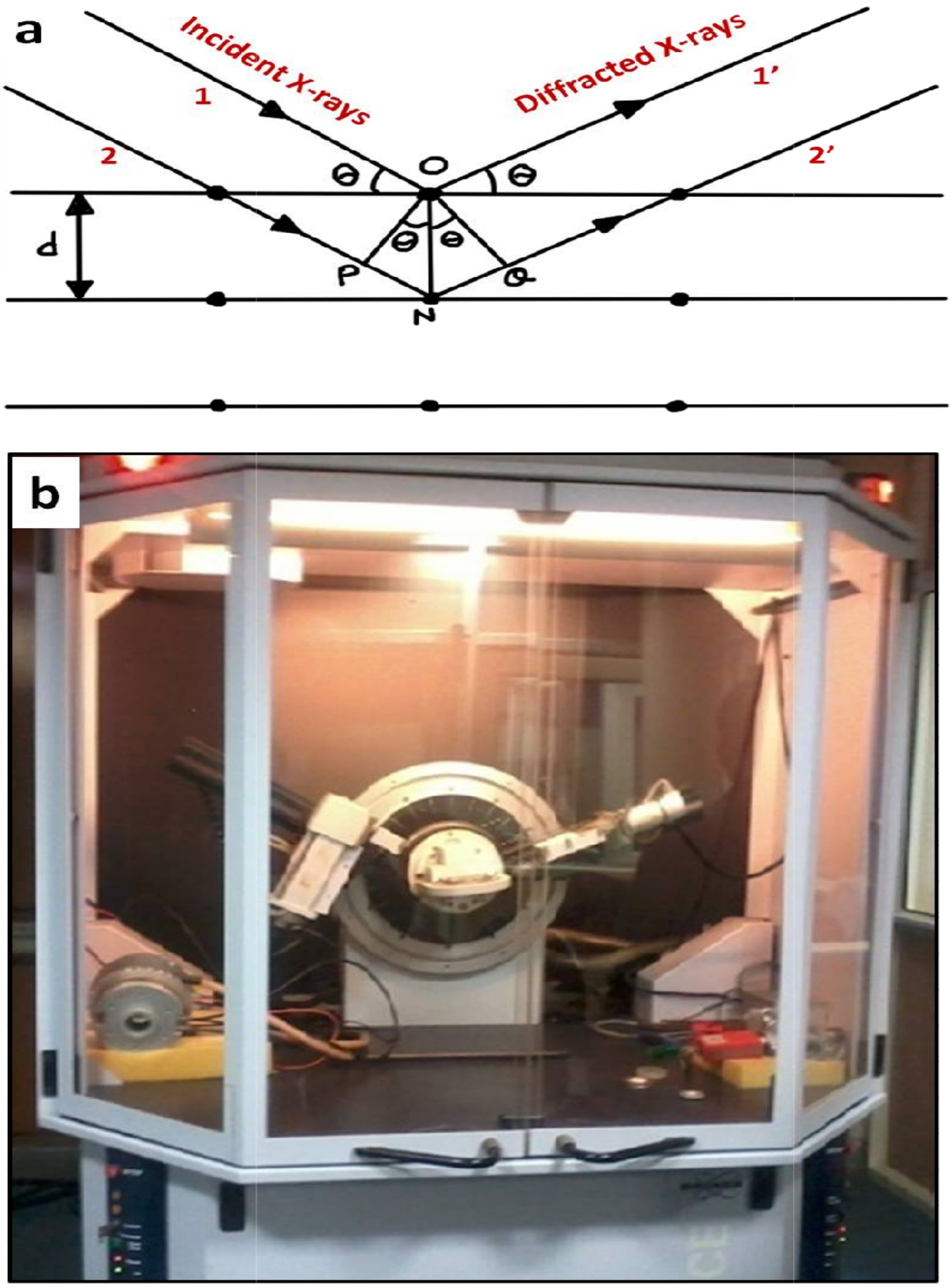

Figure 3.14 (a) XRD basic principle, (b) Set up of X-Ray Diffraction (Bruker D8 Adance) used for characterization

3.5.8 X-ray diffraction (XRD)

X-ray diffraction (XRD) is the non-destructive and versatile procedure that is used for the determination of crystal structure, lattice parameters, phases, residual stresses, and crystallographic texture in the material. In XRD, high energy and short wavelength (0.5-2.5 Å) X-rays are used as a medium to perform diffraction in the crystal. For diffraction, the wavelength (λ) of radiation employed must be of the order of the grating element. Since X-rays have a wavelength comparable to interatomic distance in crystal, therefore crystal behaves like the natural grating element for diffraction of X-rays. The essential condition to be satisfied for diffraction phenomena to occur is:

$$n\lambda = 2d\sin\theta$$

The above equation is called Bragg's law, shown in Figure 3.14 (a). Here'd' is interplanar spacing, '2θ' is scattering angle and 'n' should be an integer. Constructive interference should be there for diffraction phenomena to occur, therefore the distance PNQ travelled by 2-2' should be equal to $n\lambda$. XRD technique gives the variation of 2θ and intensity (in the form of peaks) data. The following data is used to recognize the type of material by matching them with the benchmark data compiled by the Joint Committee for Powder Diffraction Standard (JCPDS). In the present study, XRD analysis was carried out mainly for Mg_2Si phase identification in AS21A alloy through Bruker D8 Advanced X-ray Diffractometer shown by Figure 3.14 (b) having monochromatic Cu-Kα radiation (λ=1.540 Å, 2θ values: 20°–80° with Ni filter).

3.6 Mechanical Characterization

Experimental techniques employed in the present study for determining the mechanical features of specimens are Tensile Test and Microhardness test.

3.6.1 Tensile Test

Tensile test is utilized to determine the mechanical behaviour of materials under the uniaxial state of stress conditions. Properties such as Yield strength (YS), Ultimate Tensile Strength (UTS) and % elongation (ductility) can be found from the tension test. In tension test, load and elongation data is acquired which helps in calculating the various mechanical properties of the material through basic strength of materials equations. In the following study, a tension test was performed in room temperature conditions using dual-column Universal Testing Machine (UTM) set up (Tinius Olsen, Model: H50KS, Capacity: 50 kN) shown in Figure

3.15 at a constant crosshead speed of 2.5 mm/min. Longitudinal tensile specimens were prepared according to ASTM B557M-06 standard from the FSPed region.

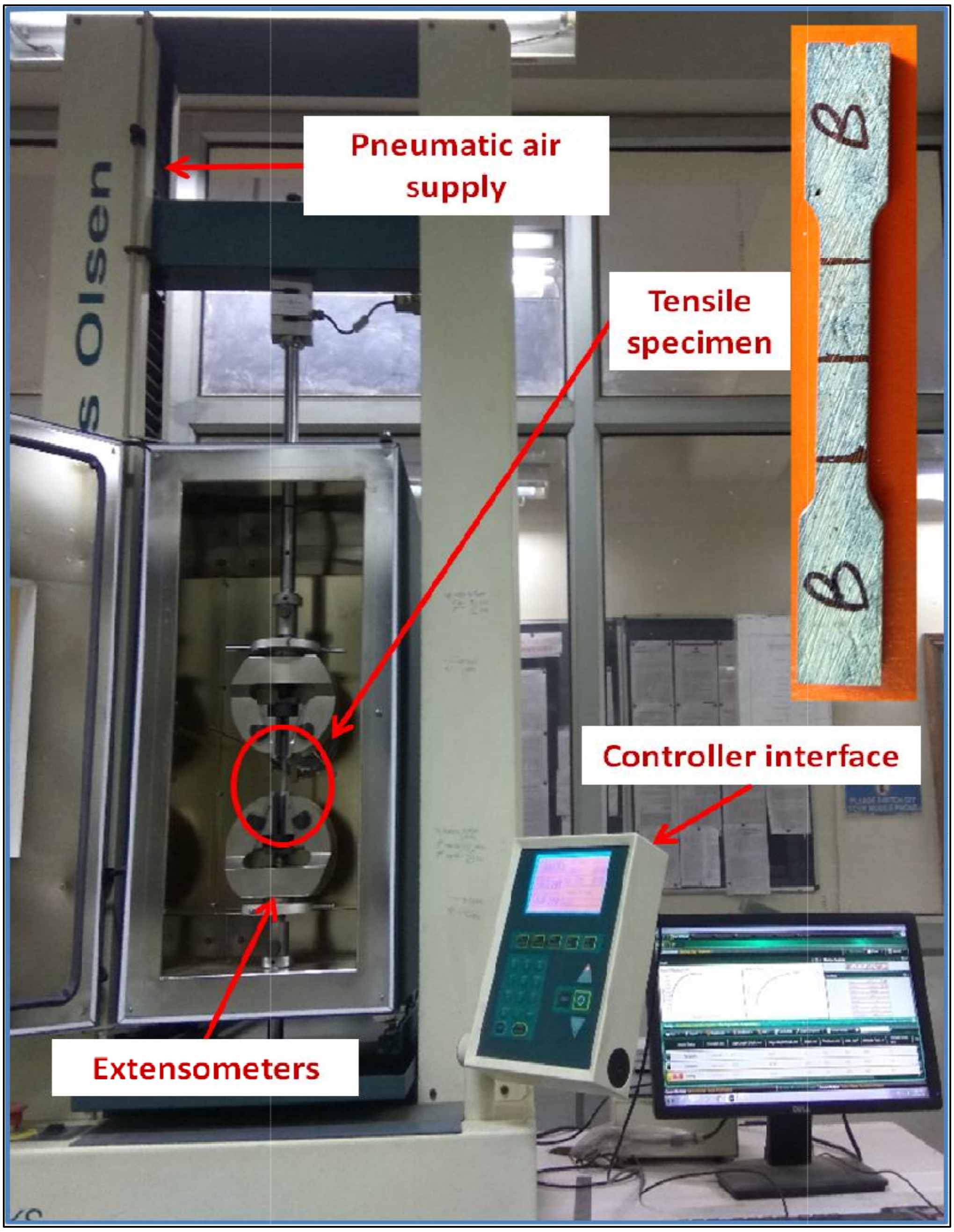

Figure 3.15 Universal Testing Machine (Tinius Olsen, Model: H50KS, Capacity: 50 kN) set up for the tensile test

3.6.2 Microhardness Test

The microhardness analysis was carried out using Vicker's hardness test. In this test, a square pyramid diamond indenter with a 136° angle between the opposite faces and a load ranging from 1 kg to 120 kg is used. Vicker's hardness test comprises of application of a definite load to the specimen surface using indenter for some duration as shown in Figure 3.16 (b) After removal of the load, the area of the indenter mark is measured in terms of diagonal of indentation (D) using a high-resolution microscope. Finally, the relation between the applied load and the area of indentation provides the hardness value of the concerned specimen. The Vicker's hardness number, indicated by HV, is computed by the following expression:

$$HV = \frac{1.8854\, P}{D^2}$$

where 'P' is the applied load in kg and 'D' is the measured average diagonal of indentation in mm.

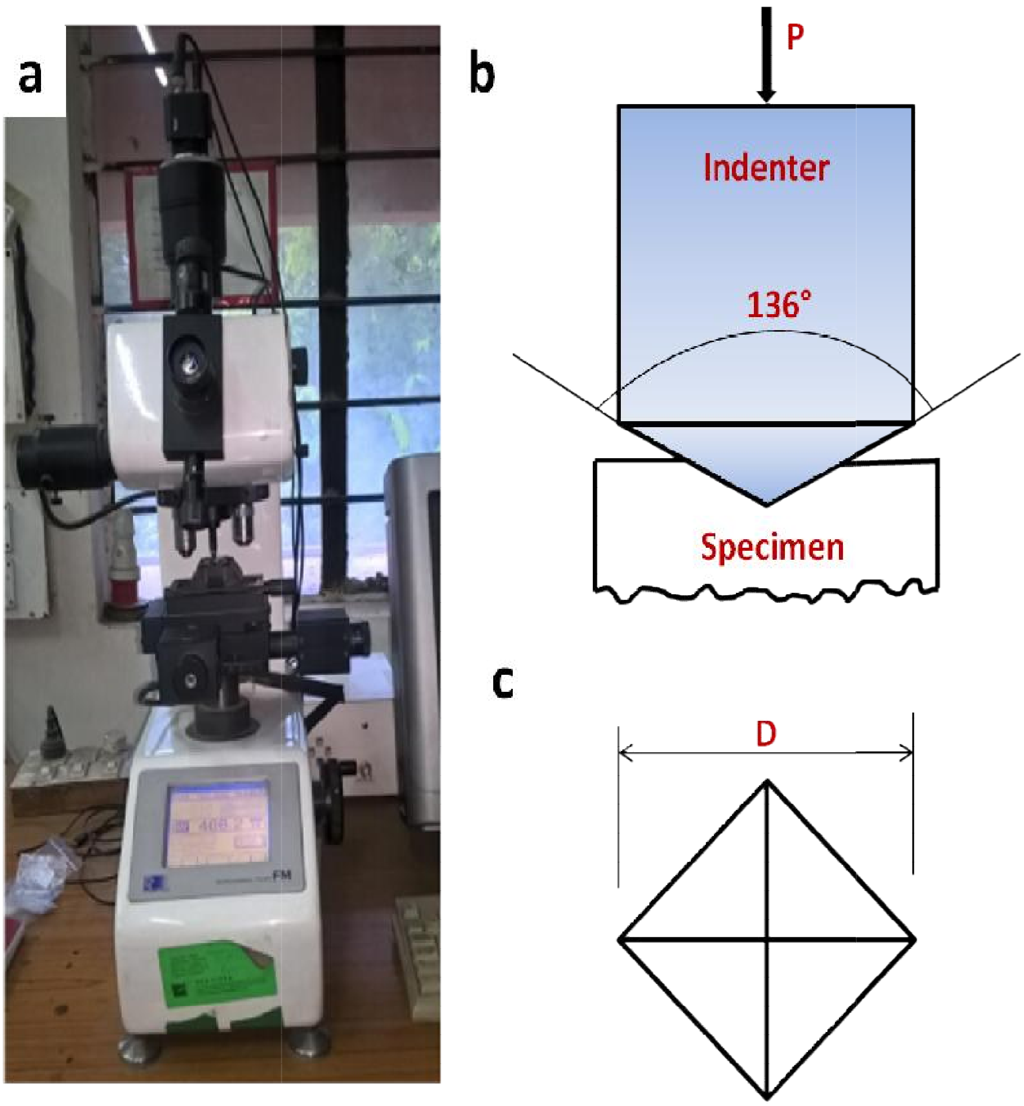

Figure 3.16 (a) Microhardness tester (Model: FM-e7, Future Tech, Japan); (b,c) Principle of indentation and measurement

The microhardness analysis was performed according to the ASTM E 92 standard using a microhardness machine having attachment of Vickers diamond pyramid indenter (136°) at a load of 100 gram and a dwell time of 10 seconds as shown in Figure 3.16. Before the test, specimens were polished to eliminate the oxide layer and other scales for a legible examination of the indentation spot. Indentations were done along (from left to right) and perpendicular (from top to bottom) in the SZ at an equal interval of 1 mm, and an average of six readings has been treated as the hardness value.

3.7 Tribological Characterization

Tribology is a multidisciplinary field of study and research that is focused on Wear, Friction and Lubrication which may affect the service life of a component or the efficient operation of machinery. The reduction in wear and optimization of friction are the dual primary objectives of Tribology for achieving energy conservation, increased productivity and reduced maintenance. Tribological characterization involves measurement of wear and friction coefficients between the Tribopairs i.e. components having relative or rubbing motion with each other.

3.7.1 Wear and Friction measurement

The wear characterization was performed according to the ASTM G99-04 standard using Pin-On-Disc Tribometer (Mfd: Ducom, model: TR-20 LE) as shown in Figure 3.17. The tribological properties of the specimens were measured in dry and lubricated conditions. In the POD apparatus, a specimen in the shape of a cylindrical pin is made to rub against the hard counter disc. The disc is made to rotate at variable speed, ranging from 200 to 2000 rpm, through a motor assembly. The pin is gripped in the holder of the respective size, which is further attached with the one end of the bell crank lever assembly. Another end of the assembly is coupled with the weight pan through wire & pulley arrangement. The dead weights placed on the flat pan are assigned to pin in the form of Normal load through bell crank lever assembly. The wear of the pin expressed in micrometres is given via the wear sensor by identifying the change in length of the pin in the micrometre. On the other hand, the frictional force between disc and pin interface is detected by the friction sensor. Lubrication arrangement is also attached in the POD setup for performing the wear test in wet conditions. For this, a continuous supply of lubricating oil at the interface of disc and pin is ensured through the pumping system. A dedicated storage tank is attached for keeping the lubricating oil. The schematic sketch (top and front view) of the wear testing equipment is depicted in Figure 3.18.

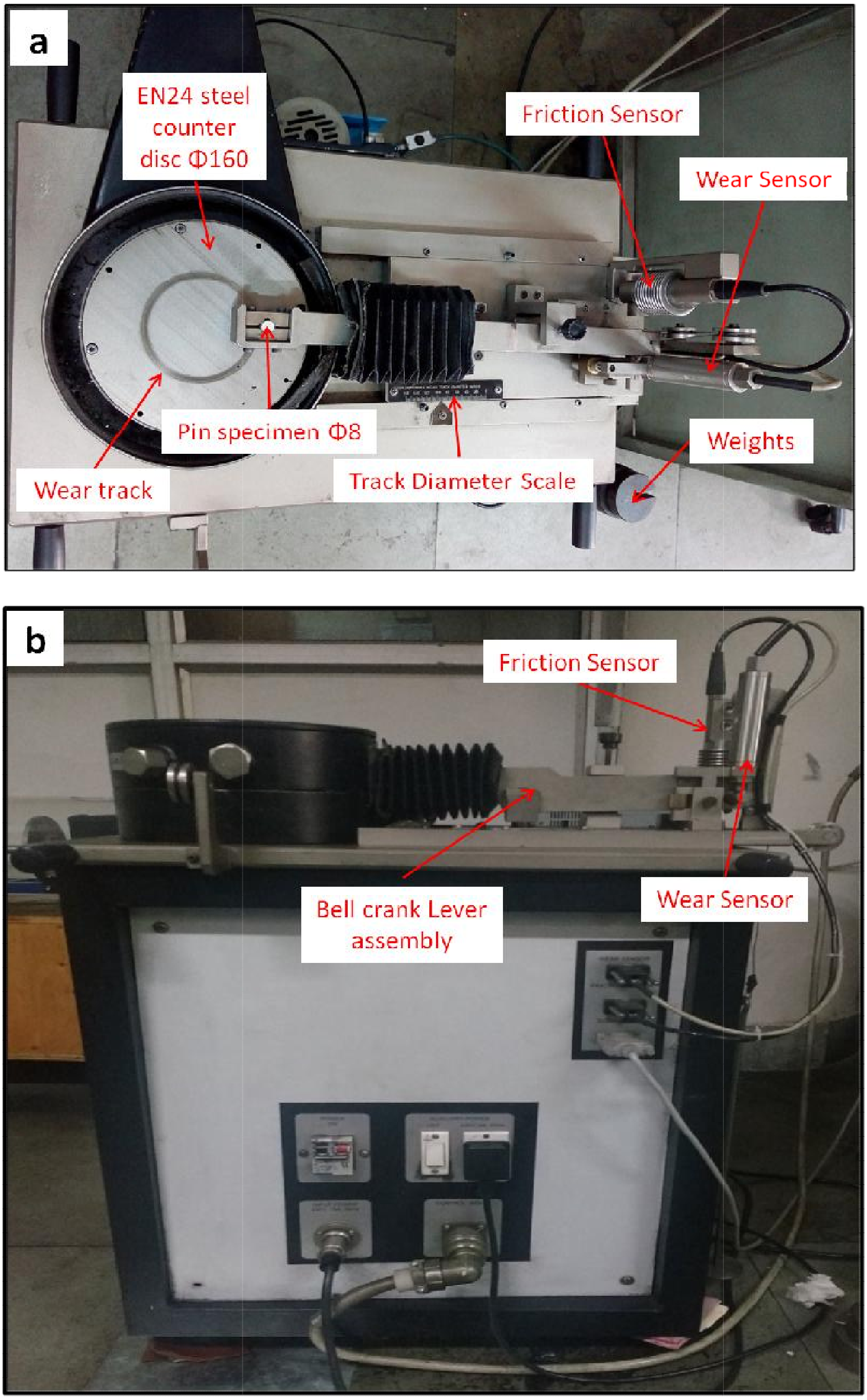

Figure 3.17 Pin-on-Disc Tribometer (Ducom mfd, model: TR-20 LE)

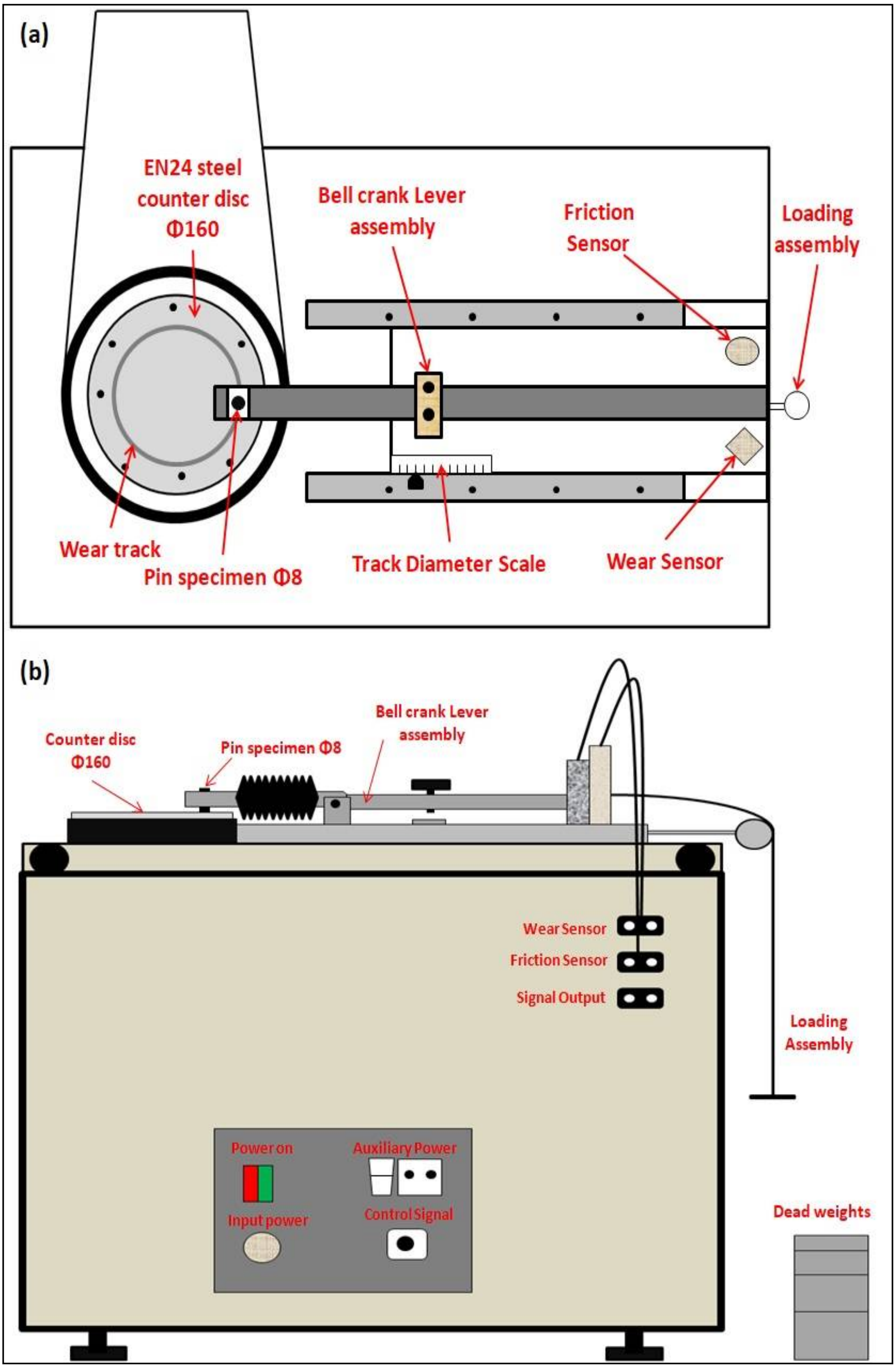

Figure 3.18 Schematic sketch showing Pin-on-Disc Tribometer (a) Top view and (b) Front view

The present study specified the specific wear rate for representing the wear of pin specimens. Specific wear rate (mm^3/Nm) was calculated with the help of following relation:

$$Specific\ wear\ rate = \frac{Volume\ loss\ (in\ mm^3)}{Normal\ load\ (in\ N) \times Sliding\ Distance\ (in\ m)}$$

The volume loss was evaluated by ratio of weight loss (g) and density (g/cm^3) of pin samples. Further, the weight loss was determined by measuring weight of pin samples before and after the wear test. The pin samples were rinsed with acetone before and after each wear test. The electronic weighing apparatus having an accuracy of 0.001mg was employed for measuring the weight of pin samples. The density of pin samples was considered as 1.75 g/cm^3, theoretically of magnesium alloy [5]. Besides, wear is presented in terms of the micrometre (µm), which was measured from the wear sensor attached to the Pin−on−Disc apparatus. The Coefficient of Friction (COF) between the counter disc and pin was determined by measuring the frictional force through the friction sensor of the wear testing apparatus. The expression used for evaluating the COF is:

$$COF = \frac{Frictional\ Force\ (in\ N)}{Normal\ load\ (in\ N)}$$

The wear experiment was performed at least 3 times for each load level to ensure the consistency of results and the average of them was considered as a final reading. The pin worn surfaces were characterised with SEM and EDS resources to identify the wear mechanism involved.

CHAPTER 4

RESULTS AND DISCUSSIONS

In this chapter, the experimental and optimization results are presented and analysed. The major research objectives of the current thesis have been discussed thoroughly with the supporting literature.

4.1 Implementation of Taguchi-GRA-PCA hybrid approach

The objective of the Taguchi-Grey Relational Analysis (GRA)-Principal Component Analysis (PCA) optimisation approach is to determine the optimal combinations of the process parameters for the FSP of cast AS21A magnesium alloy. The Minitab 17 statistical software was utilized in this particular optimisation phenomenon. The implementation of the optimisation analysis is achieved step by step as follows:

1. Selection of input/process parameters and their levels.
2. Selection of performance attributes.
3. Selection of Orthogonal Array as per Taguchi design.
4. Carry out experiments as per the OA and obtain the values of performance attributes.
5. Calculation of S/N ratio corresponding to each performance attributes.
6. Normalization of the S/N ratio i.e. Grey Relational Generation.
7. Calculation of Grey Relational Coefficient (GRC) using deviation sequence.
8. Computation of Grey Relational Grade (GRG) using PCA.
9. Determination of the optimal level of process parameters.
10. Performing statistical analysis of variance (ANOVA).
11. Prediction of GRG value at optimal levels.
12. Performing confirmation experiments.

The first four steps are already performed and discussed in chapter 3. In brief, the FSP of cast AS21A alloy was carried out as per L9 Taguchi OA with the different settings of influencing process parameters. Rotational speed (RS), Travel Speed (TS) and Shoulder Diameter (SD) was the input variables while UTS (MPa), Ductility (ε) and Microhardness (HV) were measured as the performance attributes. The remaining steps are discussed and analysed in the upcoming section.

4.1.1 Calculation of Signal−to−Noise ratio

The performance attributes attained from the experimental results, as listed in Table 4.1, are initially transformed into an S/N ratio to seek the desired result with the best performance and the smallest variance. The enhanced mechanical behaviour of the material after the FSP operation is exhibited by the higher values of UTS, ductility and hardness. Therefore in the current investigation, S/N value was calculated as per "larger-the-better" criterion to maximize the performance attributes. The experimental results are substituted in Eqn. 4.1 to determine the S/N ratios corresponding to each response as shown in Table 4.1. S/N ratio with "larger-the-better" attribute can be evaluated from the following expression:

$$\text{S/N ratio } (\eta) = -10\log_{10}\frac{1}{n}\sum_{i=1}^{n}\frac{1}{y_i^2} \quad (4.1)$$

where, n is the total number of experiments and y_i represents the experimental values of the i^{th} experiment.

Table 4.1 S/N ratios of different performance attributes

Exp. No.	Input factors			Performance attributes			Signal-to-noise ratio (S/N ratio)		
	RS	TS	D	UTS (MPa)	ε (%)	HV	$(S/N)_{UTS}$	$(S/N)_{\varepsilon}$	$(S/N)_{HV}$
1	400	20	16	88.4	5.32	62.2	38.9290	14.5182	35.8758
2	400	50	20	91.8	6.72	64.1	39.2569	16.5474	36.1372
3	400	80	24	89.9	5.43	65.5	39.0752	14.6960	36.3248
4	800	20	20	89.4	10.1	64.7	39.0268	20.0864	36.2181
5	800	50	24	90.2	9.31	66.2	39.1041	19.3790	36.4172
6	800	80	16	89.2	9.75	65.5	39.0073	19.7801	36.3248
7	1200	20	24	90.3	7.95	64.3	39.1138	18.0073	36.1642
8	1200	50	16	91.5	5.58	63.6	39.2284	14.9327	36.0691
9	1200	80	20	91.1	7.12	64.9	39.1904	17.0496	36.2449

4.1.2 Normalization of the S/N ratio

GRA starts with the normalization of the original sequences of S/N ratios, which is known as grey relational generation. In the current investigation, the target is to maximize the reference sequence for each attribute thus "larger the better" criterion was used for data normalization.

S/N ratio values depicted in Table 4.1 were considered as reference sequence $[x_i^r(k)]$. The sequence obtained after normalization of reference sequence is called the comparability sequence$[x_i^c(k)]$. The comparability sequences for each attribute were calculated from the following expression:

$$x_i^c(k) = \frac{x_i^r(k) - min\, x_i^r(k)}{max\, x_i^r(k) - min\, x_i^r(k)} \tag{4.2}$$

where, $x_i^r(k)$ and $x_i^c(k)$ denotes reference sequence and comparability sequence respectively, $max\, x_i^r(k)$ and $min\, x_i^r(k)$ are the greatest and smallest value in reference sequence respectively, $i = 1,2,3,\ldots\ldots, m\ and\ k = 1,2,3,\ldots\ldots, n$; m is the no. of experimental runs and n is the no. of responses. In the present case, $m = 9$ and $n = 3$. The outcomes of grey relational generation obtained from Eqn. 4.2 are presented in Table 4.2.

Table 4.2 Normalization of S/N ratio data or Grey Relational Generation

Exp. No.	$(S/N)_{UTS}$	$(S/N)_{\varepsilon}$	$(S/N)_{HV}$
Reference sequence $[x_i^r(k)]$	1.0000	1.0000	1.0000
Comparability sequence: $[x_i^c(k)]$			
1	0.0000	0.0000	0.0000
2	1.0000	0.3644	0.4827
3	0.4458	0.0319	0.8294
4	0.2981	1.0000	0.6322
5	0.5341	0.8730	1.0000
6	0.2388	0.9450	0.8294
7	0.5634	0.6266	0.5327
8	0.9131	0.0744	0.3571
9	0.7971	0.4546	0.6817

For instance, the comparability sequence of each attribute for experiment no. 3 ($i = 3$) is calculated as follows:

$$x_3^c(UTS) = \frac{x_3^r(UTS) - min\, x_i^r(UTS)}{max\, x_3^r(UTS) - min\, x_3^r(UTS)} = \frac{39.0752 - 38.9290}{39.2569 - 38.9290} = 0.4458$$

$$x_3^c(\varepsilon) = \frac{x_3^r(\varepsilon) - min\, x_i^r(\varepsilon)}{max\, x_3^r(\varepsilon) - min\, x_3^r(\varepsilon)} = \frac{14.6960 - 14.5182}{20.0864 - 14.5182} = 0.0319$$

$$x_3^c(HV) = \frac{x_3^r(HV) - min\, x_i^r(HV)}{max\, x_3^r(HV) - min\, x_3^r(HV)} = \frac{36.3248 - 35.8758}{36.4172 - 35.8758} = 0.8294$$

A similar procedure will be adopted for $i = 1\ to\ 9$.

4.1.3 Calculation of grey relational coefficients using deviation sequences

The next step in GRA is to calculate the value of Grey Relational Coefficients (GRCs). GRC $[\Gamma_i(k)]$ establish the relationship between the reference sequences $[x_i^r(k)]$ and comparability sequences $[x_i^c(k)]$ and is calculated from the following expression:

$$\Gamma[x_i^c(k), x_i^r(k)] = \frac{\triangle_{min}(k) + \xi\, \triangle_{max}(k)}{\triangle_{rc}(k) + \xi\, \triangle_{max}(k)} \tag{4.3}$$

where, $\triangle_{rc}(k)$ known as deviation sequence given by:

$$\Delta_{rc}^i(k) = ||x_i^c(k) - x_i^r(k)|| \tag{4.4}$$

$\xi \in [0,1]$ called a distinguishing coefficient.

$\triangle_{max} = max_{\forall j \in i} max_{\forall j \in k} ||x_i^c(k) - x_i^r(k)||$ is the largest value of $\triangle_{rc}(k)$ (4.5)

$\triangle_{min} = min_{\forall j \in i} min_{\forall j \in k} ||x_i^c(k) - x_i^r(k)||$ is the smallest value of $\triangle_{rc}(k)$ (4.6)

The GRC value was determined by first calculating the value of the deviation sequence from Eqn. 4.4. The values of deviation sequences calculated are presented in Table 4.3. For experiment no. 3 ($i = 3$), deviation sequence for each attribute is calculated as follows:

$$\Delta_{rc}^3(UTS) = ||x_i^c(k) - x_i^r(k)|| = ||0.4458 - 1.000|| = 0.5542$$

$$\Delta_{rc}^3(\varepsilon) = ||x_i^c(k) - x_i^r(k)|| = ||0.0319 - 1.000|| = 0.9681$$

$$\Delta_{rc}^3(HV) = ||x_i^c(k) - x_i^r(k)|| = ||0.8294 - 1.000|| = 0.1706$$

Table 4.3 Deviation sequence corresponding to each attribute $[\Delta_{rc}^i(k)]$

Deviation sequences	$\triangle_{rc}\ (\boldsymbol{UTS})$	$\triangle_{rc}\ (\boldsymbol{\varepsilon})$	$\triangle_{rc}\ (\boldsymbol{HV})$
Exp. No. 1, $i = 1$	1.0000	1.0000	1.0000
Exp. No. 2, $i = 2$	0.0000	0.6356	0.5173
Exp. No. 3, $i = 3$	0.5542	0.9681	0.1706
Exp. No. 4, $i = 4$	0.7019	0.0000	0.3678
Exp. No. 5, $i = 5$	0.4659	0.1270	0.0000
Exp. No. 6, $i = 6$	0.7612	0.0550	0.1706
Exp. No. 7, $i = 7$	0.4366	0.3734	0.4673
Exp. No. 8, $i = 8$	0.0869	0.9256	0.6429
Exp. No. 9, $i = 9$	0.2029	0.5454	0.3183

From Table 4.3 of the deviation sequence, it can be inferred that the value of $\triangle_{min}$ and $\triangle_{max}$ will be 0 and 1 respectively. In the present study, equal weight was chosen, therefore the value of ξ is taken as 0.5. Finally, putting all the obtained values in Eqn. 4.3, all 9 values of GRCs $[\Gamma_{\mathrm{i}}(\mathrm{k})]$ were obtained corresponding to each attribute as reported in Table 4.4. For experiment no. 3 ($i = 3$), the value of GRCs is calculated as follows:

$$\Gamma_3(\mathrm{UTS}) = \frac{0.5}{\Delta_{rc}^3(UTS) + 0.5} = \frac{0.5}{0.5542 + 0.5} = 0.4743$$

$$\Gamma_3(\varepsilon) = \frac{0.5}{\Delta_{rc}^3(\varepsilon) + 0.5} = \frac{0.5}{0.9681 + 0.5} = 0.3406$$

$$\Gamma_3(\mathrm{HV}) = \frac{0.5}{\Delta_{rc}^3(HV) + 0.5} = \frac{0.5}{0.1706 + 0.5} = 0.7456$$

A similar procedure will be adopted for $i = 1\ to\ 9$.

Table 4.4 Calculated Grey Relational Coefficient (GRC) and Grey Relational Grade (GRG) for 9 comparability sequences

Exp. No.	GRC $[\Gamma_{\mathrm{i}}(\mathrm{k})]$			GRG $[\Psi_{\mathrm{i}}]$*
	$\Gamma_{\mathrm{i}}(\mathrm{UTS})$	$\Gamma_{\mathrm{i}}(\varepsilon)$	$\Gamma_{\mathrm{i}}(\mathrm{HV})$	
$i = 1$	0.3333	0.3333	0.3333	0.3332
$i = 2$	1.0000	0.4403	0.4915	0.6024
$i = 3$	0.4743	0.3406	0.7456	0.5072
$i = 4$	0.4160	1.0000	0.5762	0.7094
$i = 5$	0.5177	0.7974	1.0000	0.7903
$i = 6$	0.3964	0.9009	0.7456	0.7186
$i = 7$	0.5339	0.5725	0.5169	0.5440
$i = 8$	0.8520	0.3507	0.4375	0.5092
$i = 9$	0.7113	0.4783	0.6111	0.5819

*Average grey relational grade (Ψ_{m}) is 0.5885

4.1.4 Calculation of grey relational grade using principal component analysis

Last step in GRA is the determination of Grey Relational Grade (GRG). GRG is calculated via averaging the sum of GRCs with the help of following equation:

$$\Psi[x_i^c, x_i^r] = \sum_{k=1}^{n} \delta_k \, \Gamma[x_i^c(k), x_i^r(k)] \tag{4.7}$$

where, δ_k represents the fraction values of k^{th} response, and $\sum_{k=1}^{n} \delta_k = 1$.

The concept of Principal Component Analysis (PCA) is particularly introduced here for assigning the fraction values(δ_k) to each performance attribute, thereby computing the GRG value corresponding to each experiment. The objective of using PCA was to illustrate the relative importance of each performance attribute in the GRA. The first step in PCA is to formulate a multiple attribute matrix having performance attributes like the number of rows i.e. 3, and the number of experiments i.e. 9 as the number of columns. The values of GRCs [$\Gamma_i(k)$] listed in Table 4.4 represent the elements of the [3×9] multiple attribute matrix. The second step is to compute the correlation coefficient matrix from matrix data and corresponding Eigen values are determined from Eqn. 4.8 as shown in Table 4.5. The Eigen vector related to each Eigen value is depicted in Table 4.6 and their squares signify the fraction values of the corresponding performance attribute to the principal component. The Eigen values and Eigen vectors were determined from Eqn. 3.12:

Table 4.5 Eigen values and explained variation for principal components

Principal Component	Eigen value	Proportion	Cumulative
1st	1.7709	0.59	0.59
2nd	0.7787	0.26	0.85
3rd	0.4504	0.15	1

Table 4.6 Eigen vectors for principal components

Performance attributes	**Eigenvector**		
	1st principal component	2nd principal component	3rd principal component
UTS (MPa)	-0.51	-0.793	0.334
ε (%)	0.643	-0.094	0.76
HV	0.571	-0.602	-0.558

Table 4.7 shows the fraction values of UTS, Elongation and Microhardness as 0.2601, 0.4134 and 0.3260 respectively. Further, the variance for the first principal component representing all 3 attributes, is as large as 87.79%. Thus, the squares of their corresponding Eigen vectors are assigned as the fraction values (δ_k) of the performance attribute in the calculation of GRG. Finally, the value of GRG $\{\Psi[x_i^c, x_i^r]\}$ was obtained for each experiment

using Eqn. 4.7 by substituting the values of δ_k from Table 4.7. For experiment no. 3 ($i = 3$), the value of GRG is calculated as follows:

$$\Psi_3 = 0.2601 \times \Gamma_i(\mathrm{UTS}) + 0.4134 \times \Gamma_i(\varepsilon) + 0.326 \times \Gamma_i(\mathrm{HV})$$
$$= 0.2601 \times 0.4743 + 0.4134 \times 0.3406 + 0.326 \times 0.7456$$
$$= \mathbf{0.5072}$$

Using a similar calculation, the GRG values were obtained for all the experiments ($i = 1\ to\ 9$) and are shown in Table 4.4. Thus, using GRA analysis, the entire study can be confined to optimisation of a single grey relational grade in place of the complex and multiple performance attributes. In other words, multiple responses involved in the present problem are transformed into a single output called Grey Relational Grade (GRG).

Table 4.7 Fraction value of each performance attribute corresponding to 1st Principal Component

Performance attributes	**Fraction value ($\boldsymbol{\delta_k}$)**
Ultimate Tensile Strength (UTS)	0.2601
Elongation (ε)	0.4134
Microhardness (HV)	0.3260

4.1.5 Determination of optimal level of process parameters

Response table of the Taguchi procedure depicts value of the average GRG for each process parameter settings. Since the selected experimental layout is orthogonal, thus it is feasible to sort out GRGs corresponding to the levels of the FSP parameter in each column of the design array, and computing an average of those GRGs with the same level. For example, FSP parameter Rotational Speed was set at level 1 for experiment no., $i = 1,2,3$ according to the L9 orthogonal array depicted in Table 4.1. The average of the GRGs corresponding to $i = 1,2,3$ will represent the GRG value of the level 1 RS (RS_1) and is computed as follows:

$$RS_1 = \frac{0.3332 + 0.6024 + 0.5072}{3} = 0.4809$$

Similarly,

$$RS_2 = \frac{0.7094 + 0.7903 + 0.7186}{3} = 0.7394$$

$$RS_3 = \frac{0.5440 + 0.5092 + 0.5819}{3} = 0.5451$$

Using similar above procedure, calculations are done for each process parameter and accordingly the response table is created as depicted in Table 4.8. Better product quality is attributed to larger value of grey relational grade. Thus, the setting exhibiting the largest value of GRG is selected as the optimum setting of that particular input parameter. Therefore, it can be inferred from the response table for GRG presented in Table 4.8 that optimal setting of the input parameters for better response is $RS_2TS_2D_2$. The optimal setting $RS_2TS_2D_2$ for the FSP of cast AS21A alloy can also be inferred from the graphical representation of the S/N ratio for overall GRG as shown in Figure 4.1.

Table 4.8 Response table for the GRG

Designation	Input Parameters	Level 1	Level 2	Level 3	Max-Min	Rank
RS	Rotational Speed (rpm)	0.4809	0.7394*	0.5451	0.2585	1
TS	Travel Speed (mm/min)	0.5289	0.634*	0.6026	0.1051	3
D	Shoulder Diameter (mm)	0.5203	0.6313*	0.6139	0.1109	2

*optimum settings for input parameters

4.1.6 Performing statistical analysis of variance (ANOVA)

In further optimisation analysis, ANOVA was utilized to determine significance and contribution of each input parameter influencing the performance attributes. The findings of ANOVA for the GRG are presented in Table 4.9. It can be inferred that the rotational speed is the most notable input parameter (71.27 %) influencing the characteristics of FSPed AS21A alloy followed by shoulder diameter (13.99 %) and travel speed (11.44 %). The results of ANOVA are also in agreement with the graphical representation shown by Figure 4.1.

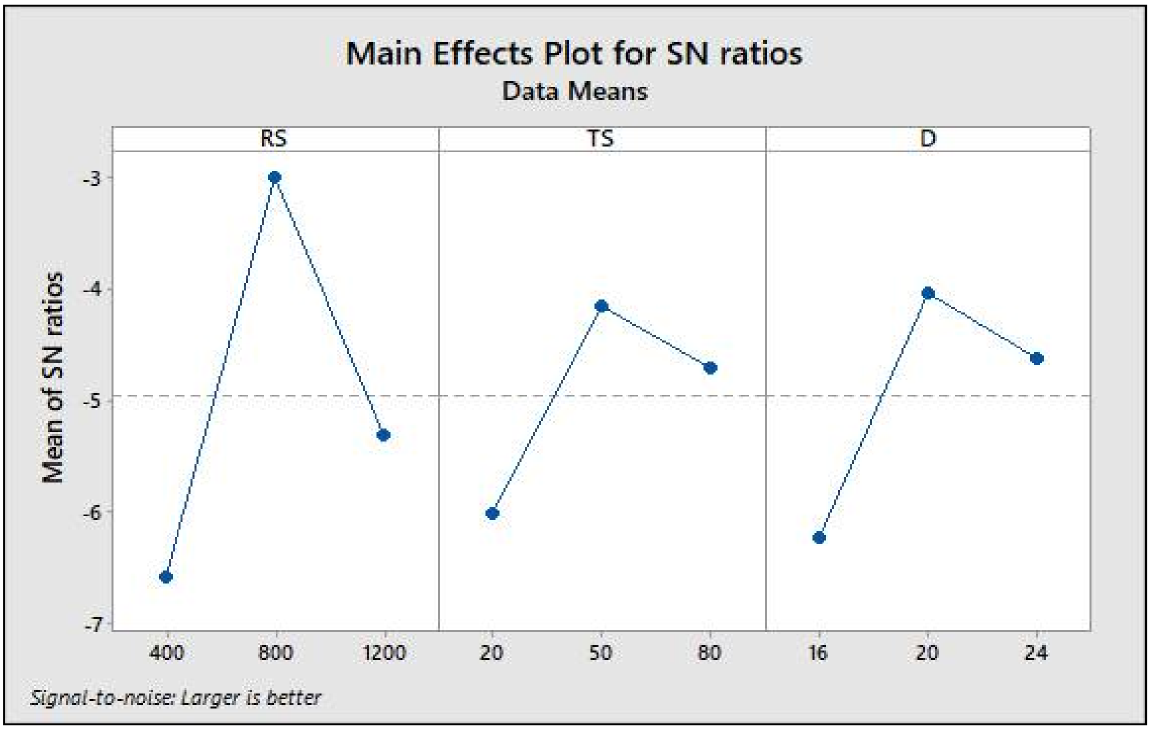

Figure 4.1 Graphical representation of S/N ratio with different levels of process parameters

Table 4.9 ANOVA results

Input Parameters	DoF*	Adj SS*	Adj MS*	F value	P value	% contribution
RS	2	0.1087	0.0544	21.63	0.044	71.27
TS	2	0.0175	0.0087	3.47	0.224	11.44
D	2	0.0213	0.0107	4.25	0.191	13.99
Error	2	0.0050	0.0025			3.29
Total	8	0.1526				100

*DoF: Degree of Freedom, SS: Sum of Square, MS: Mean Square

In friction stir processing, the mechanical properties of the material are significantly influenced by amount of heat generated during FSP. An appreciable amount of heat input leads to better consolidation and material movement in the processed region. The maximum contribution of rotational speed, as inferred from ANOVA results, can be attributed to the strong dependency of rotational speed on peak temperature [141]. At very low RS, defects like pin holes and cracks appear due to insufficient heat generation which leads to the poor consolidation of material around the tool pin. This results in lower mechanical characteristics of the material. On the other side, too high rotational speed creates an appreciable amount of turbulence in the processed region which leads to a reduction in the forging action and material consolidation [134].

Furthermore, too high travel speed leads to less heat input thus causing defects like cracks or pinholes, resulting in lower mechanical properties. On contrary, too low travel speed of tool leads to higher heat input which results in enhancement of grain growth and heat-affected zone, thus exhibiting lower mechanical behaviour [138].

In a similar manner, shoulder diameter is also having a direct relation with heat generation. The large shoulder diameter leads to high heat generation which can be attributed to a wider contact area, resulting in the formation of coarse grains in stirred region and subsequently deteriorating the mechanical properties. On contrary, due to the narrow contact area in the case of small shoulder diameter, heat generation is less and therefore the metal consolidation is not so fine enough in the stirred zone [135].

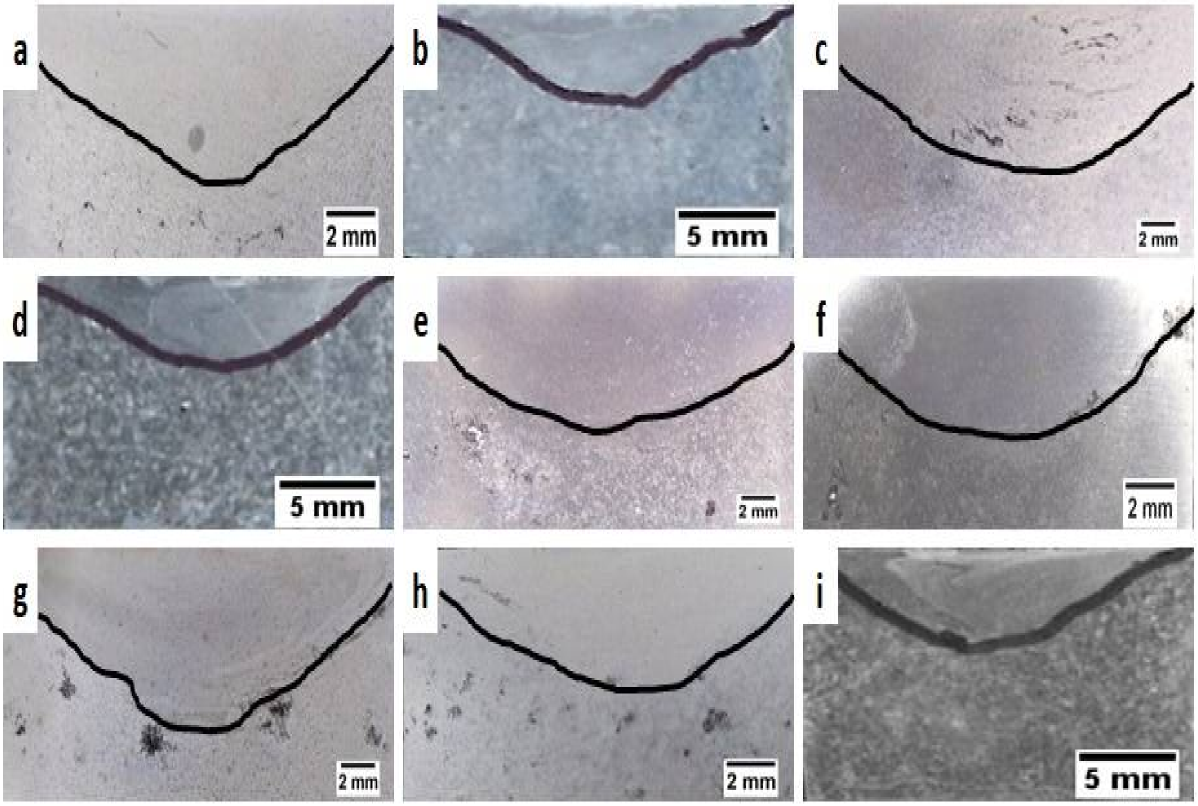

Figure 4.2 Macrographs showing FSP impression in all L9 samples ($i = 1\ to\ 9$)

In the present study, defect-free processed zones were formed in the FSP of cast AS21A alloy processed at various parameters, as inferred from the macrographs shown in Figure 4.2. The fractography of the various tensile samples tested is shown in Figure 4.3.

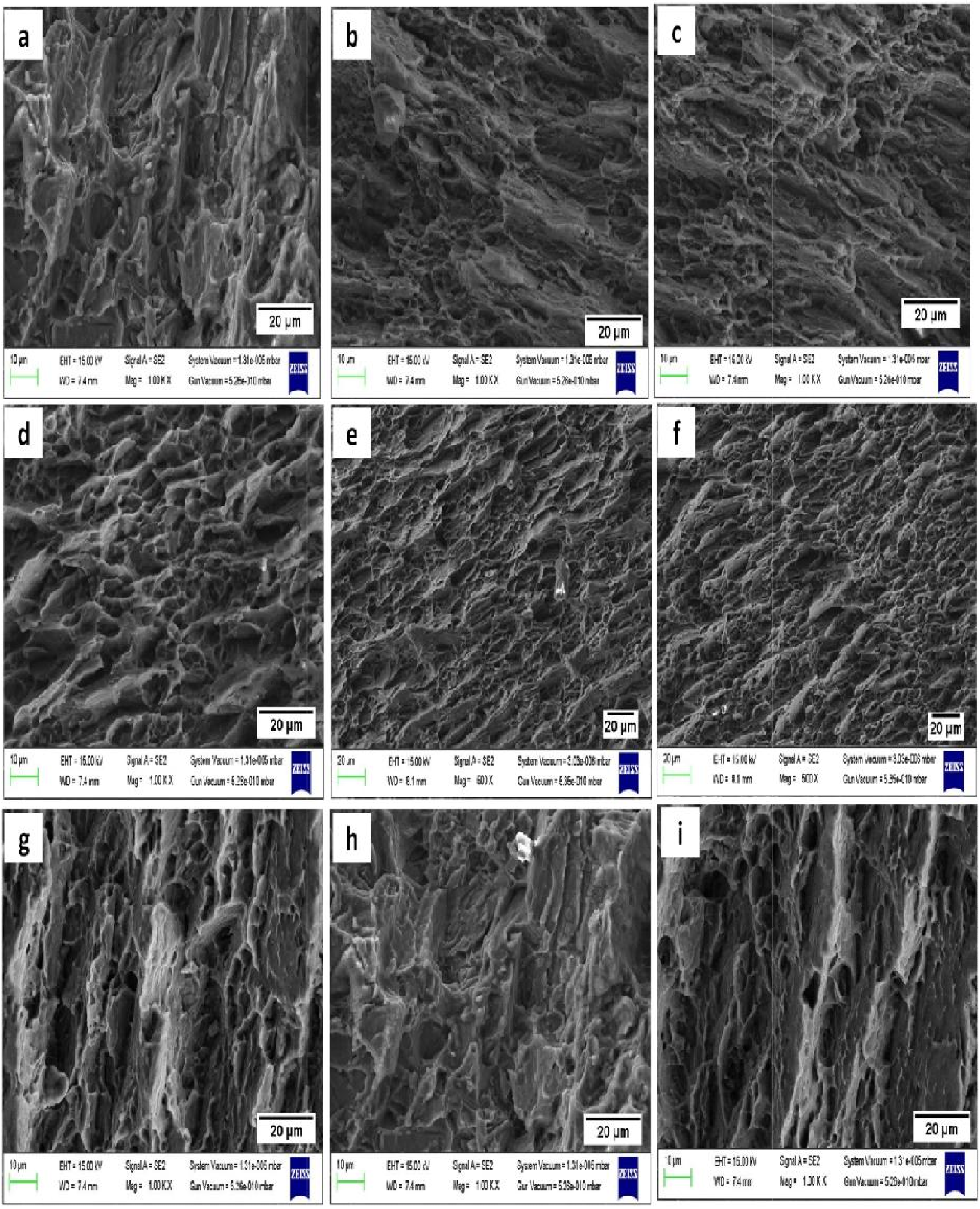

Figure 4.3 Morphology of all L9 fractured tensile specimens ($i = 1\ to\ 9$)

4.1.7 Prediction of GRG value at optimal levels

The GRG value is predicted at the optimal level of process parameters to confirm the enhancement in GRG value. In the present study, GRG value was predicted using an additive model [138] which is given by Eqn. 4.9.

$$\Psi_p = \Psi_m + \sum_{i=1}^{q} (\overline{\Psi}_i - \Psi_m) \tag{4.9}$$

where Ψ_p is predicted GRG, Ψ_m is total mean of GRG which can be obtained from Table 4.4 as 0.5885 and $\overline{\Psi}_i$ is the mean of GRG at optimal settings which can be inferred from Table 4.8 as 0.7394, 0.634, and 0.6313, and q is the number of input parameters which is 3. Therefore, from Eqn. 4.9, the predicted value of GRG can be calculated as:

$$\Psi_p = \mathrm{RS}_2 + \mathrm{TS}_2 + D_2 - 2\Psi_m$$

$$\Psi_p = 0.7394 + 0.634 + 0.6313 - 2(0.5885) = \mathbf{0.8277}$$

It can be inferred that the predicted value of GRG is highest amid all GRG values. Hence, enhancement by 0.0374 in GRG value is confirmed as depicted in Table 4.10.

4.1.7 Performing confirmation experiments

The confirmation experiment was performed at optimal settings to examine the accuracy of the predicted GRG value. The FSP of cast AS21A alloy was done at a rotational speed of 800 rpm, travel speed of 50 mm/min and a shoulder diameter of 20 mm. It is evident from the confirmation experiment results, depicted in Table 4.10 that the GRG value obtained from prediction and the value obtained experimentally are approximately close to each other.

Table 4.10 GRG values of initial, predicted, and confirmation run

	Initial data	**Optimal parameter setting**	
		Prediction	**Experimental**
Setting level	$RS_2TS_2D_3$	$RS_2TS_2D_2$	$RS_2TS_2D_2$
Ultimate Tensile Strength (UTS) in MPa	90.2		88.6
Elongation (ε) in %	9.31		10.6
Microhardness in HV	66.2		66
GRG	0.7903	0.8277*	0.8299

*Improvement in the GRG value is 0.0374

In the forthcoming investigation, the detailed microstructural, mechanical and wear analysis was carried out at an optimal set of process parameters, achieved from the statistical and mathematical approaches. The effect of FSP on the microstructural and mechanical features of Mg-Al-Si based AS21A alloy casting has been investigated. The aim was to analyse the effect of FSP on the coarse Chinese script morphology of thermally stable Mg_2Si phase present in the AS21A matrix.

4.2 Structural analysis

4.2.1 Microstructural analysis of Cast AS21A alloy

The OM image of the cast AS21A magnesium alloy is depicted in Figure 4.4. It is evident that the parent material microstructure was characterised by the α-Mg grains surrounded by the eutectic network of coarse intermetallic compounds distributed at the grain boundaries. The coarse intermetallic morphology appeared as Chinese script which confirmed the presence of hard and brittle thermally stable Mg_2Si phase as depicted in the inset of Figure 4.4. SEM along with the EDS spectrum shown in Figure 4.5 confirmed the presence of main alloying elements. More details of cast AS21A alloy are shown in Figure 4.6. Moreover, as shown in Figure 4.7, the XRD graph of AS21A alloy justified the presence of Mg_2Si phase in magnesium matrix. Microstructural findings of AS21A alloy were in good agreement with the literature [143-146-37] since PM was prepared through the casting route, that's why it was obvious for the evolution of coarse Mg_2Si precipitates in the matrix. Further, casting defects particularly porosity and voids were present in the parent material.

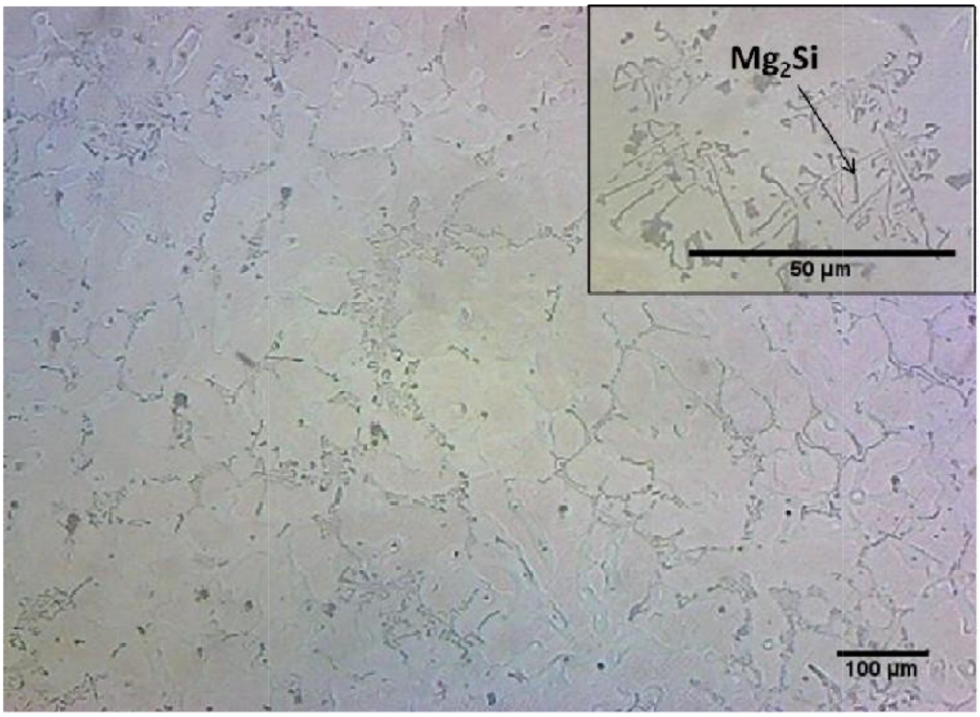

Figure 4.4 Microstructure of the cast AS21A alloy

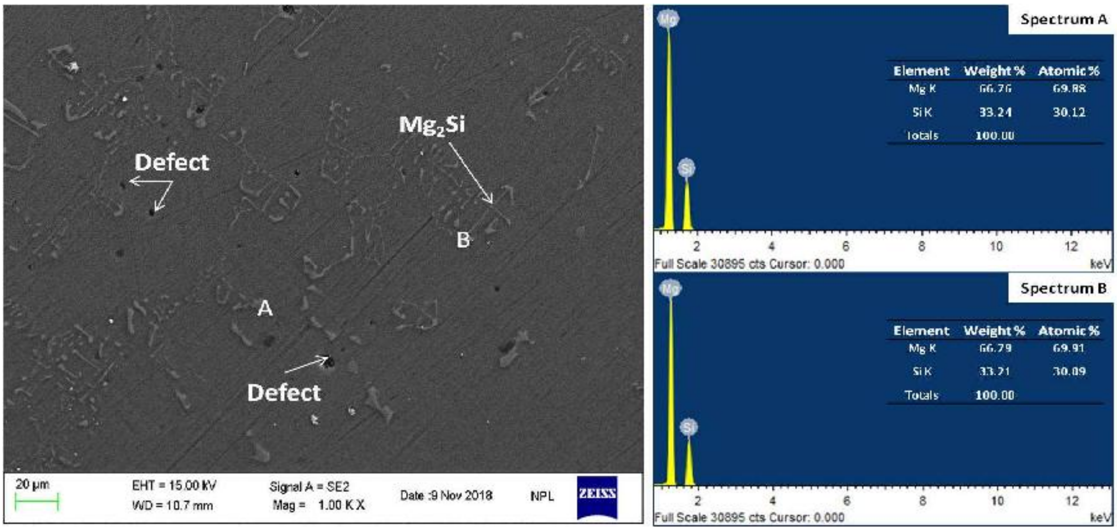

Figure 4.5 SEM with EDS of cast AS21A alloy

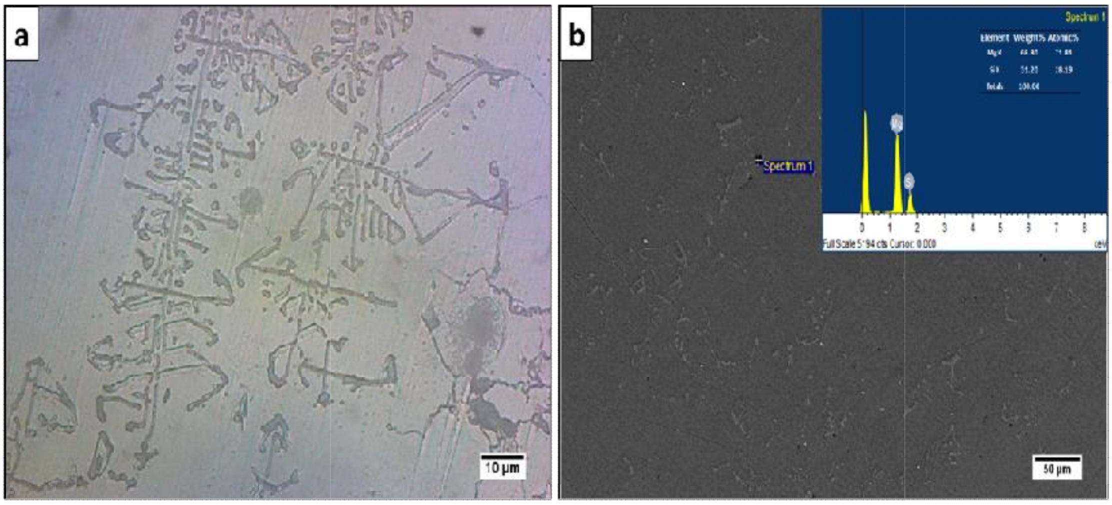

Figure 4.6 Microstructural features of cast AS21A alloy at different location

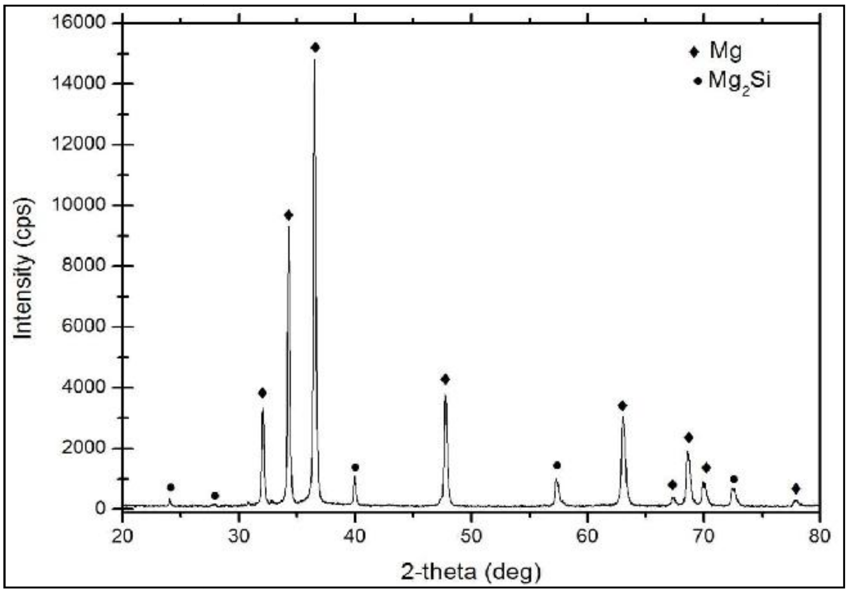

Figure 4.7 XRD pattern of cast AS21A alloy

4.2.2 Microstructural analysis of FSPed AS21A alloy

AS21A alloy when subjected to FSP at three different rpm: 400 (F1), 800 (F2) and 1200 (F3), a distinct impression referred to as the Stirred Zone (SZ) appeared as shown by the macrograph shown in Figure 4.8. The SZ was sound in all three processing conditions which imply that the severe plastic deformation and material stirring created by FSP was able to diminish the porosity present in the PM. An Infra-Red technology-based thermal imaging camera (Fluke Ti400) was used for capturing the thermographic images to get an approximation of the peak temperature developed during FSP operation. During the whole experiment, the camera was set up at a fixed distance and angle from the operating region for getting accurate results Figure 4.9 represents the thermal imaging camera with its captured thermographic image of the processed zone. The approximate peak temperature developed was less than 500 ^{0}C (380-460 ^{0}C), which is very less than the melting point (T_m~650 ^{0}C) of the Mg alloy, not particularly of AS21A alloy. In other words, FSP produced the temperature in the range 0.7-0.9 T_m which confirmed the absence of parent alloy melting and thus it can be concluded that FSP is a hot working operation.

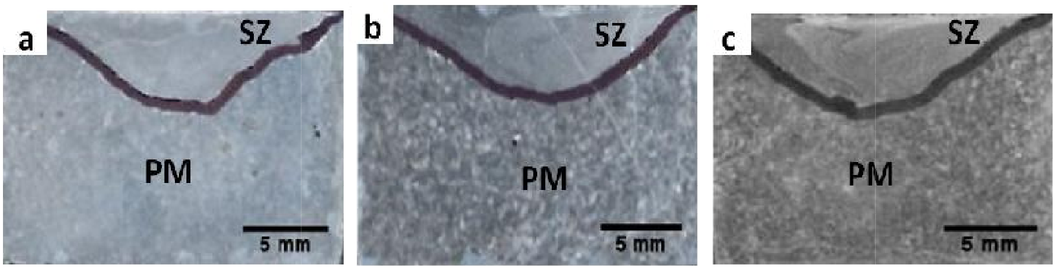

Figure 4.8 Macrograph of the FSP impression created in samples (a) F1, (b) F2 and (c) F3

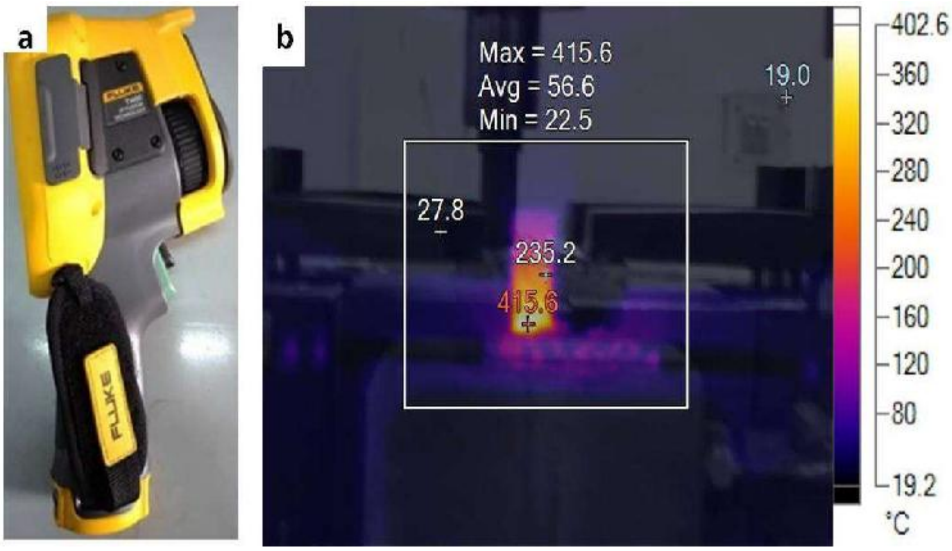

Figure 4.9 (a) Thermal imaging camera; (b) Thermographic image

Figure 4.10 exhibits the microstructures of the SZ (the centre region of the impression in Figure 4.8) developed in the processed samples. On comparing the OM image of parent and processed material, it can be inferred that size and shape of the Mg_2Si phase were modified after FSP. For all three samples, vigorous stirring and forging action produced by the FSP tool pin aided in the fragmentation of coarse eutectic Mg_2Si phase into fine particles and thus attaining their uniform dispersion in the matrix. The microstructure of the transition region shown in Figure 4.11 clearly distinguishes the processed and the unprocessed region. The fragmentation of Mg_2Si was further interpreted from SEM+EDS micrograph as shown in Figure 4.12. The present microstructure findings were in accordance with the investigation done by Zhang et al. [85] which states that the FSP of Mg-RE alloy resulted in the mechanical breaking of Al_2Ca intermetallic into fine particles. Arora et al. [86] concluded that FSP produced a homogeneous distribution of fine intermetallics (Al-RE) in the AE42 matrix. Santella et al. [147] and Ma et al. [148] observed uniform dispersion of second phase acicular silicon particles in the aluminium matrix during FSP of A319 and A356 castings. However, FSP of AZ91 and AZ31 alloys resulted in the complete dissolution of β-$Mg_{17}Al_{12}$ as observed by Wen et al. [81] and Feng et al. [82] respectively. It was attributed to the low MP of $Mg_{17}Al_{12}$ (460 ^{0}C). In the present work, frictional heat generated the temperature in the range 380-460 ^{0}C which was not enough for the dissolution of Mg_2Si due to its very high MP (1085 ^{0}C). More details of the FSPed cast AS21 A alloy are shown in Figure 4.13.

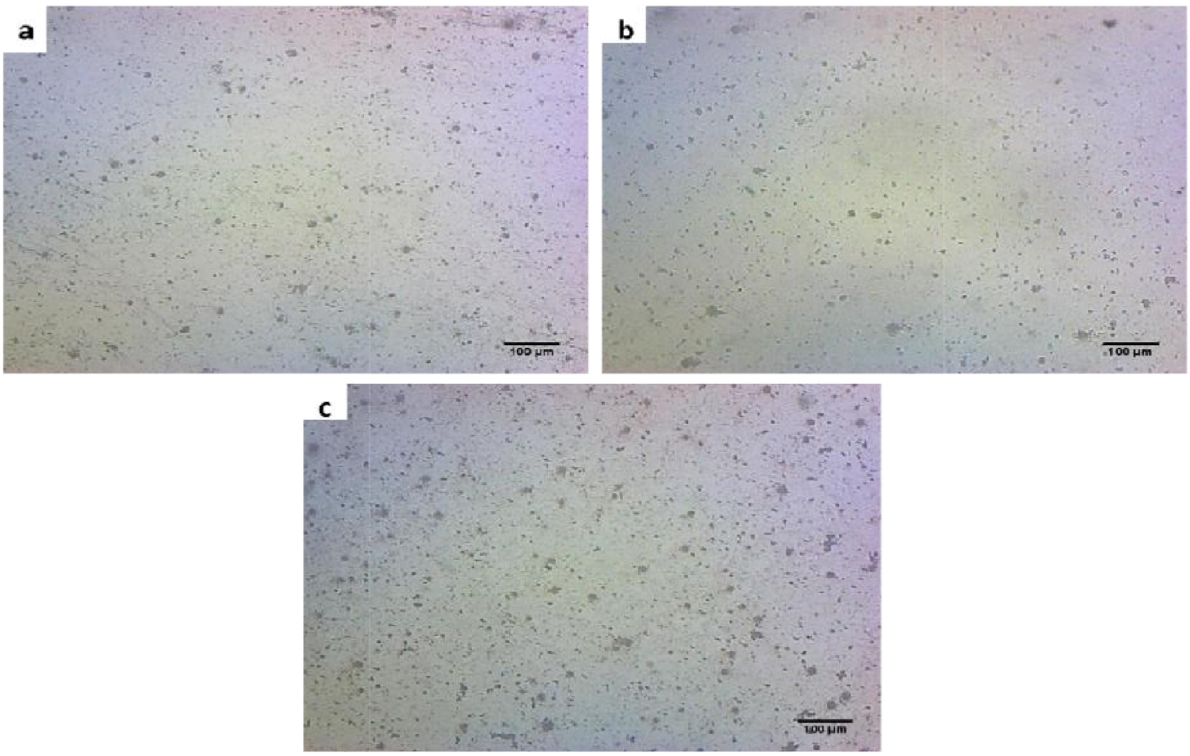

Figure 4.10 Microstructure of the processed samples: (a) F1, (b) F2 and (c) F3

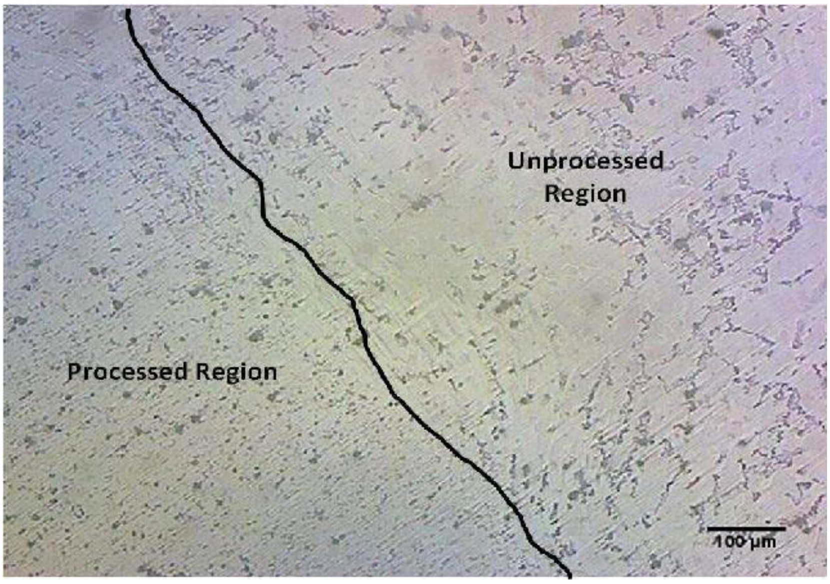

Figure 4.11 Microstructure of transition zone in the processed sample

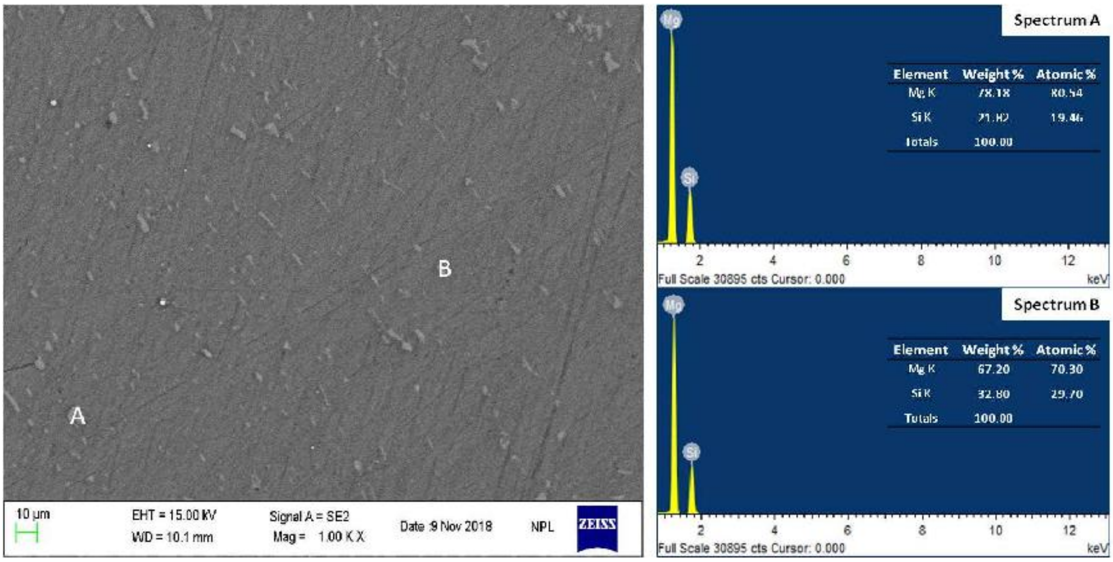

Figure 4.12 SEM with EDS spectrum of the processed sample

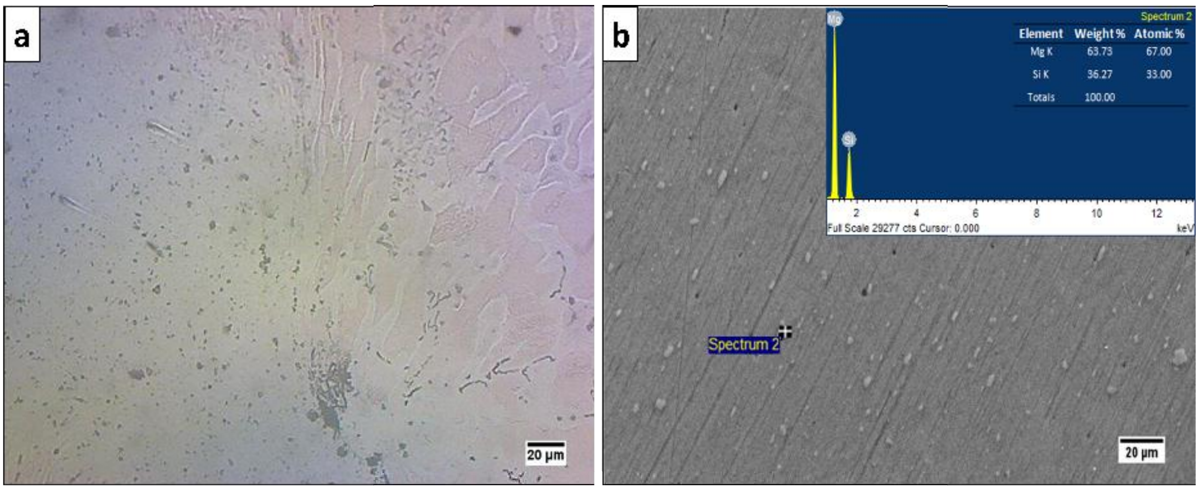

Figure 4.13 Microstructural features of the FSPed cast AS21A alloy at a different location

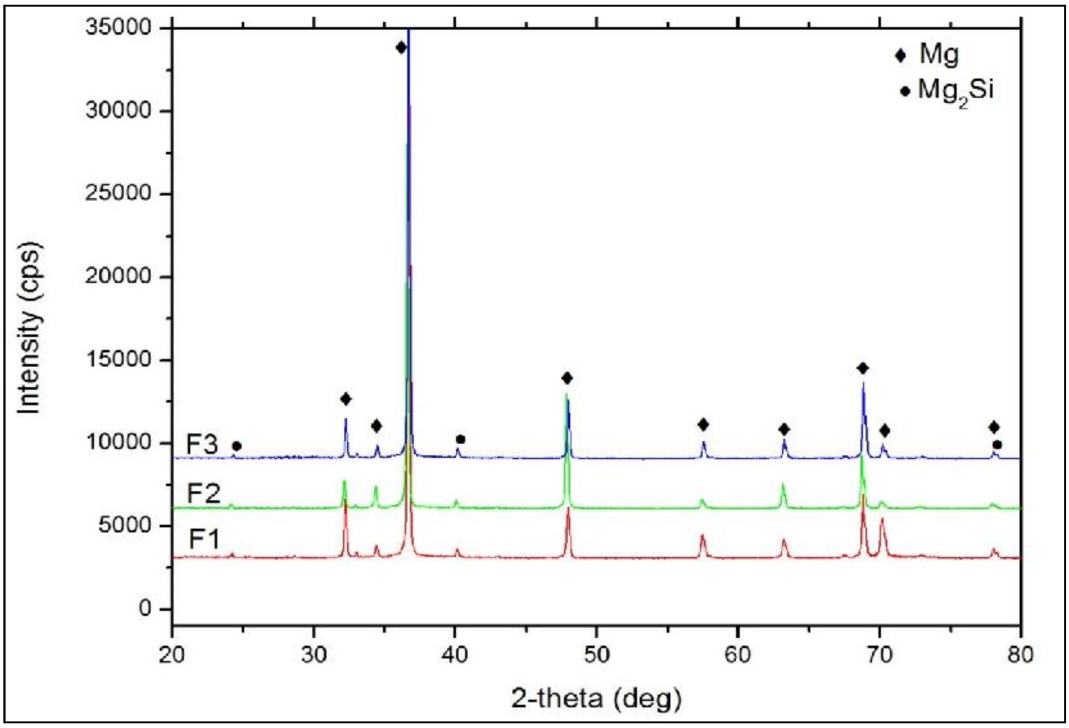

Figure 4.14 XRD pattern of the FSP samples

The fragmentation of Mg_2Si instead of dissolution was further confirmed by the XRD graph as shown in Figure 4.14. The graph indicates that FSP resulted in a decrease in the number and intensity of Mg_2Si peak when compared to the cast sample (Fig. 6) which confirmed the fragmentation of Mg_2Si into fine particles. Similarly, Cao et al. [98] performed FSP on Mg-Nd-Y alloy and attained the breakup of $Mg_{12}Nd$ and $Mg_{24}Y_5$ phases into tiny particles that were attributed to the reduction of diffraction peaks.

4.3 Mechanical Behaviour

The mechanical characteristics obtained from UTM and microhardness test are summarised in Table 4.11.

4.3.1 Microhardness Test

The average microhardness of the parent material was 55 HV which was only 20 % lower than the specimen processed at 800 rpm (F2). Microhardness variation of the processed samples along the width and depth of SZ is shown in Figure 4.15. The hardness profile clearly depicts that the FSP samples exhibited small fluctuation in the microhardness values. The large fluctuation in the PM hardness value can be attributed to the hard Mg_2Si and soft α-Mg networks (Figure 4.4) present in the magnesium matrix. Further, transformation of the coarse network into small particles due to FSP (Figure 4.10) contributed towards enhancing and homogenising the hardness in the SZ. Li et al. [101] reported a similar trend in respect of microhardness when FSP was performed on the WE43 magnesium alloy.

4.3.2 UTM test

The stress-strain curve presented in Figure 4.16 explains tensile behaviour of the cast and FSP treated (F1, F2, F3) specimens. The tensile test results exhibit that the FSP of cast AS21A alloy considerably improved its mechanical properties, especially ductility. The parent material exhibited a little elongation of 4 % while the sample processed at 800 rpm (F2) showed the highest elongation of 11%. The coarse and brittle Mg_2Si network attribute of cast AS21A alloy (shown in Figure 4.4) encouraged PM crack formation thus exhibiting the brittle characteristics. After FSP, the significant breakup of the coarse network into small particles (Figure 4.10) encouraged the precipitation strengthening, and there was a significant enhancement in the ductility for all specimens especially the specimen processed at 800 rpm. However, there was a marginal enhance in the strength of the samples. Moreover, the casting defects present in the PM were disappeared after FSP, which was also advantageous for the enhancement in ductility of FSP specimens. The high crosshead speed of 2.5 mm/min can be held responsible for the low strength of the alloy.

Table 4.11 Mechanical properties obtained from UTM and microhardness test

Specimen	Strength (MPa)	% Elongation	Average Microhardness (HV)
Parent Material	83.2	3.87	55
F1	91.8	6.72	62 *
F2	88.6	10.6	66 *
F3	91.5	7.95	61 *

***Stirred Zone**

The tensile fracture morphologies of the specimens are shown in Figure 4.17. The transverse fractured surface of cast AS21 alloy was characterised by the cleavage facets (point A in Figure 4.17a and 4.17b), wide craters (point B of Figure 4.17a) and cracks (point C of Figure 4.17b). These typical features indicate the brittle failure of the PM. During tensile deformation of the PM, crack formation was obvious due to the brittle nature of coarse Mg_2Si present at the grain boundary (Figure 4.4) thus exhibiting poor ductility. The FSP sample F1 and F3 transverse fractured surfaces were characterised by the limited and elongated dimples (point A in Figure 4.17d and 4.17h) thus exhibiting the mix ductile and brittle behaviour. Further, FSP sample F2 fractured surface was characterised by the fine and equiaxed dimples as shown in Figure 4.17f (point A). The superior ductile behaviour shown by the F2 sample justified the appearance of the fractured surface. Cao et al. [98] also discovered the second phase $Mg_{12}Nd$ as the main factor affecting the mechanical properties particularly ductility of Mg-Nd-Y alloy after FSP.

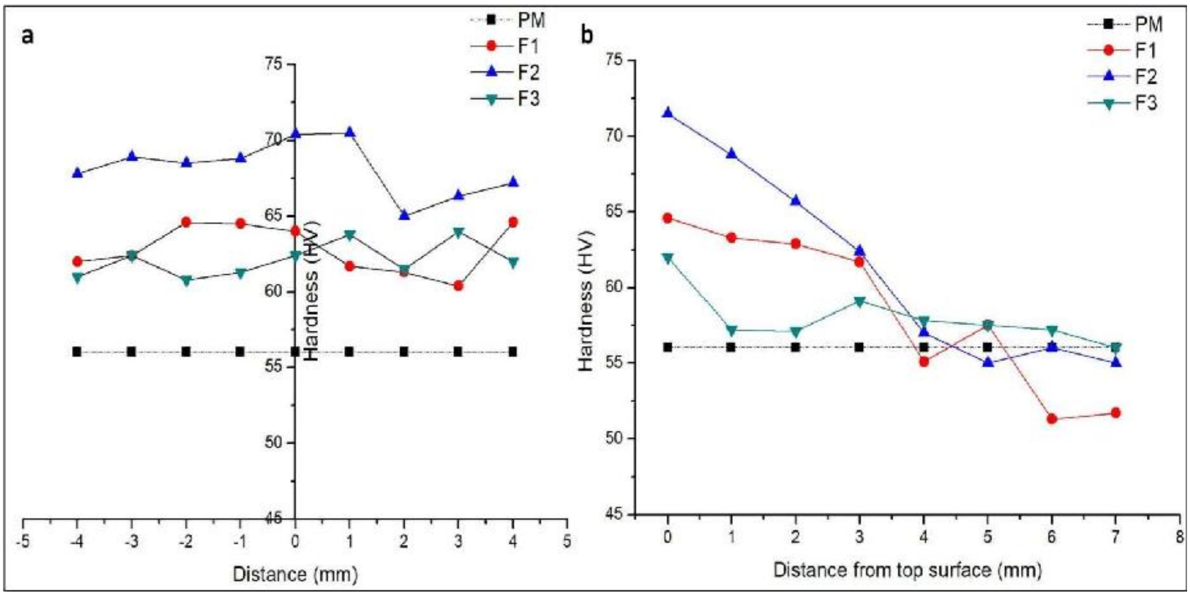

Figure 4.15 Microhardness variation along the (a) width of SZ and (b) depth of SZ

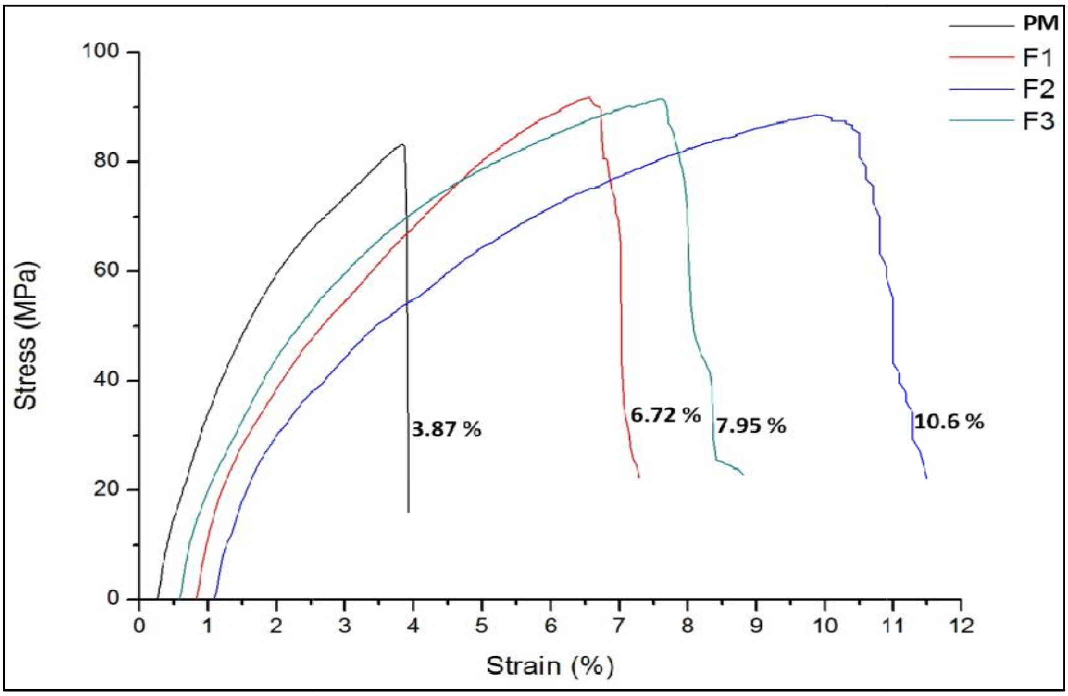

Figure 4.16 Tensile results obtained from UTM test

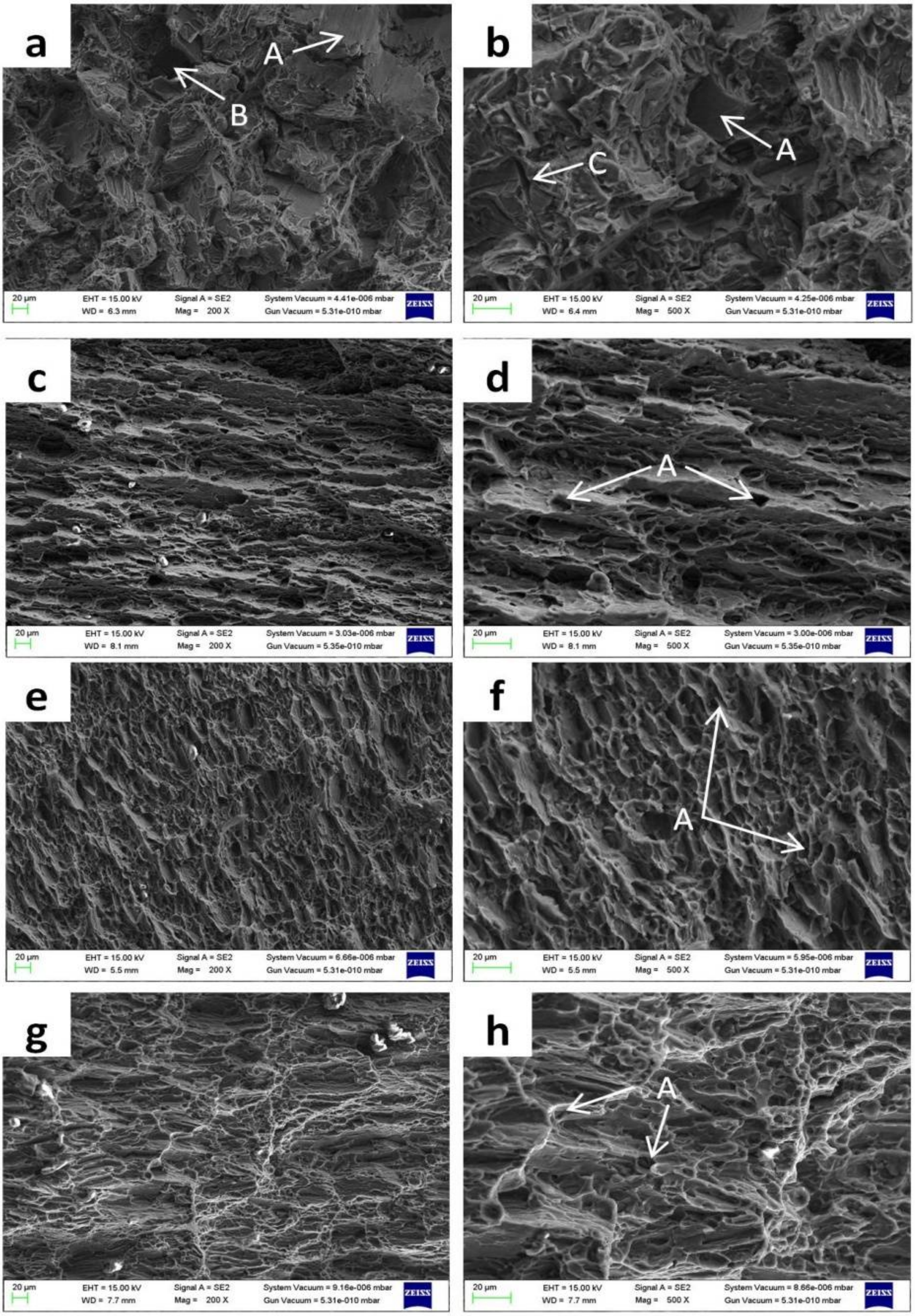

Figure 4.17 SEM micrographs of the fractured surfaces of (a,b) parent material; (c,d) F1; (e,f) F2; (g,h) F3 specimens

4.4 Wear Characterisation

In the subsequent investigation, the dry sliding wear characterisation of FSP treated cast AS21A alloy was performed on pin-on-disc apparatus. The objective was to examine the consequences of modified Mg_2Si morphology on the tribological performance of the cast AS21A alloy. In wear investigation, cylindrical pins of 8 mm diameter were wire-cut from the centre of the FSPed AS21A plate surface through wire cut as shown in Figure 4.18. Similarly, pin samples were also cut from the cast AS21A plate. The parameters employed during the wear investigation are presented in Table 4.12.

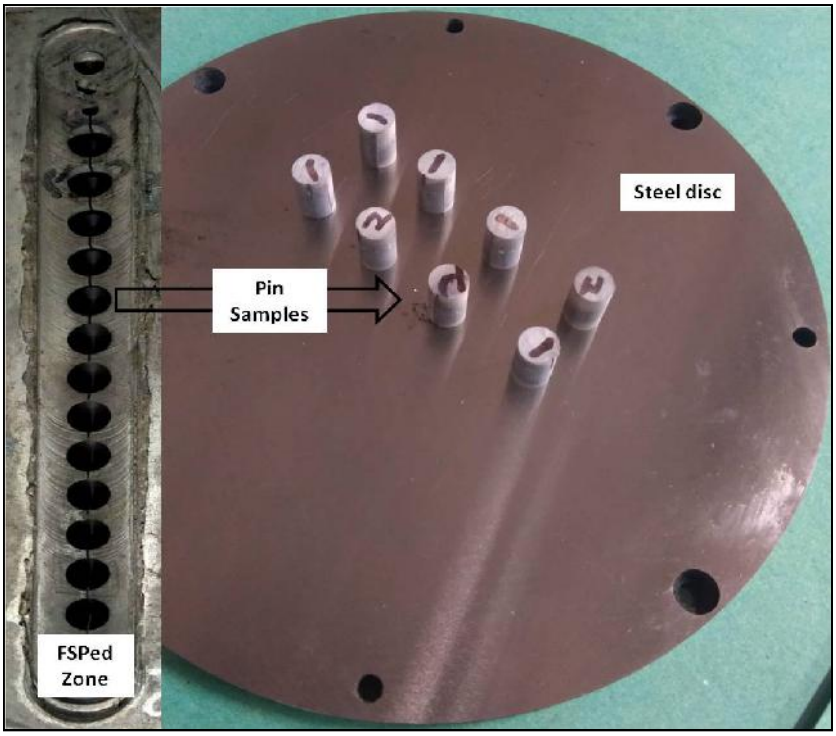

Figure 4.18 Pin samples and steel disc utilized during the wear test

Table 4.12 Pin-on-Disc Test Parameters

Parameters	Values
Normal load	10, 20, 30, 40 N
Sliding Speed	1 m/s
Sliding Distance	2500 m
Test Pin diameter	8 mm
Test Pin Ra value	0.30-0.74 µm
Counter Disc	EN24 steel hardened to 50-55 HRC
Counter Disc Ra value	0.12-0.22 µm
Counter disc diameter, height	165, 10 mm

4.4.1 Wear rate and Coefficient of Friction (COF)

The wear behaviour of cast AS21A alloy and FSPed AS21A alloy was investigated on Pin-on-Disc apparatus. All wear test results are summarised in Table 4.13, indicating wear loss, specific wear rate and Coefficient of Friction (COF). The weight loss measured before and after the wear of samples was used to determine the specific wear rate value.

Table 4.13 Wear characteristics obtained from Pin-on-Disc configuration

Load (N)	**Wear loss (mg)**		**Specific wear rate (10^{-4} mm^3/Nm)**		**Coefficient of Friction (COF)**	
	Cast AS21A sample	FSPed sample	Cast AS21A sample	FSPed sample	Cast AS21A sample	FSPed sample
10	34.2	26.2	7.82	5.99	0.32	0.31
20	49.2	40.9	5.62	4.67	0.29	0.26
30	66	57.5	5.03	4.38	0.24	0.23
40	99.4	86.3	5.68	4.93	0.15	0.14

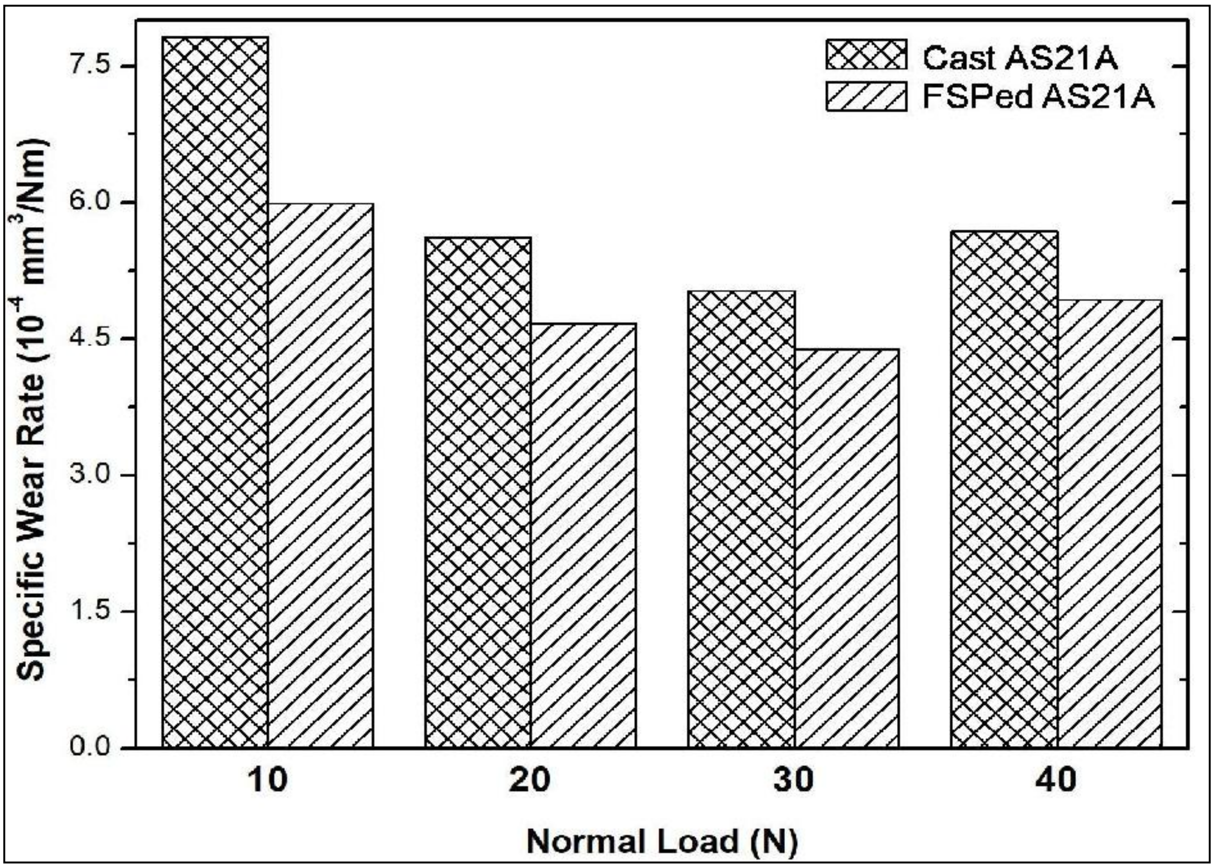

Figure 4.19 Specific Wear Rate plot for both conditions of AS21A alloy

The Specific wear rate plot against different load levels for cast and FSPed AS21A alloy is depicted in Figure 4.19. It is evident from the test results that the FSPed specimen has consistently exhibited superior wear resistance throughout the range of parameters investigated. Additionally, the increasing trend of wear rate with increase in the normal load was found in both cast and FSPed samples.

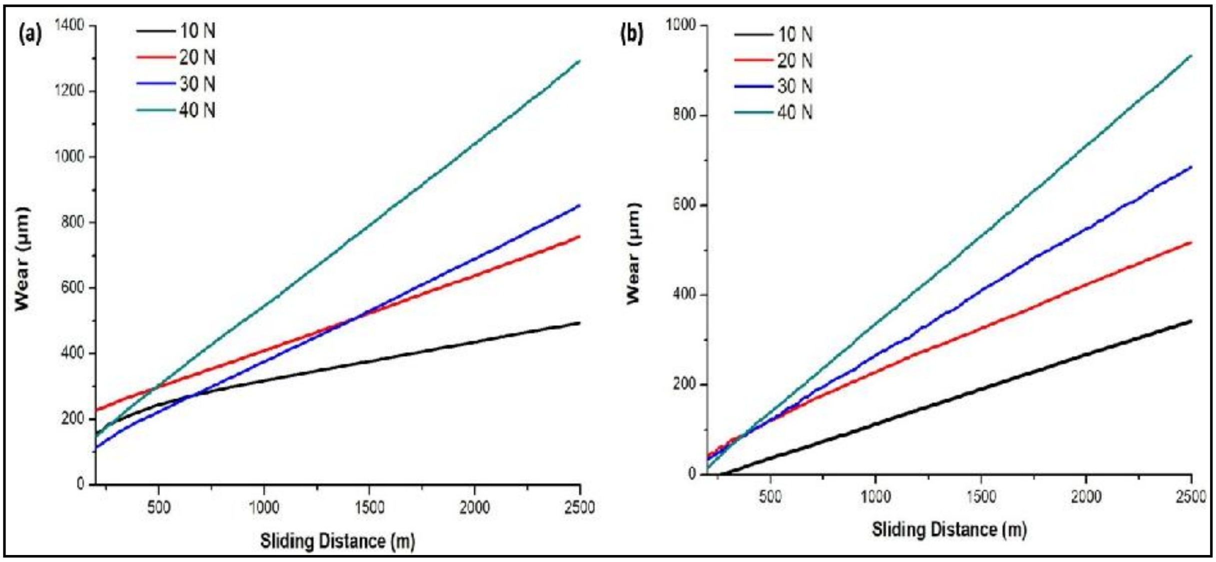

Figure 4.20 Wear loss measured from Pin-on-Disc wear sensor in (a) cast and (b) FSPed AS21A samples

In addition to this, wear loss (μm) measured through the wear sensor is plotted against sliding distance for all load conditions, as depicted in Figure 4.20. The plot indicates the increase in wear loss with an increase in Normal load. FSP of AS21A has a marginal effect on COF value, as shown in Table 4.13. However, FSP resulted in less COF fluctuation compared to base alloy, as shown in Figure 4.21 at all load levels. Also, the COF value was found to be reducing with the increase in load for both cast and FSPed samples.

4.4.2 Worn Surfaces

The worn out surfaces of wear samples were examined by means of SEM and EDS, as shown in Figure 4.22 and Table 4.14. The prominent mechanisms responsible for the wear of worn surfaces were abrasion, adhesion, delamination, oxidation and plastic deformation. The deep and narrow ploughing traces running parallel to the sliding direction on all samples validated the wear due to abrasion mode. Further, fractured surfaces and micro-cutting appeared prominently at higher load indicated the abrasion wear in the samples. The signs of metal flow and the presence of wear debris on the worn surfaces, particularly at lower load value, easily described the adhesion wear mode. The worn surfaces of cast samples tested at a higher load value of 30 and 40 N exhibit signs of material removal in the form of platelets which established the wear due to delamination. Magnesium alloys are easily prone to get oxidised; therefore, the oxidation mechanism also plays an essential role in wear of samples. The oxidation mechanism in wear samples was validated by the EDS analysis as shown in Table 6 which depicts that an oxide layer accompanies the worn surfaces. The evidence of lip formation and the extruded layers of material in the case of the FSPed sample, particularly at higher loads indicate the signs of plastic deformation.

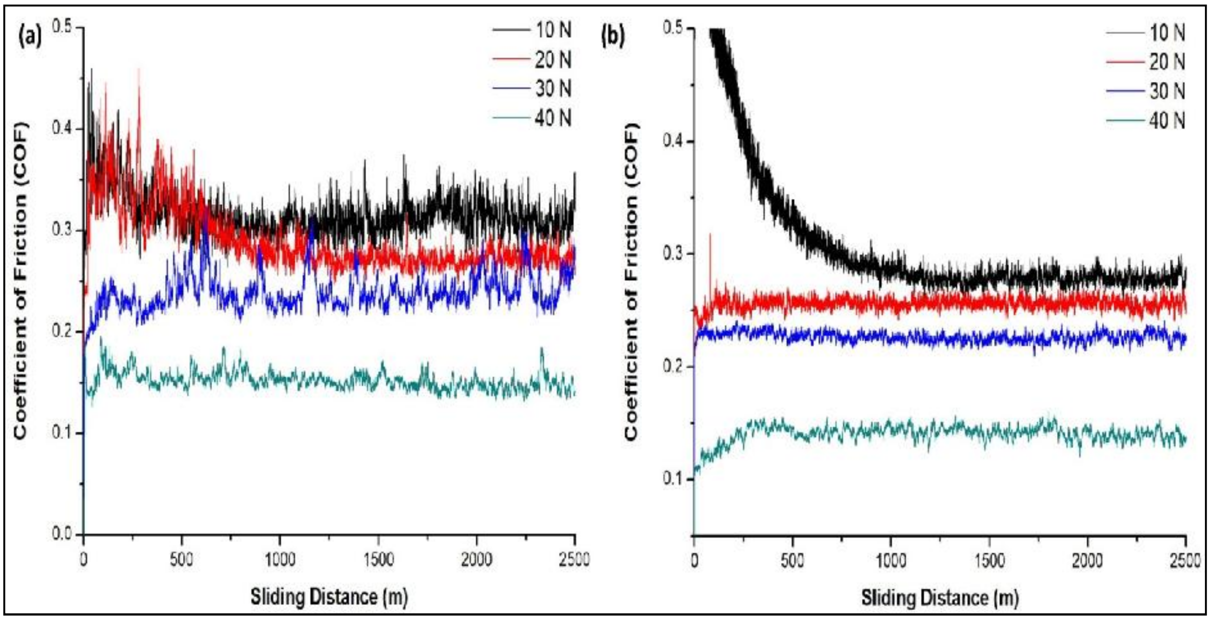

Figure 4.21 Coefficient of Friction (COF) graph for (a) cast and (b) FSPed AS21A samples under different load conditions

4.4.3 Wear Discussion

In the present study of AS21A magnesium alloy, the active relation between Wear and microstructural characteristics was observed. The extent of wear specified by the specific wear rate in the case of FSPed AS21A samples was found to be lower as compared to the cast AS21A samples. The features, size and distribution of the Mg_2Si eutectic phase played a crucial part in the wear characteristic of AS21A magnesium alloy. The presence of coarse and irregular Mg_2Si precipitates in the cast AS21A sample may lead to the stress concentration at the interface of α-Mg/Mg_2Si, thus providing an easy path for crack nucleation increasing wear. On the other hand, fine in-situ Mg_2Si precipitates obtained after FSP treatment would retard the growth of the crack in the case of the processed sample, thus reducing its wear. Also, the reduction of pores and cavities due to FSP contributed to enhancing the wear resistance of the AS21A alloy. The cavities present in the cast samples reduce the contact area between the wear sample and its counterpart during the wear test which increases the actual pressure on the surface of the sample and hence decreasing the wear resistance of cast AS21A samples. Alidokht et al. [91] and Reddy et al. [90] advocate similar wear characteristics in the case of FSP treated aluminium alloy. It was reported that the microstructural features obtained after FSP of Al alloys such as uniform distribution of coarse Si particles and porosity closure significantly improved the wear resistance of A356 Al alloy. Akyuz et al. [79] observed that the Mg_2Si intermetallic assisted in improving the wear behaviour of AS91 alloy in contrary to the $Mg_{17}Al_{12}$ phase. Apart from the microstructural features, the high hardness value exhibited by the FSPed sample also contributed to enhancing the wear resistance of AS21A alloy, which is in good agreement with the Archard equation [149]. Archard predicted that the wear resistance of any material depends on its hardness; the relation between microstructure and hardness was ignored.

Wear loss was found to be increased drastically with the application of higher load for both conditions of AS21A magnesium alloy: cast and FSPed. The following acquired result validates the Archard [150] argument who concluded that the wear rate is directly related to the normal load. Higher load assisted in increase in the no. of contact asperities between the mating surfaces resulting in more wear debris. Further, an appreciable amount of plastic deformation due to the high ductility of magnesium alloy can also be attributed to the increased wear rate at higher loads [97]. The higher value of normal load during the wear test resulted in a small Coefficient of Friction (COF) value for both conditions of AS21A samples. The decrease of COF with load might be ascribed to the thermal softening of the samples leading to high temperatures generation at the surfaces. In addition to this, a higher COF value at lower load can also be attributed to the abrasion of wear samples by debris particles since particles were not in a position to get out from the interacting surfaces at lower loads. Previous investigations [151, 152] also reported that samples having lower COF exhibited high wear resistance. The initial increase in COF value as depicted from Figure 4.21 particularly at smaller loads can be attributed to the increase in friction force required to prevail over the extreme adhesive contact between pin and its counterpart [57]. There was not much difference observed in the COF value of cast and FSPed samples since FSPed surfaces were subjected to a considerable amount of localised plastic deformation because of their superior ductility [89]. The COF fluctuations in the case of FSPed samples were observed to be lower compared to the cast AS21A samples as depicted from Figure 4.21. The fine in-situ precipitates of Mg_2Si obtained after FSP acted as a capable load bearing candidate, thus decreasing the COF fluctuations in the case of FSPed samples. Alidkoht et al. [91] also attributed the lower COF fluctuations to the fine Si particles obtained after FSP of A356 aluminium alloys.

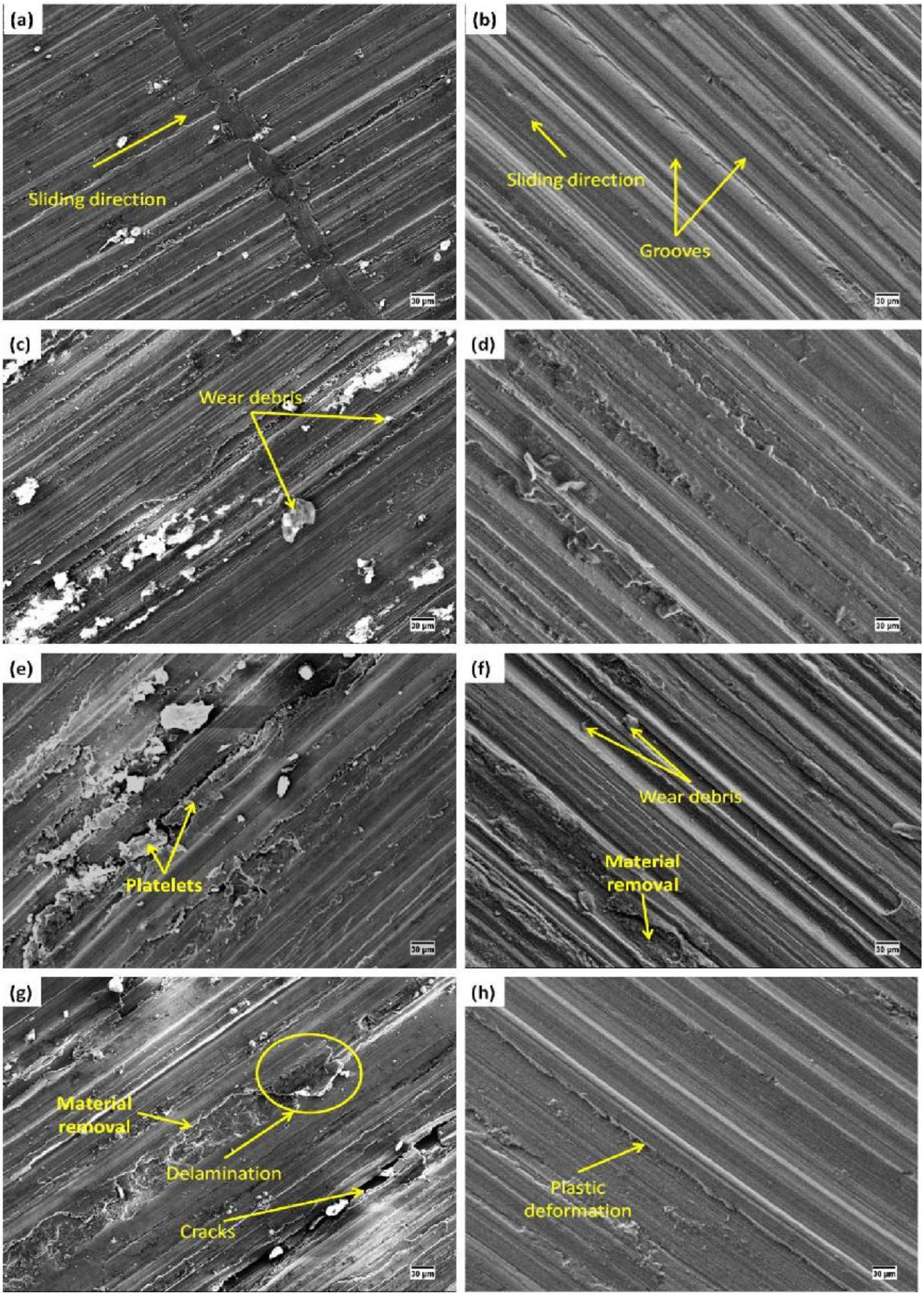

Figure 4.22 SEM micrographs showing worn surfaces of the cast and FSPed AS21A samples tested at 10 N (a, b); 20 N (c, d); 30 N (e, f) and 40 N (g, h)

The abrasion mode was confirmed by the worn samples surface features such as groove and ridges impressions running parallel to the sliding direction. The presence of hard asperities on steel counterface or detached particles amid interacting surfaces assisted in deformation and microploughing of the soft matrix, thus causing the removal of material through abrasion mode. The extensive surface damage occurred at a higher load due to the appreciable amount of material removal obtained in the form of platelets, thus exhibiting the delamination mode of the wear mechanism. As the rate of delamination depends on the crack nucleation, therefore cast AS21A wear samples were subjected to severe delamination as compared to FSPed samples. In FSPed samples, fine in-situ Mg_2Si precipitates faded the delamination effect resulting in more wear resistance. In a similar finding, Mahmoud et al. [87] recognised fine Si particulates as the primary phenomenon for the enhanced wear resistance in FSPed cast A413 alloys. The considerable amount of ductility obtained after the FSP of AS21A alloy contributed to the plastic deformation of the FSPed wear sample, particularly at higher load. Arora et al. [92] also reported that the FSPed AE42 wear samples were more plastically deformed in contrary to as-cast alloy. Another important mechanism involved in the wear of the studied alloy was oxidation wear which is distinguished by oxide layer formation on the worn surfaces. The oxidation mode is a common mechanism encountered in magnesium alloys since Mg alloys tend to get oxidised as samples were continuously exposed to an oxidising atmosphere during testing [153]. The decrease in the amount of oxidation with the normal load as depicted from the EDS spectrum in Table 6 can be attributed to fracture of the oxide layer at higher load values which is per Arora et al. [92] and Zahmatkesh et al. [88] results.

Table 4.14 EDS spectrum of worn surfaces of FSPed samples

Load	SEM micrograph of the worn surface	EDS analysis of worn surface
10 N	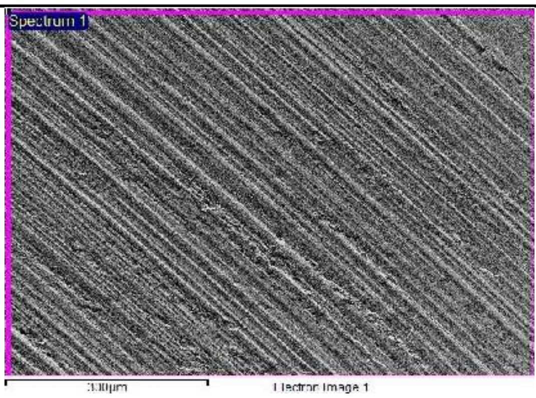	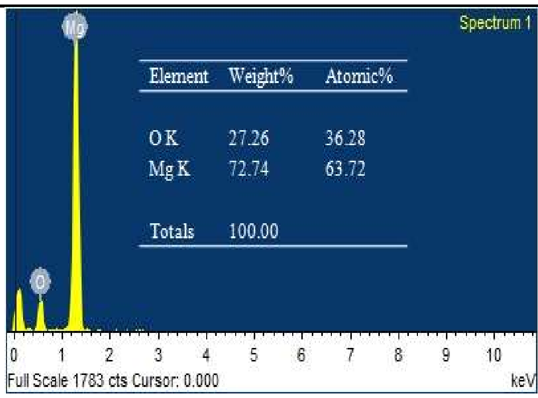
20 N	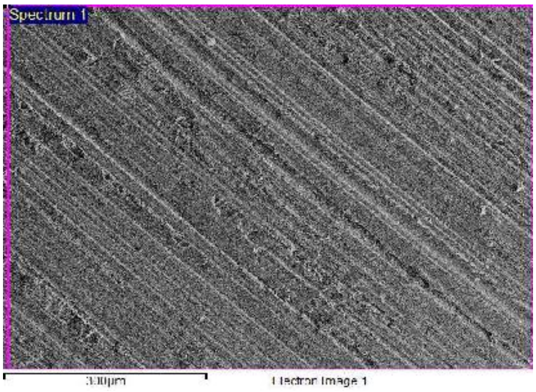	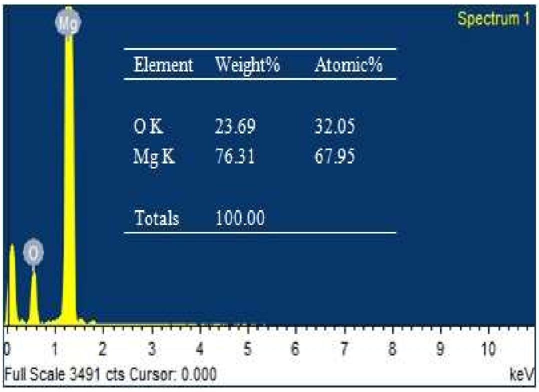
30 N	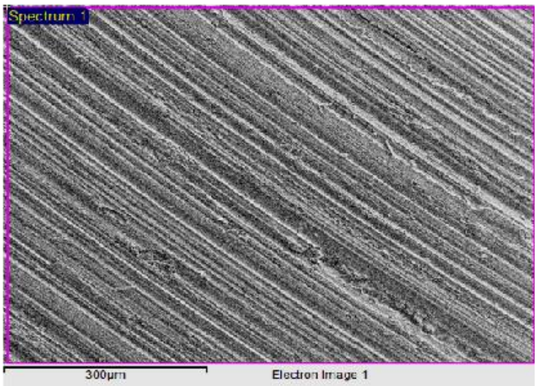	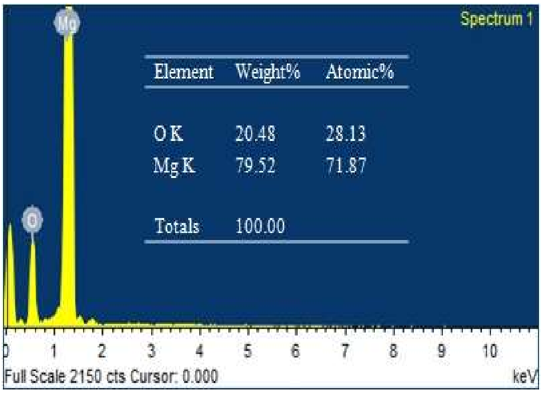
40 N	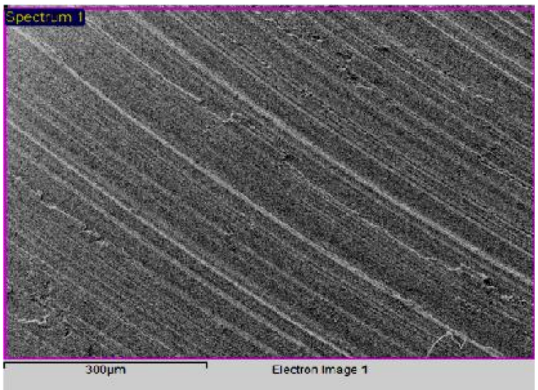	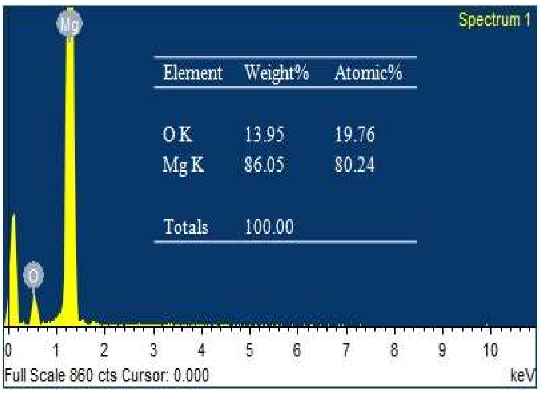

4.5 Fabrication of sector shape pad

The significant amount of ductility and the analogous microstructure of the investigated material gave a novel idea to develop a sector shape pad material. In sector shape pad, Babbitt or white metal is used as a bearing material surface with steel base. The pad is loosely constrained so it is free to pivot. Sector shape pads are employed in thrust bearings to support the heavy-duty axial load. Thrust bearing consists of series of such metallic pads arranged around a rotating collar fixed to the shaft. Figure 4.23 shows the Kingsbury hydrodynamic thrust bearing and its anatomy. Babbitt alloys are the best choice for the bearing materials due to their ability to embed foreign particles which can be attributed to their softness. Further, they have the unique feature to adapt to any type of misalignment during operation.

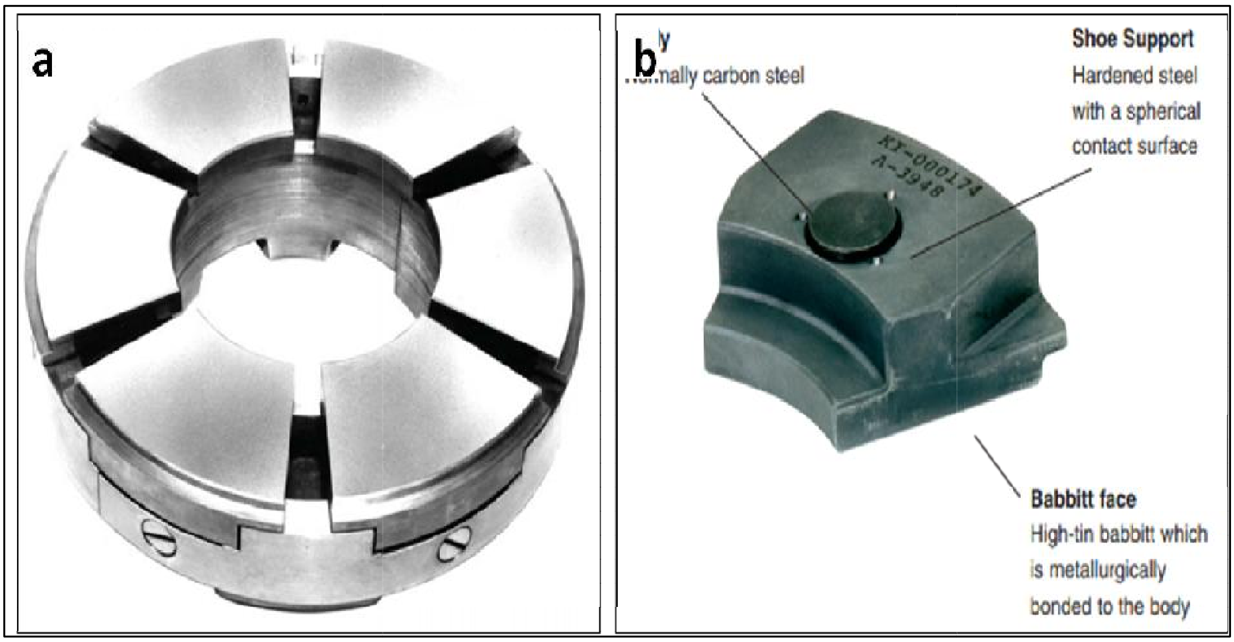

Figure 4.23 (a) Hydrodynamic, Equalizing Pivoted Shoe Thrust Bearing; (b) Pivoted shoe anatomy (Source: Kingsbury, Inc)

For the present study, one of the sector shape pads of thrust bearing was procured from the Chambal fertiliser and chemicals limited, Kota. A tilting pad thrust bearing attached to the steam turbine machinery is used to support thrust loads. Almost 90 % of axial load is balanced by the balancing drum and the remaining load is transmitted to thrust bearings. Figure 4.24a shows the actual machinery where the thrust bearing is employed and Figure 4.24b shows the actual tilting pad thrust bearing (Mfd: Siemens). The turbine machinery is the part of 1175×2 MTPD Urea plant in Chambal fertiliser. The thrust bearing is double-acting having a total area of 7480 mm^2 and is designed for the allowable thrust load of 8.6 MPa.

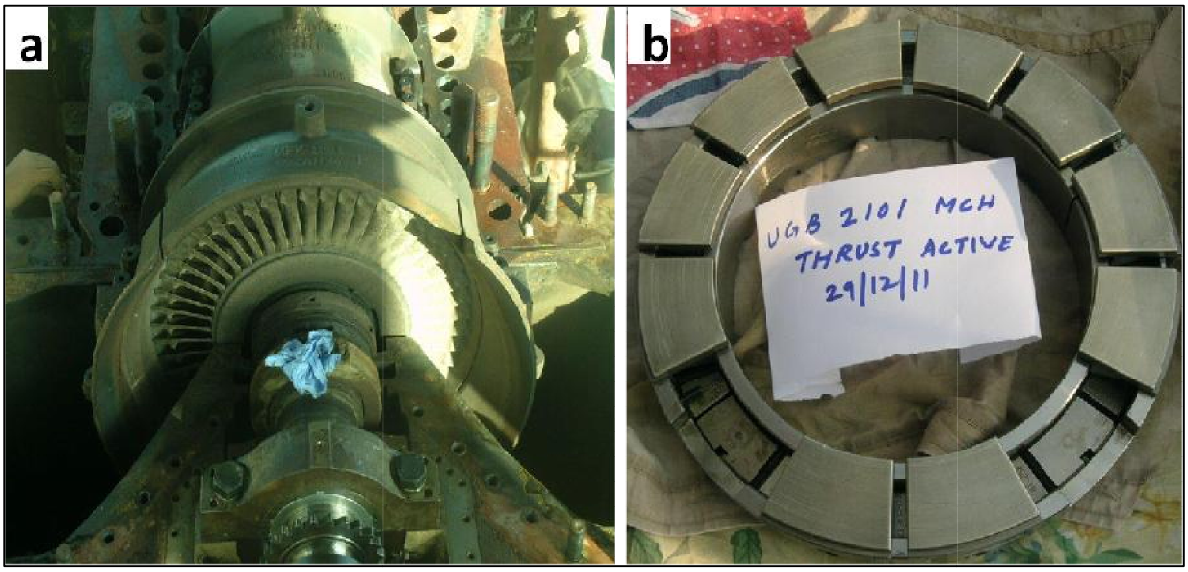

Figure 4.24 (a) Actual steam turbine machinery; (b) Thrust bearing

4.5.1 Microstructural characterization of the pad material

The procured sector shape pad was further characterized for microstructure, microhardness and wear. For this, specimens were taken from the pad surface through wire-cut as shown in Figure 4.25.

Figure 4.25 Samples cut from the pad for characterization

It was revealed from the microstructural analysis that the thrust pad is having a tin-based babbitt alloy coating with the backing of steel. Tin based babbitt alloy microstructural features consists of a soft and solid matrix of Sn in which hard Cu_6Sn_5 needles and Sn-Sb cuboids are dispersed as shown by the optical micrograph shown in Figure 4.26a. The presence of intermetallics was confirmed by the XRD pattern as shown in Figure 4.26b.

These intermetallics enhance the load-bearing capacity and the strength of the pad material. The present investigated material, i.e. FSPed cast AS21A alloy, is also having an analogous structure with that of Babbitt alloy since it contains fine intermetallics of Mg_2Si dispersed in the solid matrix of magnesium. This microstructural analogy gave a novel idea to investigate the magnesium alloy for thrust bearing applications.

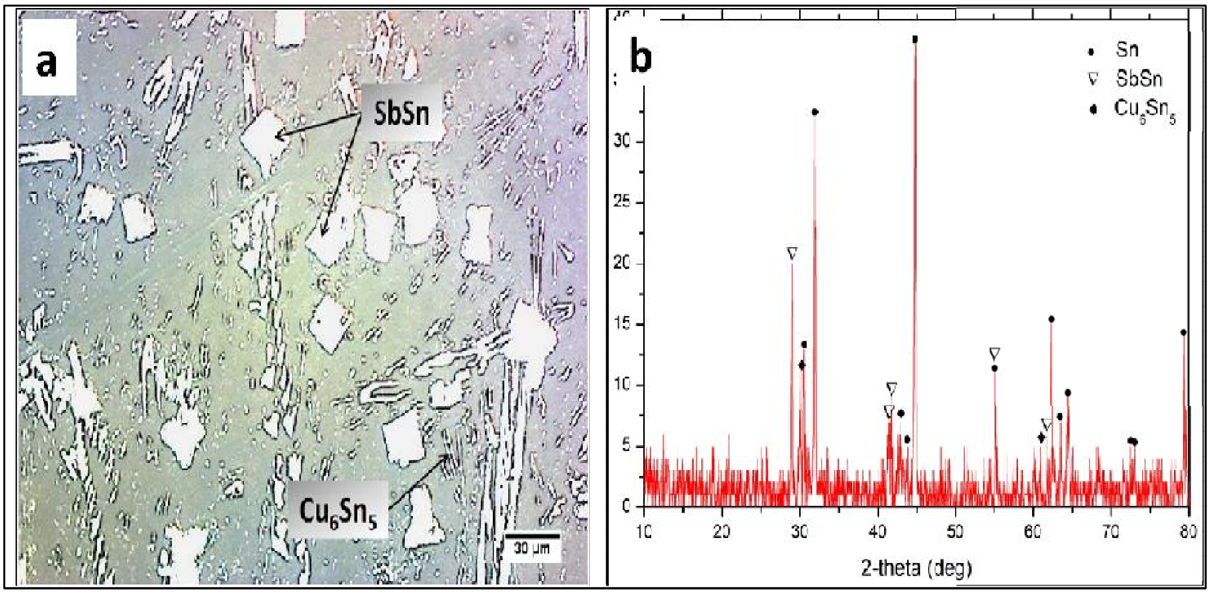

Figure 4.26 (a) OM image of the pad material; (b) XRD pattern

In further investigation, the microhardness value of the pad material was found to be in the range of 20-30 HV with a mean value of around 23 HV. The pattern of hardness, shown in Figure 4.27, was obtained by the indentation of the pad surface at various locations. The indentation mark can be observed in the micrograph as shown by Figure 4.28. The low microhardness value of the material can be attributed to its softness, which makes them suitable for bearing applications.

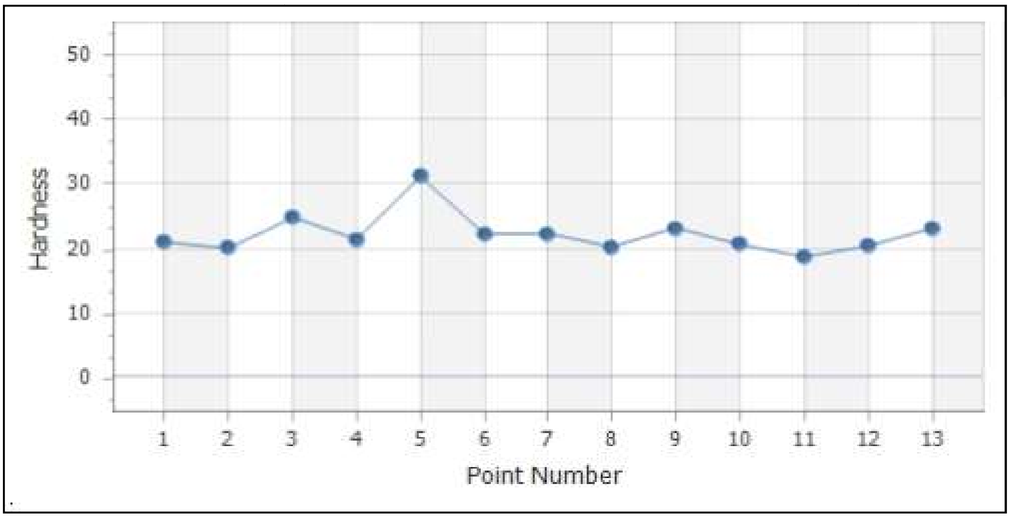

Figure 4.27 Hardness profile of the pad material

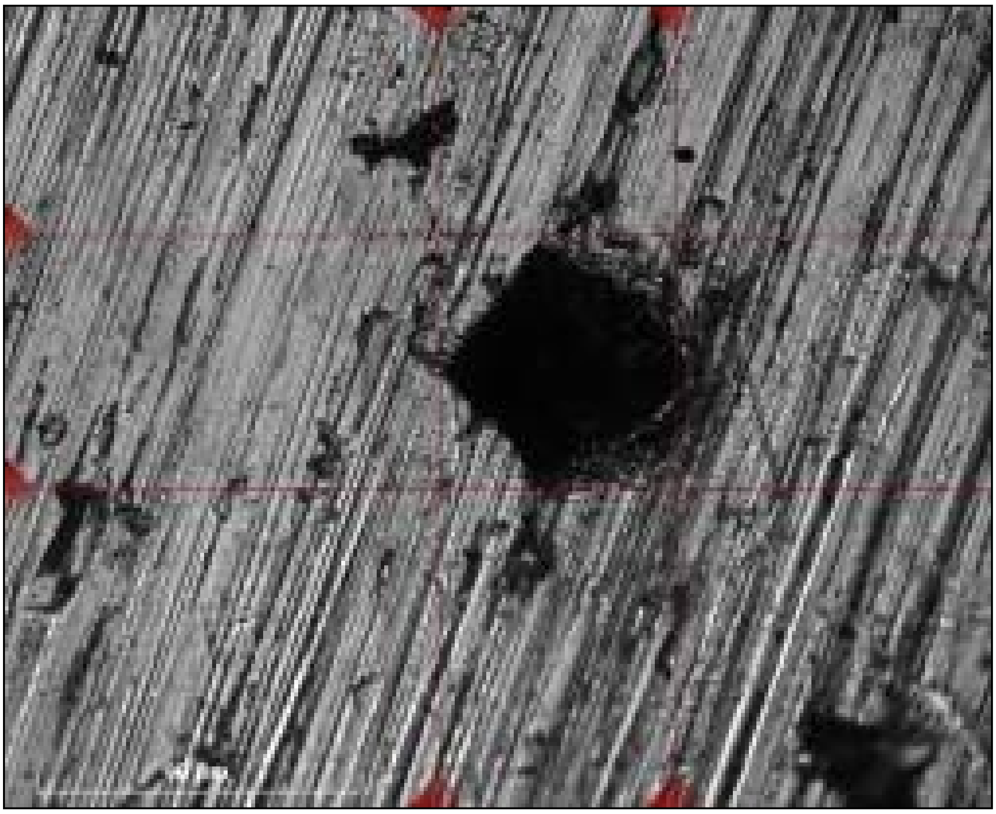

Figure 4.28 OM image showing indentation mark on the pad surface

4.5.2 Wear characterization of pad material

The pad material of Babbitt alloy was further studied for the wet wear analysis at different pressure values. The commercially available SAE 15W40 lubricating oil (mfd: Shell) was employed for the wet analysis. In power generating machinery, thrust loads provide average bearing pressure of 2-5 MPa [154]. Therefore, in the present study wet analysis was carried out at the pressure values of 1.98, 2.58, 3.18 and 3.78 MPa. Apart from this, other parameters which were set during the wear test are the sliding distance of 1000 metres and sliding velocity of 1 m/s. Similarly, wet wear analysis was also performed on the FSPed cast AS21A alloy for comparison purposes. The detailed wear findings are shown in Table 4.15. It can be observed that there is not much difference in the specific wear rate and coefficient of friction values for both types of samples. Furthermore, little amount of wear was detected which can be attributed to the lubrication between the tribo pairs. Figure 4.29 shows the COF variation with the sliding distance.

Table 4.15 Wet wear results

Pressure (MPa)	Wear loss (mg)		Specific wear rate (10^{-6} mm^3/Nm)		Coefficient of Friction (COF)	
	Pad material	FSPed AS21A alloy	Pad material	FSPed AS21A alloy	Pad material	FSPed AS21A alloy
1.98	0.2	0.2	1.200	1.143	0.012	0.015
2.58	0.5	0.3	0.894	1.319	0.011	0.009
3.18	0.7	0.5	0.574	1.786	0.009	0.011
3.78	0.9	0.6	0.612	1.805	0.013	0.014

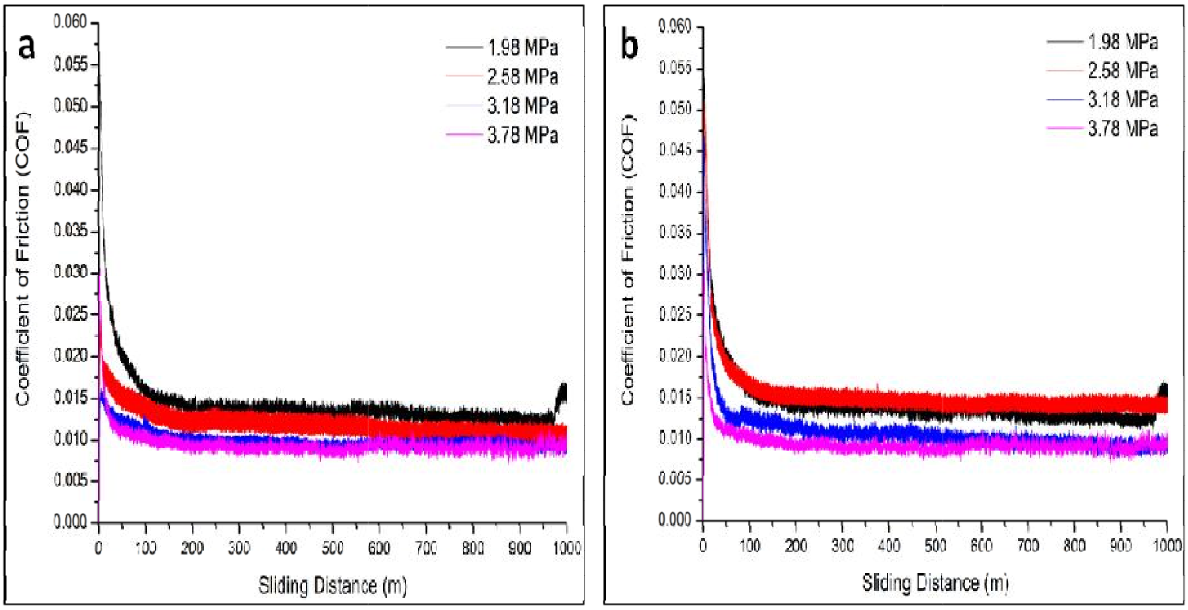

Figure 4.29 Coefficient of Friction (COF) graphs for (a) pad samples and (b) FSPed AS21A samples under different pressure values

4.5.3 Fabrication of pad

It can be inferred from the characterization studies that the present work material is comparable with the Babbitt alloy in terms of microstructure, microhardness and wear. Therefore, the thrust bearing pad of FSPed AS21A alloy was fabricated on the steel backing. In the FSP technique, a narrow processed zone is obtained which is not appropriate for practical applications. The extension of FSP to multiple pass FSP addresses this issue, whereby a certain level of overlap between successive passes can be utilized to fabricate a wider processed zone. As per the literature [94] 50 % overlapping provide the best result in the multi-pass FSP approach. Here 50 % overlapping means overlapping of the processed zone. It is well established [94] that the size and distribution of intermetallics or precipitates is not affected by overlapping FSP. The precipitates broken by FSP were found to be homogeneously dispersed in the whole processed zone fabricated via multiple pass FSP.

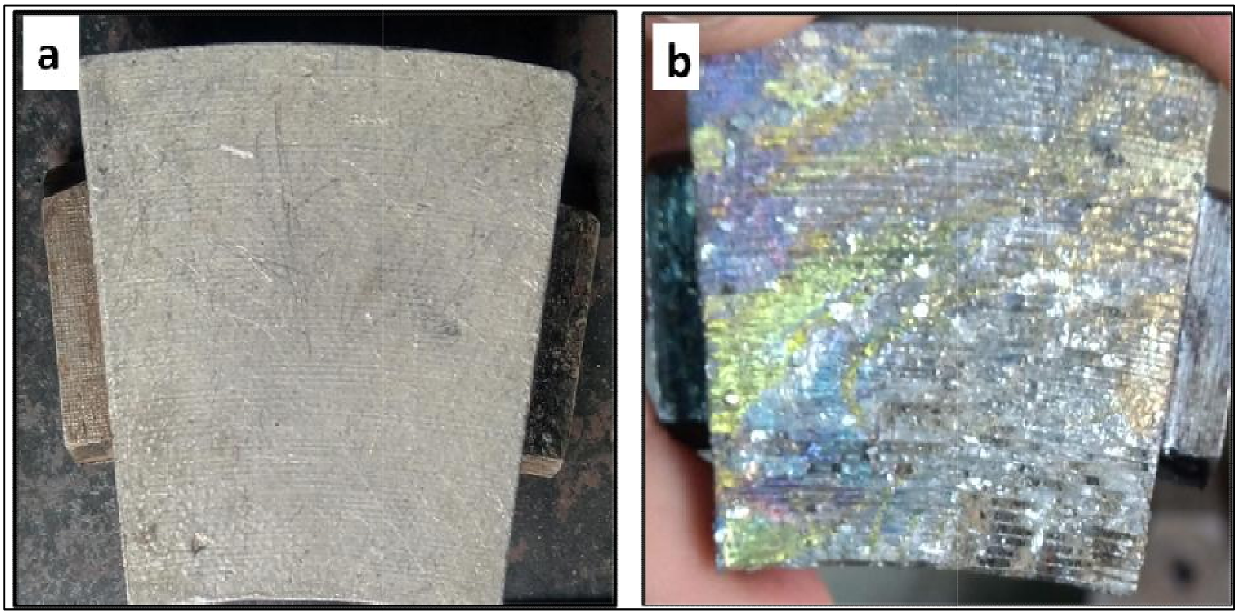

Figure 4.30 (a) Procured sector shape pad (b) Surface appearance of the pad after removing the Babbitt coating

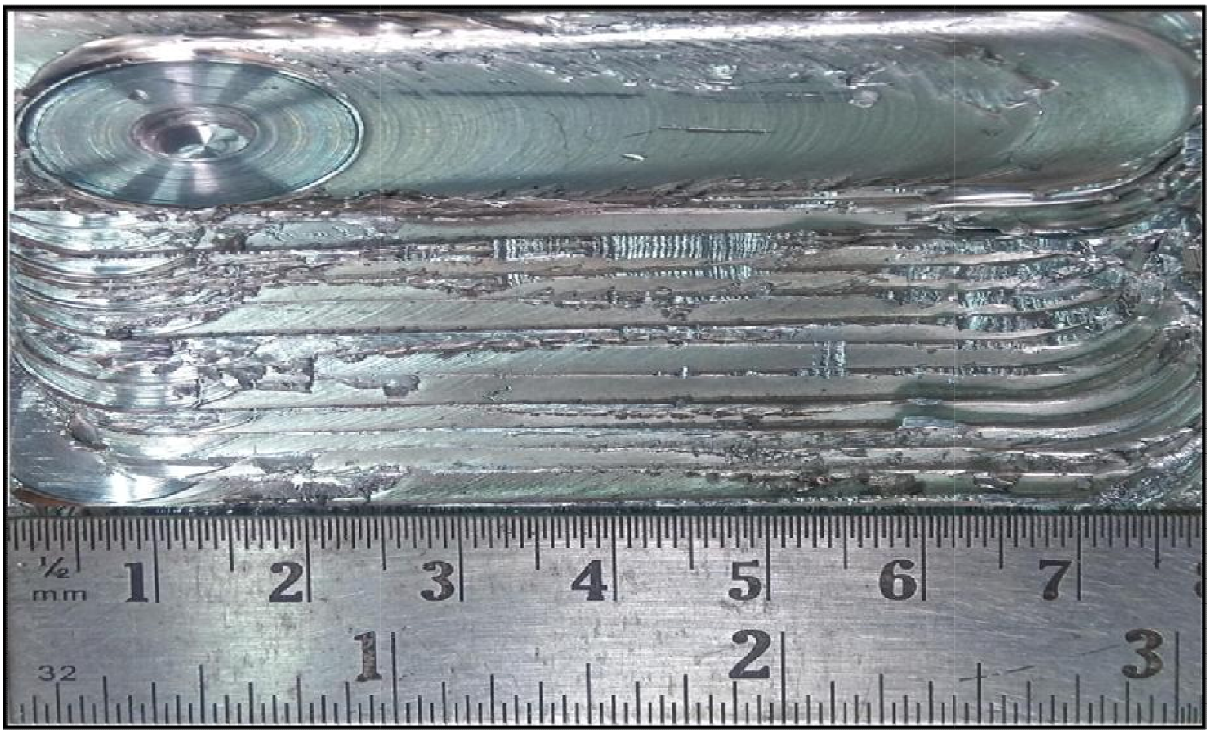

Figure 4.31 Processed zone of cast AS21A alloy achieved through multi-pass FSP

Therefore in the present work, multiple pass FSP of cast AS21A alloy was performed at an optimised set of parameters. The sector shape pad of the investigated material was fabricated in three stages. Firstly, the babbitt layer was melted from the procured pad by a gas welding flame as depicted in Figure 4.30. In the next stage of fabrication, a multi-pass FSP strategy with 50 % overlap was utilised for fabrication of sector shape pad which leads to 12 pass FSP to achieve a wider processed zone as shown in Figure 4.31. Finally, the material was cut from the processed zone as per the shape and size of the thrust pad and fabricated on the base using adhesive as shown in Figure 4.32.

Figure 4.32 (a) Pad shape piece cut from the processed zone (b) Fabricated FSPed cast AS21A alloy sector shape pad

CHAPTER 5

CONCLUSIONS AND FUTURE SCOPE

5.1 Conclusions

The heat-resistant Mg-Al-Si based AS21A magnesium alloy selected as parent material was employed for the current study. The AS21A alloy microstructural features were characterized by the α-Mg grains surrounded by coarse and brittle Mg_2Si Chinese script networks at the grain boundaries. In the present work, Friction Stir Processing (FSP) was performed on the cast AS21A alloy at an optimized set of process parameters followed by its microstructural, mechanical and tribological characterization. The hybrid optimisation approach of Taguchi-Grey Relational Analysis-Principal Component Analysis was employed to identify the optimum level of process parameters to perform the FSP operation. The optimisation experiments were conducted according to L9 Taguchi design array. Additionally, a sector shape pad was prepared from the FSPed AS21A alloy. Following were the major conclusions during the entire experiment:

1. The hybrid Taguchi-GRA-PCA approach successfully optimized the FSP of cast AS21A alloy. The optimal level of process parameters was selected based on largest GRG value and was found to be: Rotational Speed of 800 rpm, Travel Speed of 50 mm/min and Shoulder Diameter of 20 mm. ANOVA results exhibited significant process parameters as rotational speed (71.27 %) followed by the shoulder diameter (13.99 %) and travel speed (11.44 %). Furthermore, a confirmation experiment shows the improvement in GRG value by 0.0374.

2. FSP technique was able to modify the Chinese script morphology of Mg_2Si intermetallics through its fragmentation into the fine particles in the magnesium matrix, and almost eliminated all the defects present in the parent material. FSP generated the temperature in the range of 380 °C–460 °C which was not sufficient for the dissolution of Mg_2Si in the Mg matrix.

3. The microstructural modifications attained through FSP significantly improved the mechanical properties of AS21A alloy, especially ductility. The specimen processed at 800 rpm exhibited the highest degree of elongation (11%) compared to the parent

material (4 %). The fractography results exhibited the brittle and ductile characteristics of the parent material and the processed material respectively.

4. The FSPed samples exhibited better wear resistance compared to cast AS21A samples at all tested conditions. For instance, wear rate of the FSPed sample subjected to 10 N load was found to be $5{:}99\times10^{-4}$ mm^3/Nm, which is less as compared to $7{:}82\times10^{-4}$ mm^3/Nm in the case of cast sample. The reduced wear behaviour shown by the cast sample may be attributed to coarse and brittle Mg_2Si features present in it whereas, for FSPed specimens, fine in-situ Mg_2Si precipitates was recognized for better wear resistance. With the increase in load from 10 N to 40 N, wear loss was found to be increased from 34.2 mg to 99.4 mg in the case of cast sample while 26.2 mg to 86.3 mg for FSPed specimen. Moreover, COF values decreased from 0.32 to 0.15 and 0.31 to 0.14 for the cast and FSPed samples, respectively. However, there was not much variation found in COF value for both conditions of AS21A alloy.

5. Mg_2Si precipitates acted as an active load bearing candidate, thus decreasing the COF fluctuations in FSPed samples. The mechanisms found accountable for the wear of samples were abrasion, adhesion, oxidation, delamination and plastic deformation. At a high load regime, dominant mechanisms observed in the base and processed samples were delamination and plastic deformation, respectively.

6. The excellent ductility obtained in cast AS21A alloy through FSP gave a novel idea to further explore the investigated alloy for bearing applications. For this, a comparison was made between the investigated material and the Babbitt alloy in respect of microstructure, microhardness and wear. It was observed that the FSPed AS21A alloy exhibits comparable characteristics with that of Babbitt alloy. Therefore, a sector shape pad was fabricated for thrust bearing application using FSPed AS21A material through a multi-pass FSP strategy.

5.2 Future Scope of the work

- The current thesis work presents the characteristics of Mg-Al-Si based AS21A alloy at room temperature conditions only. Since Mg-Al-Si alloys are heat-resistant, their behaviour could be assessed for elevated temperature applications also.

- The newly prepared sector shape pad could be evaluated for further analysis in respect of load-carrying capacity and wear characteristics under different ambient conditions.

REFERENCES

[1] "US Energy Information Administration Website: http://tonto.eia.doe.gov/dnav/pet/hist/wtotworldw.htm (last accessed on December 20, 2009.)."

[2] A. A. Nayeb-Hashemi and J. B. Clark, *Phase Diagrams of Binary Magnesium Alloys*. 1988.

[3] M. M. Avedesian and H. Baker, *ASM specialty handbook: magnesium and magnesium alloys*. 1999.

[4] K. U. Kainer, Ed., *Magnesium Alloys and their Applications*. Wiley, 2000.

[5] B. L. Mordike and T. Ebert, "Magnesium Properties - applications - potential," *Mater. Sci. Eng. A*, vol. 302, no. 1, pp. 37–45, 2001, doi: 10.1016/S0921-5093(00)01351-4.

[6] R. W. Cahn, P. Haasen, and E. J. Kramer, *Materials Science and Technology: A Comprehensive Treatment*. 2008.

[7] H. E. Friedrich and B. L. Mordike, *Magnesium technology: Metallurgy, design data, applications*. 2006.

[8] D. Eliezer, E. Aghion, and F. H. Froes, "Magnesium science, technology and applications," *Adv. Perform. Mater.*, vol. 5, no. 3, pp. 201–212, 1998, doi: 10.1023/A:1008682415141.

[9] C.S. Roberts, *Magnesium and its alloys*, vol. 270, no. 1. 1960.

[10] M. Gupta and N. M. L. Sharon, *Magnesium, Magnesium Alloys, and Magnesium Composites*. 2010.

[11] I. Polmear, D. St. John, J. F. Nie, and M. Qian, *Light Alloys: Metallurgy of the Light Metals: Fifth Ed.* 2017.

[12] *ASM Handbook Volume 15: Casting*. ASM International, 2008.

[13] M. Pekguleryuz, K. Kainer, and A. A. Kaya, *Fundamentals of magnesium alloy metallurgy*. 2013.

[14] K. U. Kainer, *Magnesium Alloys and Technologies*. 2006.

[15] S. N. Mathaudhu, A. A. Luo, N. R. Neelameggham, E. A. Nyberg, and W. H. Sillekens, Eds., *Essential Readings in Magnesium Technology*. Cham: Springer International Publishing, 2016.

[16] B. R. Powell, A. A. Luo, V. Rezhets, J. J. Bommarito, and B. L. Tiwari, "Development of creep-resistant magnesium alloys for powertrain applications: Part 1 of 2," *SAE Tech. Pap.*, 2001, doi: 10.4271/2001-01-0422.

[17] W. E. Mercer, "Magnesium die cast alloys for elevated temperature applications," *SAE Tech. Pap.*, 1990, doi: 10.4271/900788.

[18] A. A. Luo, "Recent magnesium alloy development for elevated temperature applications," *Int. Mater. Rev.*, vol. 49, no. 1, pp. 13–30, 2004, doi: 10.1179/095066004225010497.

[19] R. Ninomiya, T. Ojiro, and K. Kubota, "Improved heat resistance of Mg-Al alloys by the Ca addition," *Acta Metall. Mater.*, vol. 43, no. 2, pp. 669–674, 1995, doi: 10.1016/0956-7151(94)00269-N.

[20] G. B. B. E A Brandes, *Smithells Light Metals Handbook*. Elsevier, 1998.

[21] and E. S. S. Beer, G. Frommeyer, "Development of Mg-Mg2Si light weight alloys," in *Magnesium Alloys and Their Applications*, K. U. Kainer, Ed. Wiley, 1992.

[22] L. K. T.B. Massalski, H. Okamoto, P.R. Subramanian, Ed., *Binary Alloy Phase Diagrams*. 1986.

[23] M. Mabuchi, K. Kubota, and K. Higashi, "Elevated temperature mechanical properties of magnesium alloys containing Mg2Si," *Mater. Sci. Technol.*, vol. 12, no. 1, pp. 35–39, 1996, doi: 10.1179/mst.1996.12.1.35.

[24] S. Zhu *et al.*, “Evaluation of Magnesium Die-Casting Alloys for Elevated Temperature Applications: Microstructure, Tensile Properties, and Creep Resistance,” *Metall. Mater. Trans. A Phys. Metall. Mater. Sci.*, vol. 46, no. 8, pp. 3543–3554, 2015, doi: 10.1007/s11661-015-2946-9.
[25] A. Luo and M. O. Pekguleryuz, “Cast magnesium alloys for elevated temperature applications,” *J. Mater. Sci.*, vol. 29, no. 20, pp. 5259–5271, 1994, doi: 10.1007/BF01171534.
[26] M. Mabuchi, K. Kubota, and K. Higashi, “Tensile strength, ductility and fracture of magnesium-silicon alloys,” *J. Mater. Sci.*, vol. 31, no. 6, pp. 1529–1535, 1996, doi: 10.1007/BF00357861.
[27] A. A. Luo, “Applications: Aerospace, automotive and other structural applications of magnesium,” in *Fundamentals of Magnesium Alloy Metallurgy: A volume in Woodhead Publishing Series in Metals and Surface Engineering*, 2013, pp. 266–316.
[28] A. A. Luo, “Magnesium casting technology for structural applications,” *J. Magnes. Alloy.*, vol. 1, no. 1, pp. 2–22, 2013, doi: 10.1016/j.jma.2013.02.002.
[29] M. Badri, S. M. Miresmaeili, and B. Nami, “Microstructure and impression creep properties of Ca-containing AS31 magnesium alloy,” *Acta Metall. Sin. (English Lett.*, vol. 29, no. 12, pp. 1089–1097, 2016, doi: 10.1007/s40195-016-0491-1.
[30] B. Bronfin, M. Katsir, and E. Aghion, “Preparation and solidification features of AS21 magnesium alloy,” *Mater. Sci. Eng. A*, vol. 302, no. 1, pp. 46–50, 2001, doi: 10.1016/S0921-5093(00)01352-6.
[31] J. L. Hu, C. P. Tang, X. M. Zhang, and Y. L. Deng, “Modification of Mg2Si in Mg-Si alloys with neodymium,” *Trans. Nonferrous Met. Soc. China (English Ed.*, vol. 23, no. 11, pp. 3161–3166, 2013, doi: 10.1016/S1003-6326(13)62847-2.
[32] H. Dong, S. Xiang, J. Lv, Y. Wang, L. Li, and W. Yu, “Modification of Mg2Si Phase Morphology in Mg-4Si Alloy by Sb and Nd Additions,” *J. Mater. Eng. Perform.*, vol. 29, no. 6, pp. 3678–3687, 2020, doi: 10.1007/s11665-020-04812-y.
[33] S. D. Sheng, D. Chen, and Z. H. Chen, “Effects of Si addition on microstructure and mechanical properties of RS/PM (rapid solidification and powder metallurgy) AZ91 alloy,” *J. Alloys Compd.*, vol. 470, no. 1–2, 2009, doi: 10.1016/j.jallcom.2008.03.005.
[34] M. Mabuchi, K. Kubota, and K. Higashi, “Effect of hot extrusion on mechanical properties of a MgSiAl alloy,” *Mater. Lett.*, vol. 19, no. 5–6, pp. 247–250, 1994, doi: 10.1016/0167-577X(94)90165-1.
[35] L. J. Cao, G. R. Ma, and C. C. Tang, “Effects of isothermal process parameters on semisolid microstructure of Mg-8Al-1Si alloy,” *Trans. Nonferrous Met. Soc. China (English Ed.*, vol. 22, no. 10, pp. 2364–2369, 2012, doi: 10.1016/S1003-6326(11)61472-6.
[36] L. Lu, M. O. Lai, and M. L. Hoe, “Formation of nanocrystalline Mg2Si and Mg2Si dispersion strengthened Mg-Al alloy by mechanical alloying,” *Nanostructured Mater.*, vol. 10, no. 4, pp. 551–563, 1998, doi: 10.1016/S0965-9773(98)00102-0.
[37] Q. D. Wang, Y. J. Chen, L. J. Zhang, J. B. Lin, and C. Q. Zhai, “Microstructure and mechanical properties of AZ31-0.5%Si alloy processed by ECAP,” *Trans. Nonferrous Met. Soc. China (English Ed.*, vol. 16, no. SUPPL. 3, pp. 1660–1663, 2006.
[38] W. M. Gan, K. Wu, M. Y. Zheng, X. J. Wang, H. Chang, and H. G. Brokmeier, “Microstructure and mechanical property of the ECAPed Mg2Si/Mg composite,” *Mater. Sci. Eng. A*, vol. 516, no. 1–2, pp. 283–289, 2009, doi: 10.1016/j.msea.2009.03.034.
[39] P. Serre, R. B. Figueiredo, N. Gao, and T. G. Langdon, “Influence of strain rate on the characteristics of a magnesium alloy processed by high-pressure torsion,” *Mater. Sci. Eng. A*, vol. 528, no. 10–11, pp. 3601–3608, 2011, doi: 10.1016/j.msea.2011.01.066.

[40] Z. M. Zhang, C. J. Xu, X. F. Guo, and S. Z. Jia, “Reciprocating extrusion of in situ Mg2Si reinforced Mg-Al based composite,” *Acta Metall. Sin. (English Lett.*, vol. 21, no. 3, pp. 169–177, 2008, doi: 10.1016/S1006-7191(08)60035-6.

[41] W. Guo, Q. D. Wang, B. Ye, H. Zhou, and J. F. Liu, “Microstructure and mechanical properties of AZ31-Mg<inf>2</inf>Si in situ composite fabricated by repetitive upsetting,” *Trans. Nonferrous Met. Soc. China (English Ed.*, vol. 24, no. 12, pp. 3755–3761, 2014, doi: 10.1016/S1003-6326(14)63529-9.

[42] J. Metayer, B. Ye, W. Guo, Q. D. Wang, H. Zhou, and F. Mollet, “Microstructure and mechanical properties of Mg-Si alloys processed by cyclic closed-die forging,” *Trans. Nonferrous Met. Soc. China (English Ed.*, vol. 24, no. 1, pp. 66–75, 2014, doi: 10.1016/S1003-6326(14)63029-6.

[43] W. Guo, Q. Wang, B. Ye, and H. Zhou, “Enhanced microstructure homogeneity and mechanical properties of AZ31-Si composite by cyclic closed-die forging,” *J. Alloys Compd.*, vol. 552, pp. 409–417, 2013, doi: 10.1016/j.jallcom.2012.11.067.

[44] K. Mohan Agarwal, R. K. Tyagi, V. K. Chaubey, and A. Dixit, “Comparison of different methods of Severe Plastic Deformation for grain refinement,” *IOP Conf. Ser. Mater. Sci. Eng.*, vol. 691, no. 1, 2019, doi: 10.1088/1757-899X/691/1/012074.

[45] V. Segal, “Review: Modes and processes of severe plastic deformation (SPD),” *Materials (Basel).*, vol. 11, no. 7, 2018, doi: 10.3390/ma11071175.

[46] Z. Y. Ma, “Friction stir processing technology: A review,” *Metall. Mater. Trans. A Phys. Metall. Mater. Sci.*, vol. 39 A, no. 3, pp. 642–658, 2008, doi: 10.1007/s11661-007-9459-0.

[47] R. S. Mishra and Z. Y. Ma, “Friction stir welding and processing,” *Mater. Sci. Eng. R Reports*, vol. 50, no. 1–2, 2005, doi: 10.1016/j.mser.2005.07.001.

[48] T. R. McNelley, S. Swaminathan, and J. Q. Su, “Recrystallization mechanisms during friction stir welding/processing of aluminum alloys,” *Scr. Mater.*, vol. 58, no. 5, pp. 349–354, 2008, doi: 10.1016/j.scriptamat.2007.09.064.

[49] Z. Y. Ma, R. S. Mishra, and M. W. Mahoney, “Superplastic deformation behaviour of friction stir processed 7075 Al alloy,” *Acta Mater.*, vol. 50, no. 17, pp. 4419–4430, 2002, doi: 10.1016/S1359-6454(02)00278-1.

[50] R. S. Mishra, Z. Y. Ma, and I. Charit, “Friction stir processing: A novel technique for fabrication of surface composite,” *Mater. Sci. Eng. A*, vol. 341, no. 1–2, pp. 307–310, 2003, doi: 10.1016/S0921-5093(02)00199-5.

[51] M. K. B. Givi and P. Asadi, *Advances in Friction-Stir Welding and Processing*. 2014.

[52] R. Bauri and D. Yadav, “Introduction to Friction Stir Processing (FSP),” *Met. Matrix Compos. by Frict. Stir Process.*, pp. 17–29, 2018, doi: 10.1016/b978-0-12-813729-1.00002-4.

[53] M. Azizieh, A. H. Kokabi, and P. Abachi, “Effect of rotational speed and probe profile on microstructure and hardness of AZ31/Al2O3 nanocomposites fabricated by friction stir processing,” *Mater. Des.*, vol. 32, no. 4, pp. 2034–2041, 2011, doi: 10.1016/j.matdes.2010.11.055.

[54] H. Eftekharinia, A. A. Amadeh, A. Khodabandeh, and M. Paidar, “Microstructure and wear behavior of AA6061/SiC surface composite fabricated via friction stir processing with different pins and passes,” *Rare Met.*, vol. 39, no. 4, pp. 429–435, 2020, doi: 10.1007/s12598-016-0691-x.

[55] R. Hashemi and G. Hussain, “Wear performance of Al/TiN dispersion strengthened surface composite produced through friction stir process: A comparison of tool geometries and number of passes,” *Wear*, vol. 324–325, pp. 45–54, 2015, doi: 10.1016/j.wear.2014.11.024.

[56] G. Faraji and P. Asadi, “Characterization of AZ91/alumina nanocomposite produced

by FSP," *Mater. Sci. Eng. A*, vol. 528, no. 6, pp. 2431–2440, 2011, doi: 10.1016/j.msea.2010.11.065.

[57] E. R. I. Mahmoud, M. Takahashi, T. Shibayanagi, and K. Ikeuchi, "Effect of friction stir processing tool probe on fabrication of SiC particle reinforced composite on aluminium surface," *Sci. Technol. Weld. Join.*, vol. 14, no. 5, pp. 413–425, 2009, doi: 10.1179/136217109X406974.

[58] G. Faraji, O. Dastani, and S. A. A. A. Mousavi, "Effect of process parameters on microstructure and micro-hardness of AZ91/Al 2O 3 surface composite produced by FSP," *J. Mater. Eng. Perform.*, vol. 20, no. 9, pp. 1583–1590, 2011, doi: 10.1007/s11665-010-9812-0.

[59] R. Singha, S. A. Rizvi, and S. P. Tewari, "Effect of friction stir welding on the tensile properties of AA6063 under different conditions," *Int. J. Eng. Trans. A Basics*, vol. 30, no. 4, pp. 597–603, 2017, doi: 10.5829/idosi.ije.2017.30.04a.19.

[60] P. Asadi, M. K. Besharati Givi, and G. Faraji, "Producing ultrafine-grained AZ91 from as-cast AZ91 by FSP," *Mater. Manuf. Process.*, vol. 25, no. 11, pp. 1219–1226, 2010, doi: 10.1080/10426911003636936.

[61] D. Khayyamin, A. Mostafapour, and R. Keshmiri, "The effect of process parameters on microstructural characteristics of AZ91/SiO 2 composite fabricated by FSP," *Mater. Sci. Eng. A*, vol. 559, pp. 217–221, 2013, doi: 10.1016/j.msea.2012.08.084.

[62] P. Asadi, G. Faraji, and M. K. Besharati, "Producing of AZ91/SiC composite by friction stir processing (FSP)," *Int. J. Adv. Manuf. Technol.*, vol. 51, no. 1–4, pp. 247–260, 2010, doi: 10.1007/s00170-010-2600-z.

[63] A. Z. Naser and B. M. Darras, "Experimental investigation of Mg/SiC composite fabrication via friction stir processing," *Int. J. Adv. Manuf. Technol.*, vol. 91, no. 1–4, pp. 781–790, 2017, doi: 10.1007/s00170-016-9801-z.

[64] A. Devaraju, A. Kumar, A. Kumaraswamy, and B. Kotiveerachari, "Influence of reinforcements (SiC and Al2O3) and rotational speed on wear and mechanical properties of aluminum alloy 6061-T6 based surface hybrid composites produced via friction stir processing," *Mater. Des.*, vol. 51, pp. 331–341, 2013, doi: 10.1016/j.matdes.2013.04.029.

[65] Y. Morisada, H. Fujii, T. Nagaoka, and M. Fukusumi, "Effect of friction stir processing with SiC particles on microstructure and hardness of AZ31," *Mater. Sci. Eng. A*, vol. 433, no. 1–2, pp. 50–54, 2006, doi: 10.1016/j.msea.2006.06.089.

[66] C. J. Lee, J. C. Huang, and P. J. Hsieh, "Mg based nano-composites fabricated by friction stir processing," *Scr. Mater.*, vol. 54, no. 7, pp. 1415–1420, 2006, doi: 10.1016/j.scriptamat.2005.11.056.

[67] M. Dadashpour, A. Mostafapour, R. Yeşildal, and S. Rouhi, "Effect of process parameter on mechanical properties and fracture behavior of AZ91C/SiO2 composite fabricated by FSP," *Mater. Sci. Eng. A*, vol. 655, pp. 379–387, 2016, doi: 10.1016/j.msea.2015.12.103.

[68] M. Abbasi, B. Bagheri, M. Dadaei, H. R. Omidvar, and M. Rezaei, "The effect of FSP on mechanical, tribological, and corrosion behavior of composite layer developed on magnesium AZ91 alloy surface," *Int. J. Adv. Manuf. Technol.*, vol. 77, no. 9–12, pp. 2051–2058, 2015, doi: 10.1007/s00170-014-6577-x.

[69] A. Alavi Nia and S. H. Nourbakhsh, "Microstructure and Mechanical Properties of AZ31/SiC and AZ31/CNT Composites Produced by Friction Stir Processing," *Trans. Indian Inst. Met.*, vol. 69, no. 7, pp. 1435–1442, 2016, doi: 10.1007/s12666-015-0702-x.

[70] K. A. J. Langari, F. Kolahan, "Effect of Tool Speed on Axial Force, Mechanical Properties and Weld Morphology of Friction Stir Welded Joints of A7075-T651," *Int.*

J. Eng. C Asp., vol. 29, no. 3, pp. 403–410, 2016, doi: 10.5829/idosi.ije.2016.29.03c.15.
[71] Y. Jiang, X. Yang, H. Miura, and T. Sakai, "Nano-SiO2 particles reinforced magnesium alloy produced by friction stir processing," *Rev. Adv. Mater. Sci.*, vol. 33, no. 1, pp. 29–32, 2013.
[72] D. Lu, Y. Jiang, and R. Zhou, "Wear performance of nano-Al2O3 particles and CNTs reinforced magnesium matrix composites by friction stir processing," *Wear*, vol. 305, no. 1–2, pp. 286–290, 2013, doi: 10.1016/j.wear.2012.11.079.
[73] M. Navazani and K. Dehghani, "Investigation of Microstructure and Hardness of Mg/TiC Surface Composite Fabricated by Friction Stir Processing (FSP)," *Procedia Mater. Sci.*, vol. 11, pp. 509–514, 2015, doi: 10.1016/j.mspro.2015.11.082.
[74] K. K. Ajith Kumar, U. T. S. Pillai, B. C. Pai, and M. Chakraborty, "Dry sliding wear behaviour of Mg-Si alloys," *Wear*, vol. 303, no. 1–2, pp. 56–64, 2013, doi: 10.1016/j.wear.2013.02.020.
[75] Katsuyoshi Kondoh, Junko UMEDA, Kenshi KAWABATA, Yoshikazu SEKI, and Yoshihito KAWAMURA, "Wear Behavior of Sintered Magnesium Matrix Composites Reinforced with Mg2Si Particle under Wet Sliding Conditions," *Trans. JWRI*, vol. 37, no. 1, pp. 45–50, 2008, [Online]. Available: https://www.researchgate.net/publication/43169655_Wear_Behavior_of_Sintered_Magnesium_Matrix_Composites_Reinforced_with_Mg2Si_Particle_under_Wet_Sliding_Conditions.
[76] H. Pourfallah and M. Shahmiri, "Effect of SIMA Process on Microstructure and Wear Behavior of Al-Mg 2 Si-3% Ni Composite," *Metallogr. Microstruct. Anal.*, vol. 8, no. 1, pp. 109–117, 2019, doi: 10.1007/s13632-018-0500-z.
[77] N. Soltani, H. R. Jafari Nodooshan, A. Bahrami, M. I. Pech-Canul, W. Liu, and G. Wu, "Effect of hot extrusion on wear properties of Al-15wt.% Mg2Si in situ metal matrix composites," *Mater. Des.*, vol. 53, pp. 774–781, 2014, doi: 10.1016/j.matdes.2013.07.084.
[78] X. F. Wu, G. G. Zhang, and F. F. Wu, "Microstructure and dry sliding wear behavior of cast Al-Mg2Si in-situ metal matrix composite modified by Nd," *Rare Met.*, vol. 32, no. 3, pp. 284–289, 2013, doi: 10.1007/s12598-013-0030-4.
[79] B. Akyüz, "Comparison of the machinability and wear properties of magnesium alloys," *Int. J. Adv. Manuf. Technol.*, vol. 75, no. 9–12, pp. 1735–1742, 2014, doi: 10.1007/s00170-014-6256-y.
[80] S. Q. Tang, J. X. Zhou, C. W. Tian, and Y. S. Yang, "Morphology modification of Mg2Si by Sr addition in Mg-4Si alloy," *Trans. Nonferrous Met. Soc. China (English Ed.*, vol. 21, no. 9, pp. 1932–1936, 2011, doi: 10.1016/S1003-6326(11)60952-7.
[81] W. Wang, K. Wang, Q. Guo, and N. Wu, "Effect of friction stir processing on microstructure and mechanical properties of cast AZ31 magnesium alloy," *Xiyou Jinshu Cailiao Yu Gongcheng/Rare Met. Mater. Eng.*, vol. 41, no. 9, pp. 1522–1526, 2012, doi: 10.1016/s1875-5372(13)60004-1.
[82] A. H. Feng and Z. Y. Ma, "Enhanced mechanical properties of Mg-Al-Zn cast alloy via friction stir processing," *Scr. Mater.*, vol. 56, no. 5, pp. 397–400, 2007, doi: 10.1016/j.scriptamat.2006.10.035.
[83] F. Y. Zheng, Y. J. Wu, L. M. Peng, X. W. Li, P. H. Fu, and W. J. Ding, "Microstructures and mechanical properties of friction stir processed Mg-2.0Nd-0.3Zn-1.0Zr magnesium alloy," *J. Magnes. Alloy.*, vol. 1, no. 2, pp. 122–127, 2013, doi: 10.1016/j.jma.2013.06.001.
[84] Z. Y. Ma, A. L. Pilchak, M. C. Juhas, and J. C. Williams, "Microstructural refinement and property enhancement of cast light alloys via friction stir processing," *Scr. Mater.*,

vol. 58, no. 5, pp. 361–366, 2008, doi: 10.1016/j.scriptamat.2007.09.062.

[85] D. Zhang, M. Suzuki, and K. Maruyama, "Microstructural evolution of a heat-resistant magnesium alloy due to friction stir welding," *Scr. Mater.*, vol. 52, no. 9, pp. 899–903, 2005, doi: 10.1016/j.scriptamat.2005.01.003.

[86] H. S. Arora, H. Singh, and B. K. Dhindaw, "Some observations on microstructural changes in a Mg-based AE42 alloy subjected to friction stir processing," *Metall. Mater. Trans. B Process Metall. Mater. Process. Sci.*, vol. 43, no. 1, pp. 92–108, 2012, doi: 10.1007/s11663-011-9573-7.

[87] T. S. Mahmoud and S. S. Mohamed, "Improvement of microstructural, mechanical and tribological characteristics of A413 cast Al alloys using friction stir processing," *Mater. Sci. Eng. A*, vol. 558, pp. 502–509, 2012, doi: 10.1016/j.msea.2012.08.036.

[88] B. Zahmatkesh, M. H. Enayati, and F. Karimzadeh, "Tribological and microstructural evaluation of friction stir processed Al2024 alloy," *Mater. Des.*, vol. 31, no. 10, pp. 4891–4896, 2010, doi: 10.1016/j.matdes.2010.04.054.

[89] R. Abdi behnagh, M. K. Besharati Givi, and M. Akbari, "Mechanical properties, corrosion resistance, and microstructural changes during friction stir processing of 5083 aluminum rolled plates," *Mater. Manuf. Process.*, vol. 27, no. 6, pp. 636–640, 2012, doi: 10.1080/10426914.2011.593243.

[90] G. M. Reddy and K. S. Rao, "Enhancement of wear and corrosion resistance of cast A356 aluminium alloy using friction stir processing," *Trans. Indian Inst. Met.*, vol. 63, no. 5, pp. 793–798, 2010, doi: 10.1007/s12666-010-0121-y.

[91] S. A. Alidokht, A. Abdollah-Zadeh, S. Soleymani, T. Saeid, and H. Assadi, "Evaluation of microstructure and wear behavior of friction stir processed cast aluminum alloy," *Mater. Charact.*, vol. 63, pp. 90–97, 2012, doi: 10.1016/j.matchar.2011.11.007.

[92] H. S. Arora, H. Singh, and B. K. Dhindaw, "Wear behaviour of a Mg alloy subjected to friction stir processing," *Wear*, vol. 303, no. 1–2, pp. 65–77, 2013, doi: 10.1016/j.wear.2013.02.023.

[93] X. hao DU and B. lin WU, "Using friction stir processing to produce ultrafine-grained microstructure in AZ61 magnesium alloy," *Trans. Nonferrous Met. Soc. China (English Ed.*, vol. 18, no. 3, pp. 562–565, 2008, doi: 10.1016/S1003-6326(08)60098-9.

[94] K. N. Ramesh, S. Pradeep, and V. Pancholi, "Multipass friction-stir processing and its effect on mechanical properties of aluminum alloy 5086," *Metall. Mater. Trans. A Phys. Metall. Mater. Sci.*, vol. 43, no. 11, pp. 4311–4319, 2012, doi: 10.1007/s11661-012-1232-3.

[95] Y. J. Kwon, I. Shigematsu, and N. Saito, "Mechanical properties of fine-grained aluminum alloy produced by friction stir process," *Scr. Mater.*, vol. 49, no. 8, pp. 785–789, 2003, doi: 10.1016/S1359-6462(03)00407-X.

[96] E. A. El-Danaf and M. M. El-Rayes, "Microstructure and mechanical properties of friction stir welded 6082 AA in as welded and post weld heat treated conditions," *Mater. Des.*, vol. 46, pp. 561–572, 2013, doi: 10.1016/j.matdes.2012.10.047.

[97] M. Vignesh Kumar, G. Padmanaban, and V. Balasubramanian, "Sliding Wear Characteristics of Friction Stir Processed CAST ZK60 Magnesium Alloy Under Different Applied Loads," *Trans. Indian Inst. Met.*, vol. 71, no. 5, pp. 1223–1230, 2018, doi: 10.1007/s12666-017-1257-9.

[98] G. Cao, D. Zhang, W. Zhang, and C. Qiu, "Microstructure evolution and mechanical properties of Mg-Nd-Y alloy in different friction stir processing conditions," *J. Alloys Compd.*, vol. 636, pp. 12–19, 2015, doi: 10.1016/j.jallcom.2015.02.081.

[99] P. Cavaliere and P. P. De Marco, "Effect of friction stir processing on mechanical and microstructural properties of AM60B Magnesium alloy," *J. Mater. Sci.*, vol. 41, no.

11, pp. 3459–3464, 2006, doi: 10.1007/s10853-005-5601-9.
[100] Y. Wang, Y. Huang, X. Meng, L. Wan, and J. Feng, “Microstructural evolution and mechanical properties of Mg[sbnd]Zn[sbnd]Y[sbnd]Zr alloy during friction stir processing,” *J. Alloys Compd.*, vol. 696, pp. 875–883, 2017, doi: 10.1016/j.jallcom.2016.12.068.
[101] J. Li, D.-T. Zhang, F. Chai, and W. Zhang, “Microstructures and mechanical properties of WE43 magnesium alloy prepared by friction stir processing,” *Rare Met.*, vol. 39, no. 11, pp. 1267–1272, 2020, doi: 10.1007/s12598-014-0306-3.
[102] B. L. Xiao, Q. Yang, J. Yang, W. G. Wang, G. M. Xie, and Z. Y. Ma, “Enhanced mechanical properties of Mg-Gd-Y-Zr casting via friction stir processing,” *J. Alloys Compd.*, vol. 509, no. 6, pp. 2879–2884, 2011, doi: 10.1016/j.jallcom.2010.11.147.
[103] L. Tonelli *et al.*, “Effect of FSP parameters and tool geometry on microstructure, hardness, and wear properties of AA7075 with and without reinforcing B4C ceramic particles,” *Int. J. Adv. Manuf. Technol.*, vol. 102, no. 9–12, pp. 3945–3961, 2019, doi: 10.1007/s00170-019-03442-6.
[104] S. K. Patel, V. P. Singh, and B. Kuriachen, “Microstructural, Tribological and Mechanical Properties Evolution of ZrSiO4/A4047 Surface Composite Fabricated through Friction Stir Processing,” *Trans. Indian Inst. Met.*, vol. 72, no. 7, pp. 1765–1774, 2019, doi: 10.1007/s12666-019-01647-7.
[105] D. Ahmadkhaniha, M. Heydarzadeh Sohi, A. Salehi, and R. Tahavvori, “Formations of AZ91/Al2O3 nano-composite layer by friction stir processing,” *J. Magnes. Alloy.*, vol. 4, no. 4, pp. 314–318, 2016, doi: 10.1016/j.jma.2016.11.002.
[106] I. Dinaharan, S. C. Vettivel, M. Balakrishnan, and E. T. Akinlabi, “Influence of processing route on microstructure and wear resistance of fly ash reinforced AZ31 magnesium matrix composites,” *J. Magnes. Alloy.*, vol. 7, no. 1, pp. 155–165, 2019, doi: 10.1016/j.jma.2019.01.003.
[107] I. Dinaharan, S. Saravanakumar, K. Kalaiselvan, and S. Gopalakrishnan, “Microstructure and sliding wear characterization of Cu/TiB 2 copper matrix composites fabricated via friction stir processing,” *J. Asian Ceram. Soc.*, vol. 5, no. 3, pp. 295–303, 2017, doi: 10.1016/j.jascer.2017.06.002.
[108] M. Balakrishnan, I. Dinaharan, R. Palanivel, and R. Sivaprakasam, “Synthesize of AZ31/TiC magnesium matrix composites using friction stir processing,” *J. Magnes. Alloy.*, vol. 3, no. 1, pp. 76–78, 2015, doi: 10.1016/j.jma.2014.12.007.
[109] Y. Morisada, H. Fujii, T. Nagaoka, and M. Fukusumi, “MWCNTs/AZ31 surface composites fabricated by friction stir processing,” *Mater. Sci. Eng. A*, vol. 419, no. 1–2, pp. 344–348, 2006, doi: 10.1016/j.msea.2006.01.016.
[110] M. Navazani and K. Dehghani, “Fabrication of Mg-ZrO2 surface layer composites by friction stir processing,” *J. Mater. Process. Technol.*, vol. 229, pp. 439–449, 2016, doi: 10.1016/j.jmatprotec.2015.09.047.
[111] K. Sun, Q. Y. Shi, Y. J. Sun, and G. Q. Chen, “Microstructure and mechanical property of nano-SiCp reinforced high strength Mg bulk composites produced by friction stir processing,” *Mater. Sci. Eng. A*, vol. 547, pp. 32–37, 2012, doi: 10.1016/j.msea.2012.03.071.
[112] G. Madhusudhan Reddy, A. Sambasiva Rao, and K. Srinivasa Rao, “Friction stir processing for enhancement of wear resistance of ZM21 magnesium alloy,” *Trans. Indian Inst. Met.*, vol. 66, no. 1, pp. 13–24, 2013, doi: 10.1007/s12666-012-0163-4.
[113] ahmad haghani, S. H. Nourbakhsh, and M. Jahangiri, “Investigation of Mechanical Property and Microstructure of Nanocomposite AZ31/SiC Fabricated by Friction Stir Process,” *ADMT J.*, vol. 9, no. 2, pp. 27–34, 2016.
[114] M. Sharifitabar, M. Kashefi, and S. Khorshahian, “Effect of friction stir processing

pass sequence on properties of Mg-ZrSiO4-Al2O3 surface hybrid micro/nano-composites," *Mater. Des.*, vol. 108, pp. 1–7, 2016, doi: 10.1016/j.matdes.2016.06.087.

[115] T. Thankachan and K. S. Prakash, "Microstructural, mechanical and tribological behavior of aluminum nitride reinforced copper surface composites fabricated through friction stir processing route," *Mater. Sci. Eng. A*, vol. 688, no. February, pp. 301–308, 2017, doi: 10.1016/j.msea.2017.02.010.

[116] S. A. Alidokht, A. Abdollah-zadeh, S. Soleymani, and H. Assadi, "Microstructure and tribological performance of an aluminium alloy based hybrid composite produced by friction stir processing," *Mater. Des.*, vol. 32, no. 5, pp. 2727–2733, 2011, doi: 10.1016/j.matdes.2011.01.021.

[117] M. Narimani, B. Lotfi, and Z. Sadeghian, "Evaluation of the microstructure and wear behaviour of AA6063-B4C/TiB2 mono and hybrid composite layers produced by friction stir processing," *Surf. Coatings Technol.*, vol. 285, pp. 1–10, 2016, doi: 10.1016/j.surfcoat.2015.11.015.

[118] C. N. Shyam Kumar, R. Bauri, and D. Yadav, "Wear properties of 5083 Al-W surface composite fabricated by friction stir processing," *Tribol. Int.*, vol. 101, pp. 284–290, 2016, doi: 10.1016/j.triboint.2016.04.033.

[119] A. Devaraju, A. Kumar, and B. Kotiveerachari, "Influence of addition of Grp/Al2O3p with SiCp on wear properties of aluminum alloy 6061-T6 hybrid composites via friction stir processing," *Trans. Nonferrous Met. Soc. China (English Ed.*, vol. 23, no. 5, pp. 1275–1280, 2013, doi: 10.1016/S1003-6326(13)62593-5.

[120] I. Dinaharan, K. Kalaiselvan, E. T. Akinlabi, and J. P. Davim, "Microstructure and wear characterization of rice husk ash reinforced copper matrix composites prepared using friction stir processing," *J. Alloys Compd.*, vol. 718, pp. 150–160, 2017, doi: 10.1016/j.jallcom.2017.05.117.

[121] R. Palanivel, I. Dinaharan, R. F. Laubscher, and J. P. Davim, "Influence of boron nitride nanoparticles on microstructure and wear behavior of AA6082/TiB2 hybrid aluminum composites synthesized by friction stir processing," *Mater. Des.*, vol. 106, pp. 195–204, 2016, doi: 10.1016/j.matdes.2016.05.127.

[122] S. Saravanakumar, S. Gopalakrishnan, I. Dinaharan, and K. Kalaiselvan, "Assessment of microstructure and wear behavior of aluminum nitrate reinforced surface composite layers synthesized using friction stir processing on copper substrate," *Surf. Coatings Technol.*, vol. 322, pp. 51–58, 2017, doi: 10.1016/j.surfcoat.2017.05.029.

[123] S. Selvakumar, I. Dinaharan, R. Palanivel, and B. Ganesh Babu, "Characterization of molybdenum particles reinforced Al6082 aluminum matrix composites with improved ductility produced using friction stir processing," *Mater. Charact.*, vol. 125, pp. 13–22, 2017, doi: 10.1016/j.matchar.2017.01.016.

[124] H. Chen and A. T. Alpas, "Sliding wear map for the magnesium alloy Mg-9Al-0.9 Zn (AZ91)," *Wear*, vol. 246, no. 1–2, pp. 106–116, 2000, doi: 10.1016/S0043-1648(00)00495-6.

[125] S. Anbu selvan and S. Ramanathan, "Dry sliding wear behavior of as-cast ZE41A magnesium alloy," *Mater. Des.*, vol. 31, no. 4, pp. 1930–1936, 2010, doi: 10.1016/j.matdes.2009.10.054.

[126] A. J. López, P. Rodrigo, B. Torres, and J. Rams, "Dry sliding wear behaviour of ZE41A magnesium alloy," *Wear*, vol. 271, no. 11–12, pp. 2836–2844, 2011, doi: 10.1016/j.wear.2011.05.043.

[127] J. An *et al.*, "Dry sliding wear behavior of magnesium alloys," *Wear*, vol. 265, no. 1–2, pp. 97–104, 2008, doi: 10.1016/j.wear.2007.08.021.

[128] C. Taltavull, P. Rodrigo, B. Torres, A. J. López, and J. Rams, "Dry sliding wear behavior of AM50B magnesium alloy," *Mater. Des.*, vol. 56, pp. 549–556, 2014, doi:

10.1016/j.matdes.2013.12.015.
[129] M. L. Hu, Q. D. Wang, Z. S. Ji, H. Y. Xu, M. De Xin, and G. R. Ma, "Wear behavior of Mg-10Y-4Gd-1.5Zn-0.4Zr alloy," *Trans. Nonferrous Met. Soc. China (English Ed.*, vol. 26, no. 2, pp. 406–413, 2016, doi: 10.1016/S1003-6326(16)64092-X.
[130] K. Meshinchi Asl, A. Masoudi, and F. Khomamizadeh, "The effect of different rare earth elements content on microstructure, mechanical and wear behavior of Mg-Al-Zn alloy," *Mater. Sci. Eng. A*, vol. 527, no. 7–8, pp. 2027–2035, 2010, doi: 10.1016/j.msea.2009.11.061.
[131] K. Elangovan and V. Balasubramanian, "Influences of tool pin profile and tool shoulder diameter on the formation of friction stir processing zone in AA6061 aluminium alloy," *Mater. Des.*, vol. 29, no. 2, pp. 362–373, 2008, doi: 10.1016/j.matdes.2007.01.030.
[132] W. C. Parr and G. Taguchi, *Introduction to Quality Engineering: Designing Quality into Products and Processes*, vol. 31, no. 2. 1989.
[133] J. R. Simpson, "Taguchi Techniques for Quality Engineering," *J. Qual. Technol.*, vol. 28, no. 4, pp. 487–489, 1996, doi: 10.1080/00224065.1996.11979713.
[134] D. Ahmadkhaniha, M. Heydarzadeh Sohi, A. Zarei-Hanzaki, S. M. Bayazid, and M. Saba, "Taguchi optimization of process parameters in friction stir processing of pure Mg," *J. Magnes. Alloy.*, vol. 3, no. 2, pp. 168–172, 2015, doi: 10.1016/j.jma.2015.04.002.
[135] M. Salehi, M. Saadatmand, and J. Aghazadeh Mohandesi, "Optimization of process parameters for producing AA6061/SiC nanocomposites by friction stir processing," *Trans. Nonferrous Met. Soc. China (English Ed.*, vol. 22, no. 5, pp. 1055–1063, 2012, doi: 10.1016/S1003-6326(11)61283-1.
[136] D. Julong, "Introduction to grey system," *J. Grey Syst.*, vol. 1, no. 1, pp. 1–24, 1989.
[137] Ş. Kasman, "Multi-response optimization using the Taguchi-based grey relational analysis: A case study for dissimilar friction stir butt welding of AA6082-T6/AA5754-H111," *Int. J. Adv. Manuf. Technol.*, vol. 68, no. 1–4, pp. 795–804, 2013, doi: 10.1007/s00170-012-4720-0.
[138] S. Vijayan, R. Raju, and S. R. K. Rao, "Multiobjective optimization of friction stir welding process parameters on aluminum alloy AA 5083 using taguchi-based grey relation analysis," *Mater. Manuf. Process.*, vol. 25, no. 11, pp. 1206–1212, 2010, doi: 10.1080/10426910903536782.
[139] N. D. Ghetiya, K. M. Patel, and A. J. Kavar, "Multi-objective Optimization of FSW Process Parameters of Aluminium Alloy Using Taguchi-Based Grey Relational Analysis," *Trans. Indian Inst. Met.*, vol. 69, no. 4, pp. 917–923, 2016, doi: 10.1007/s12666-015-0581-1.
[140] H. S. Lu, C. K. Chang, N. C. Hwang, and C. T. Chung, "Grey relational analysis coupled with principal component analysis for optimization design of the cutting parameters in high-speed end milling," *J. Mater. Process. Technol.*, vol. 209, no. 8, pp. 3808–3817, 2009, doi: 10.1016/j.jmatprotec.2008.08.030.
[141] P. K. Sahu and S. Pal, "Multi-response optimization of process parameters in friction stir welded AM20 magnesium alloy by Taguchi grey relational analysis," *J. Magnes. Alloy.*, vol. 3, no. 1, pp. 36–46, 2015, doi: 10.1016/j.jma.2014.12.002.
[142] C. P. Fung and P. C. Kang, "Multi-response optimization in friction properties of PBT composites using Taguchi method and principle component analysis," *J. Mater. Process. Technol.*, vol. 170, no. 3, pp. 602–610, 2005, doi: 10.1016/j.jmatprotec.2005.06.040.
[143] P. Zhang, "Creep behavior of the die-cast Mg-Al alloy AS21," *Scr. Mater.*, vol. 52, no. 4, pp. 277–282, 2005, doi: 10.1016/j.scriptamat.2004.10.017.

[144] G. Li, H. S. Gill, and R. A. Varin, “Magnesium silicide intermetallic alloys,” *Metall. Trans. A*, vol. 24, no. 11, pp. 2383–2391, 1993, doi: 10.1007/BF02646518.

[145] E. Evangelista, E. Gariboldi, O. Lohne, and S. Spigarelli, “High-temperature behaviour of as die-cast and heat treated Mg-Al-Si AS21X magnesium alloy,” *Mater. Sci. Eng. A*, vol. 387–389, no. 1-2 SPEC. ISS., pp. 41–45, 2004, doi: 10.1016/j.msea.2004.02.077.

[146] M. S. Dargusch, A. L. Bowles, K. Pettersen, P. Bakke, and G. L. Dunlop, “The effect of silicon content on the microstruture and creep behavior in die-cast magnesium AS alloys,” *Metall. Mater. Trans. A Phys. Metall. Mater. Sci.*, vol. 35 A, no. 6, pp. 1905–1909, 2004, doi: 10.1007/s11661-004-0099-3.

[147] M. L. Santella, T. Engstrom, D. Storjohann, and T. Y. Pan, “Effects of friction stir processing on mechanical properties of the cast aluminum alloys A319 and A356,” *Scr. Mater.*, vol. 53, no. 2, pp. 201–206, 2005, doi: 10.1016/j.scriptamat.2005.03.040.

[148] Z. Y. Ma, S. R. Sharma, and R. S. Mishra, “Microstructural modification of As-cast Al-Si-Mg alloy by friction stir processing,” *Metall. Mater. Trans. A Phys. Metall. Mater. Sci.*, vol. 37, no. 11, pp. 3323–3336, 2006, doi: 10.1007/BF02586167.

[149] J. F. Archard, “Contact and rubbing of flat surfaces,” *J. Appl. Phys.*, vol. 24, no. 8, pp. 981–988, 1953, doi: 10.1063/1.1721448.

[150] J. F. Archard and P. R. S. L. A, “Elastic deformation and the laws of friction,” *Proc. R. Soc. London. Ser. A. Math. Phys. Sci.*, vol. 243, no. 1233, pp. 190–205, 1957, doi: 10.1098/rspa.1957.0214.

[151] D. Liu, M. Shen, Y. Tang, Y. Hu, and L. Zhao, “Effect of Multipass Friction Stir Processing on Surface Corrosion Resistance and Wear Resistance of ZK60 Alloy,” *Met. Mater. Int.*, vol. 25, no. 5, pp. 1182–1190, 2019, doi: 10.1007/s12540-019-00268-5.

[152] P. Asadi, G. Faraji, A. Masoumi, and M. K. B. Givi, “Experimental investigation of magnesium-base nanocomposite produced by friction stir processing: Effects of particle types and number of friction stir processing passes,” *Metall. Mater. Trans. A Phys. Metall. Mater. Sci.*, vol. 42, no. 9, pp. 2820–2832, 2011, doi: 10.1007/s11661-011-0698-8.

[153] H. Zengin, Y. Turen, and L. Elen, “A Comparative Study on Microstructure, Mechanical and Tribological Properties of A4, AE41, AS41 and AJ41 Magnesium Alloys,” *J. Mater. Eng. Perform.*, vol. 28, no. 8, pp. 4647–4657, 2019, doi: 10.1007/s11665-019-04223-8.

[154] P. R. C. Alcover Junior and A. G. M. Pukasiewicz, “Evaluation of microstructure, mechanical and tribological properties of a Babbitt alloy deposited by arc and flame spray processes,” *Tribol. Int.*, vol. 131, pp. 148–157, 2019, doi: 10.1016/j.triboint.2018.10.027.

PUBLICATIONS

International Journals/Proceedings

1. Sumit Joshi, Ramesh Chandra Singh. Singh, Rajiv Chaudhary, *Effect of rotational speed in friction stir processing on the microstructural and mechanical characteristics of cast AS21A magnesium alloy***,** Materials Research Express 6 (2019) 056554 **(SCIE),** IOP Publishing.

2. Sumit Joshi, Ramesh Chandra Singh. Singh, Rajiv Chaudhary**,** *Effect of Friction Stir Processing (FSP) on the wear behavior of cast AS21A magnesium alloy*, Surface Review And Letters, Vol. 28, No. 01, 2050037 (2021) (**SCI, SCIE**) World Scientific Publishing Company

3. Rajiv Chaudhary**, Sumit Joshi,** Ramesh Chandra Singh, *Mechanical and wear performance of surface composite fabricated by solid-state technique-a review*, Materials Today: Proceedings 5 (2018) 28033-28042 **(Scopus)** Elsevier Publication.

4. Sumit Joshi, Ramesh Chandra Singh, Rajiv Chaudhary, *Microstructural and wear characterisation of as-cast AS21A magnesium alloy*, Journal of Physics: Conference Series 1240 (2019) 012127 **(Scopus)** IOP Publishing.

International/National Conferences

1. **Sumit Joshi,** Rajiv Chaudhary, R.C. Singh**,** *A survey on tribological performance of light-weight alloys subjected to Friction Stir Processing***,** Proceedings of 1st International Conference on New Frontiers in Engineering Science & Technology (NFEST-2018), DTU, New Delhi, Excellent Publishing House (ISBN: 978-93-86238-41-2).

2. **Sumit Joshi,** Rajiv Chaudhary, R.C. Singh**,** *Surface modification of cast magnesium alloy through friction stir processing*, Proceedings of International Conference on Advanced Production and Industrial Engineering (ICAPIE-2017), DTU, New Delhi, I.K. International Publishing House Pvt. Ltd (ISBN: 9789384588076).

3. **Sumit Joshi,** Rajiv Chaudhary, R.C. Singh**,** *A Review – Mechanical/Tribological behavior of FSPed Aluminum alloys/Surface Composites***,** National Conference on Recent Trends in Engineering, Science and Management (NCRTESM-2017), SRCEM, Palwal, Paper No. 170.

4. **Sumit Joshi,** Rajiv Chaudhary, R.C. Singh**,** *Fabrication of Mg alloy/B_4C surface composite by Friction Stir processing***,** Proceedings of International Conference on Advanced Production and Industrial Engineering (ICAPIE-2016), DTU, New Delhi, I.K. International Publishing House Pvt. Ltd (ISBN: 978-9-38-590951-1).

BIOGRAPHICAL SKETCH

SUMIT JOSHI

Mr. Sumit Joshi is a research scholar in the Department of Mechanical Engineering, Delhi Technological University, New Delhi. He holds a Master's degree from Delhi Technological University, New Delhi. As recognition of his academic achievements, he has received a Research Excellence award from DTU for his research activities. He is presently working as an Assistant Professor in the Department of Mechanical and Automation Engineering at Maharaja Agrasen Institute of Technology, Delhi. Mr. Sumit has been involved in research on the materials characterization, surface engineering and tribology of Machine Elements. He has authored many research papers in International Journals and Conferences of repute.